UiO : Department of Geosciences
University of Oslo

Floods during the last millennium - analysis of trends and the uniqueness of Storofsen in 1789

A case study for two snowmelt dominated catchments in south-eastern Norway

Jørgen Håvardslien

Master's Thesis, Spring 2023

Floods during the last millennium - analysis of trends and the uniqueness of Storofsen in 1789: A case study for two snowmelt dominated catchments in south-eastern Norway

This Master's Thesis is published electronically in DUO - Digitale Utgivelser ved UiO: http://www.duo.uio.no/

Printed: Reprosentralen, Universitetet i Oslo

Abstract

Floods are natural disasters that destroy infrastructure and sometimes claim human lives. Future flood events are predicted to become larger and more frequent. To plan for the future, it is valuable to have knowledge about the past. The largest known flood occurring in Norway during historical time is the infamous Storofsen in late July, 1789. In this study, I investigated the hydrometeorological conditions causing Storofsen and placed this extraordinary event into the context where the evolution of floods during three historical time periods: Medieval Warm Period (MWP), Little Ice Age (LIA) and Industrial Time (IT) was analysed. This study focuses on two catchments in south-eastern Norway (Lalm and Elverum) where the 1789-flood caused large impacts and the actual flood levels are known. The hydrological modelling framework Shyft was used to simulate discharge and key water balance components. Paleo climate output from the Norwegian Earth System Model (NorESM1-F) for the three periods MWP, LIA and IT was used as model forcings to establish a dataset of simulated floods from the past millennium. The same model was used to establish precipitation events capable of reproducing Storofsen. The results show that (i) there are slightly higher and more frequent floods during the LIA as compared to MWP and IT (ii) the flood seasonality is consistent for all three periods, where the annual maximum floods occur in May/June at Lalm and May at Elverum. Furthermore, none of the simulated floods occurred in late July, confirming that the Storofsen flood was exceptional. Several of the simulated floods exceeded the Storofsen flood with up to 100% within each of the periods, however, these simulated peaks are deemed to be unrealistic. Peak mean precipitation required to cause a simulated flood with the magnitude of Storofsen was found to be 612.4 and 93.7 mm/day for Lalm and Elverum, respectively.

Acknowledgements

First of all, I would like to thank my supervisor Kolbjørn Engeland for valuable guidance throughout the Master Thesis project. Many thanks to Olga Silantyeva for helping me setting up and running the hydrological model using the Shyft modelling framework, and for helpful feedback. Thanks to Lu Li for preparing the paleo climate data of NorESM1-F for the study and providing feedback throughout the research. Also, thanks to Chuncheng Guo and Zhongshi Zhang for their work of NorESM1-F modelling, which is supported by the Bjerknes Centre for Climate Research strategic project PARCIM (Proxy Assimilation for Reconstructing Climate and Improving Model). I acknowledge the UNINETT Sigma2 for computing and storage resources (nn9039k, ns9039k and ns9001k). Many thanks to Lena Tallaksen for valuable comments and tips for the writing of the thesis and feedback on the obtained results. I also want to thank Hans Peter Verne and Luc Girod from the IT-department for resolving the technical computer and server issues that I encountered.

Contents

List of Figures

List of Tables

CHAPTER 1

Introduction

1.1 Motivation

Globally, floods are the most common type of natural disaster (Alderman et al., 2012). During the 1990s, around 100,000 people were killed by floods and more than 1.4 billion people were affected by floods (Jonkman, 2005). Between 2000 and 2010, floods were the cause of almost 53,000 deaths (Alderman et al., 2012). Additionally, more than 220,000 people died due to floods between 1980 and 2013 (Winsemius et al., 2016). Floods are also a major cause of economic damages worldwide, and they resulted in losses of more than 1 trillion dollars in the period 1980-2013, globally (Dottori et al., 2016). Moreover, floods account for at least one third of all losses caused by natural disasters (Loster, 1999). In recent decades, over 7000 natural disasters occurred, out of which about three-quarters were related to water, and among those, floods accounted for approximately one third (Douben, 2006).

Although, human lives are rarely lost due to floods in Norway, floods do still have major consequences. Floods cause huge damages and large economic losses in Norway every year (Roald, 2013). In Norway, floods cause an average annual loss of around 200 million Norwegian kroner (NOK) (Nadim et al., 2008). Insurance companies have covered losses of 2.939 billion NOK due to floods during the last 10 years, distributed on 18,627 insurance cases (Finans Norge, 2023). Even though deaths caused by floods in recent years are rare, there are evidence about catastrophic flood events in the past.

One of the oldest documented large floods occurred in the year 1342 or 1348 (Roald, 2013). This flood is named *Digerofsen*, where *diger* means *large/big* and *ofse* means *vehemence* or *fierceness* (Mardal, 2018). In the year 1345, there was a large landslide in Gaula that temporally dammed the river. When the barrier eventually broke it lead to a catastrophic flood, which buried multiple churches and farms, as well as killing approximately 250 people (Roald, 2013; Thorsnæs, 2021). It is clear that floods had the ability to cause devastating damages to communities more than 600 years ago, which were much smaller than the ones that exist today. One can only imagine what consequences these immense floods could cause today with all the modern infrastructure, such as roads, railroads, hospitals, telecommunication and electric power lines.

Consequences of larger and more frequent floods might already be noticeable. Yearly flood damage for the last seven years has more than tripled compared to

the period 1980-2010 (Glover et al., 2018). The number of flood damages has increased by 150% during the period 2010-2019, compared to the mean of the last two previous ten year periods (Larsen-Vonstett, 2020). Additionally, the cost of damages caused by floods have increased by 176% in the last 10 years. It is also estimated that future rain floods will be more frequent and of a larger magnitude than compared to today (Alnes et al., 2018). If the meteorological conditions are changing, is it possible that another flood disaster similar to Storofsen could strike in the near future?

It has often been said that understanding the past is the key to understand the future. This statement also holds true for floods. If one acquires knowledge about past flooding events, it is easier to create solutions for problems related to floods in the future. Floods are closely related to climate and weather conditions, such as temperature and precipitation. Past climate variability can indicate what the future climate conditions will look like.

1.2 Theory

1.2.1 The hydrological cycle

The core principle in hydrology is the hydrological cycle. This cycle describes how a (random) water parcel is transported through the Earth's system. 97% of all the water on Earth is stored in the oceans (Chahine, 1992). From the oceans, water will evaporate into the atmosphere as vapor, which is only holding 0.001% of the Earth's water. Water vapor is released from the atmosphere as precipitation, either in form of rain, snow, sleet or hail, and ends up on the land surface, glaciers, in snow packs, in underground storage or lakes. Some water will also be transported from the land surface and into the air through evapotranspiration. Eventually, the water will, either as surface flow or ground water flow, find its way back into the oceans, and the cycle is complete. Obviously, this is only a highly simplified version, as the hydrological cycle is a vastly complex system. The scientific field of hydrology focuses on the water, that has been deposited as precipitation, and is transported downstream to the oceans. This will be water flow in streams, channels, rivers, underground soils and as melted water from snow packs and glaciers.

1.2.2 Floods

A definition of the word flood is expressed in Roald (2013), where he defines floods as when the water stage is so high that rivers and waters go over their widths and cause damage. There are mainly two dominating factors that contribute to the generation of floods, namely precipitation in the form of rainfall and melting water from snow packs and glaciers. Floods can be classified in different types based on the processes that produce them. These flood types are: (1) Long-rain floods, (2) Short-rain floods, (3) Flash floods, (4) Rain-on-snow floods and (5) Snow melt floods (Merz and Blöschl, 2003). Flood magnitude can be characterised by the return period, which is the time span in which a certain water discharge will be exceeded on average (Salas and Obeysekera, 2014). The inverse of the return period is the probability that a certain discharge is exceeded in one year.

Along the western coast of Norway, floods are mostly a result of precipitation, caused by atmospheric rivers that are orographically enhanced by the mountainous regions, combined with snow melt (Hegdahl et al., 2020). In the inland eastern part of the country, floods are mostly driven by snow melt, often combined with rain (see Section 1.2.3 for more details about runoff regimes in Norway). Snow melt floods can also lead to an ice jam flood. During such a flood, floating river ice can begin to accumulate due to the river topography or an obstruction, e.g. a bridge. The ice dam will prevent water from flowing downstream, causing an upstream flooding as the water is flowing over the river banks, or a sudden outburst flood if the ice dam collapses. Increasing flood frequency in southern and western Norway is primarily caused by increasing trends in the frequency of rainfall dominated events, whereas, decreasing flood frequency in northern Norway are mostly caused by decreasing trends in the frequency of snow melt dominated floods (Vormoor et al., 2016). Most of the catchments in Norway will experience an increase in flood frequency in the future (Huo et al., 2022). There will be increased autumn/winter floods and decreased spring/summer floods. In Western Norway, floods will increase in the future, as a result of increased precipitation, and there will be a shift leading to more rain-induced floods during autumn and winter (Sorteberg et al., 2018; Hanssen-Bauer et al., 2017; Lawrence and Hisdal, 2011).

Multiple studies have shown that extreme flooding events display some form of non-stationary (Olsen et al., 1999; Lins and Slack, 1999; Engeland et al., 2020). Based on paleo data, Engeland et al. (2020) found that flood frequency is non-stationary across time scales. In design flood estimates, it is possible to utilise paleo data in order to explore non-stationarity. Additionally, there are significant trends in annual maximum discharge during the 20th century in the United States (Lins and Slack, 1999). Similarly, statistically significant increasing trends in annual floods were found along the Upper Mississippi and Missouri Rivers (Olsen et al., 1999). These findings suggested that flood risk varies in time, which challenged the conventional assumption that time series of floods were independent random variables.

1.2.3 Runoff regimes in Norway

The runoff regimes in Norway has been separated into five categories (Gottschalk et al., 1979), which are seen in Figure 1.1. Gottschalk et al. (1979) describes the five regimes in Norway as the following:

- H_1L_1: Inner and northeast parts of Norway (mountain regime).
- H_2L_1: Fjord area along Norway's western coast, forest and coastal area to the west of the Gulf of Bothnia (inland regime).
- H_2L_2: Inlands in Østlandet (transition regime).
- H_2L_3: Parts of Møre-Trønderlag (Baltic regime).
- H_3L_3: Frontier coastal regions of Norway (Atlantic regime).

At the west coast of Norway there is a swift, but gradual regime change when moving inland (towards the east) (Gottschalk et al., 1979). The H_3L_3 regime is found at the very coast, while there is a transition zone of H_2L_3, H_2L_2 and H_2L_1 further inland. Although, the transition zone is so narrow that it is not feasible to differentiate all the types of regimes based on available observation stations. Figure 1.1 only show the regimes that have been verified. Furthermore, the mountainous regions consists of the regime type H_1L_1. Glaciated areas are not marked specifically in Figure 1.1, but they are all located within the H_1L_1 regime. These areas with glacial influence, could have maximum runoff late in the season, e.g. July/August.

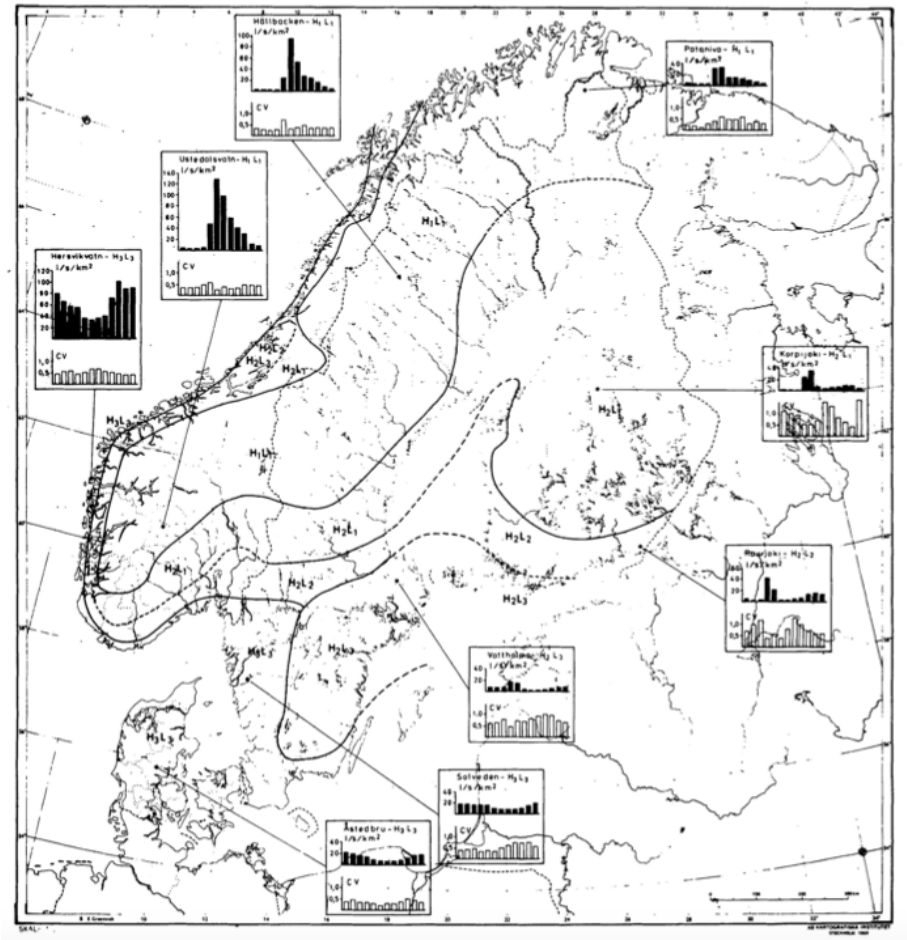

Figure 1.1: Map showing runoff regimes in the Nordic countries. Taken from Gottschalk et al. (1979).

1.2.4 Future floods

It is expected that a future climate would be warmer and have more intense precipitation than the climate that we experience today (Benestad, 2013). Such a climate scenario would increase the flood intensity (frequency and magnitude) in the areas where the floods are driven by precipitation. In contrast, areas that are prone to snow and glacier melt driven floods will most likely experience less intense flooding, due to smaller amounts of snow available for melting. Flood magnitudes are expected to increase in catchments that are rainfall-driven, while the magnitudes are expected to decrease in areas that are driven by snow melt (Lawrence, 2020). There are also expected to be changes in runoff regimes (Huo et al., 2022). In areas that are seasonally covered by snow, these changes can lead to a shift in flood generating processes. This means that floods mostly driven by snow melt previously, could become mostly driven by rainfall.

1.2.5 Flood prevention

There are many different mitigation measures for preventing and reducing damage caused by floods. Flood mitigation measures can be split into two categories: physical measures and informative measures. Physical measures revolves around creating physical obstructions against the floods, altering river channels or building dams. These include floodwalls/seawalls, floodgates, levees, dikes, channels and flood storage reservoirs. Reservoirs has the same effect on floods as lakes. When flood waves pass a lake or reservoir they become delayed and reduced (Roald, 2013). Dikes are famously used in the Netherlands, to prevent the low-laying land from being flooded by the ocean. Informative measures consists of acquiring knowledge about floods and how to respond to them. Examples of these measures are: discharge measurements, flood simulation, flood forecasting, flood hazard/risk maps, urban planning and evacuation. By obtaining knowledge about floods, it is easier to avoid building important infrastructure in places that are susceptible to flooding. Flood forecasting makes it possible to issue warnings to the public if there is a possibility of a large flood in the near future.

1.2.6 Climate in Norway during the last millennium

During the last millennium there has been identified two periods with a clear difference in climate (Huo et al., 2022). The first was a warming period from 950 to 1250, which is referred to as the Medieval Climate Anomaly (MCA) or the Medieval Warm Period (MWP), and the second was a cold period from 1500 to 1800, which is called the Little Ice Age (LIA). However, the timing of LIA varies between different sources (Hanssen-Bauer et al., 2009). Glaciers in Norway reached their maximum extent since the last ice age during LIA. In fact, many glaciers advanced over agricultural land and crops. This period was characterised by a lot of precipitation and strict winters, along with low temperatures during spring and autumn. The 1740s are deemed to be the worst decade, with famine due to crop failure. Reconstructions of precipitation show that periods with high winter precipitation occurred around 1710 and 1860, and periods with low winter precipitation happened around 1410 (Hanssen-Bauer et al., 2009).

1.3 Background

1.3.1 Past floods

A comprehensive collection of the largest floods in Norway during the last 660 years is included in Roald (2013). The earliest written records about floods in Norway date back to the year 1342/1348 (Digerofsen) and 1345 (Kvasshyllanraset), as previously mentioned. However, as a result of the lack of people to write down events that unfolded, due to the Black Death that hit Norway in 1348, there are no written records regarding floods during the 15th and 16th century. In 1653, there was a large rain flood in Numedalslågen after many days with heavy rain from late August to the first days of September. All the timber booms (used for timber floating) in Hjellevannet were destroyed by the flood. There was another rain flood in Driva river in late July of 1698, which damaged adjacent farms and fields. During 26-27th of August 1763, a thunderstorm and heavy rain showers hit Røldal, causing Røldalsvatnet to flood fields that were located close to the lake. While people were fleeing up to higher grounds, they witnessed their cabins floating down Storelva river. In late July 1789, Storofsen hit south-eastern Norway, which became the most catastrophic flood event in Norway in historical time (see Section 1.3.2). The large flood event in the spring of 1860, was a snow melt-driven flood. In the beginning of June 1995, there was another huge flood in south-eastern Norway, albeit not as huge as Storofsen. This 1995 flood has been named "Velseofsen", and is viewed as the "little brother" of Storofsen.

There are various different ways of collecting information about past floods. Hydrologists have performed discharge measurements for centuries, and historical flood records can date back more than a hundred years. For some extreme flooding events, monuments are made in order to preserve information about the peak water stage for future generations. These monuments are often called *flood rocks* or *flood stones*. Information about past extreme floods can also be found in church books. It is also possible to determine the size of past floods based on sediment cores. Paleo climate models can also be used to gain information about past floods, although this approach is only simulation and it does not necessarily match what actually happened.

1.3.2 Storofsen

Storofsen is the largest flood that has occurred in Norway in historical time. The flood event lasted from the 21st to the 23rd of July 1789 (Sommerfeldt, 1972; Otnes, 1982). It was mainly a rain flood, reinforced by large amounts of snow in the mountains and high temperatures (Roald, 2013). A more detailed description of the weather situation leading up to Storofsen is found in Section 1.3.3. The flood affected nearly the entirety of south-eastern Norway, and it also extended into Sweden by the eastern border. Storofsen left entire farms in ruins and many people lost their livelihoods for several years. As a results, tax reductions were given to farmers who had lost animals, field crops or buildings (Sommerfeldt, 1972). 72 people lost their lives due to the flood (Roald, 2013).

1.3.3 Weather situation in July 1789

The winter of 1788-89 began as cold and snow limited, however, plenty of snow started to fall over Østlandet later in the season (Roald, 2013). This particular winter was the hardest in a long time, not just in Norway, but in the rest of Europe, as well (Sommerfeldt, 1972). It rained extensively during the preceding autumn, although it snowed sparsely after the temperatures went below 0°C. The notably cold temperatures lasted from before Christmas and into April. Additionally, the ground was frozen much deeper than 1 meter some places. As a result, the ground needed a long time in order to thaw. The thawing resulted in a particularly wet soil, that remained so well into the summer.

On the 9th of March, there was an ice drift flood, which destroyed a bridge in Gausdal (Roald, 2013). Many landslides also occurred there. During early May, the temperature started to rise and a damaging flood arose in Romerike and Solør/Odal. Easterly winds and heavy rainfall began on the 18th and 19th of May. The weather was warm and wet during spring and summer. In the mountains, the snow melted and the upper part of the soil, above the previous winter's frost, became saturated. The weather was a huge contrast to previous years, and 1789 looked like it was going to be a great year for agriculture. However, during the course of July, the weather became even warmer and heavy thunderstorms lit up the sky. Apparently, it became hard to work outside due to the heat.

During the evening of the 20th of July, it started to rain over Østlandet (Østmoe, 1985). The rain intensified and the following day was turned black as night by heavy cloudbursts and thunderstorms. The cause of this extreme precipitation was a specific weather type, called *Vb track*. This Vb track (read: "five b") is a cyclone track type described by Wilhelm Jakob van Bebber in 1891 (Bebber, 1891; Hofstätter et al., 2016). The Vb track, transported warm and humid air northwards from the Mediterranean Sea, over Poland before it reached Østlandet from the south-east (Roald, 2013). Simultaneously, there was cold air coming from the west due to a low-pressure area in the ocean west of Trøndelag. As a result, a stationary front was formed over Østlandet, which produced massive amounts of precipitation over the course of three days. The rain intensified even more, and reached its peak on the 22nd of July (Østmoe, 1985). South-eastern Norway might not have received this amount of precipitation in a day, as on the 22nd of July 1789, for many centuries. Finally, on the 23rd of July, it rained significantly less and on the following day the weather was warm and the skies were clear again. The weather situation starting from the 11th of July to the 23rd of July is described in detail in Østmoe (1985).

1.3.4 Flood stones

On multiple places in Norway flood stones have been risen in order to show how high the water stage was during the most extreme flood events. A map of these flood stones in Østlandet can be found in Roald (2013). The flood stones at Fetsund, Fåvang and Lalm are shown in Figure 1.2. Figure 1.2d shows that the water level was 7.59 meters above the ground surface at Fetsund during the Storofsen flood in 1789. There was also a huge flooding in 1860. It is not hard to imagine how destructive and devastating these floods were, considering how

high the water stage was. In fact, it is almost completely unthinkable that the water could have reached such heights.

(a) Fåvang.

(b) Lalm.

(c) Fetsund.

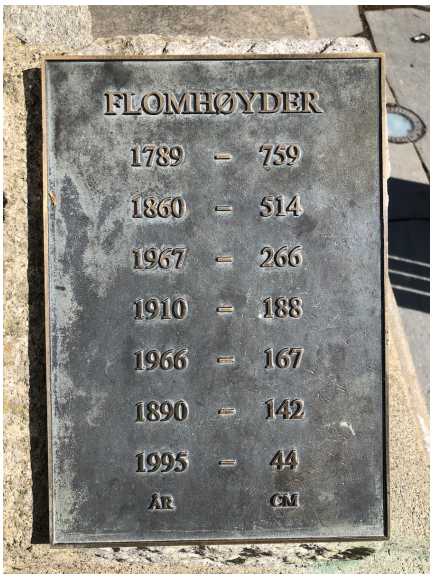

(d) Water level stages at Fetsund.

Figure 1.2: Flood stones at (a) Fåvang, (b) Lalm and (c) Fetsund, showing the water stage during the largest recorded floods in eastern Norway. The water level stages at Fetsund are shown in (d).

1.4 Aims of the study

The main aim of this study is to investigate the seasonality and magnitude of floods within the three historical periods: MWP, LIA and Industrial Time (IT), and comparing the results to the Storofsen flood. I also aim to identify the hydrometeorological conditions capable of causing Storofsen. Based on these aims, the following research questions are stated:

i) **Did flood seasonality and magnitude differ between MWP, LIA and IT?**

ii) **Did a flood occur at the same time of the season (late July) as Storofsen during the three periods MWP, LIA and IT?**

iii) **Did a flood of a comparable magnitude to Storofsen happen within the three periods MWP, LIA and IT?**

iv) **What were the hydrometeorological conditions that caused Storofsen in late July 1789?**

In order to answer the research questions, I will use meteorological forcing data, combined with observed discharge, in order to configure and calibrate a hydrological model using the *Shyft* modelling framework (Burkhart et al., 2021). The study area of the thesis will be the two catchments, Lalm and Elverum, since the flood levels of Storofsen are known for these catchments (Engeland et al., 2018; Engeland et al., 2020). Climate model data, covering the last 1200 years, will be bias corrected and used as model forcings for the hydrological model. This climate model data consists of two different versions, with high solar variability and low solar variability. The hydrological model will be used to simulated discharge within three historical periods, MWP, LIA and IT, where each simulation period would last 150 years. Furthermore, the simulated discharge will be analysed and compared to the Storofsen flooding of July 1789. The properties to be analysed are flood seasonality, magnitude and frequency. Lastly, a precipitation analysis of Storofsen will be performed.

CHAPTER 2

Study area

2.1 Catchments

The study area are the two catchments, Lalm and Elverum, which are both located in eastern Norway. Both catchments consist of large land form variations. As seen in Figure 2.1, Lalm catchment encloses mountains higher than 2000 Meters Above Sea Level (MASL), located in the eastern parts of Norway's highest mountain range, Jotunheimen. Elverum catchment mainly consists of areas with an elevation below 1000 MASL. The catchment area of Lalm and Elverum is 3978 and 15450 km^2, respectively (NVE, n.d.(a); NVE, n.d.(b)). Lalm and Elverum are both sub-catchments of Glomma catchment, with Lalm being the western branch and Elverum being the eastern branch.

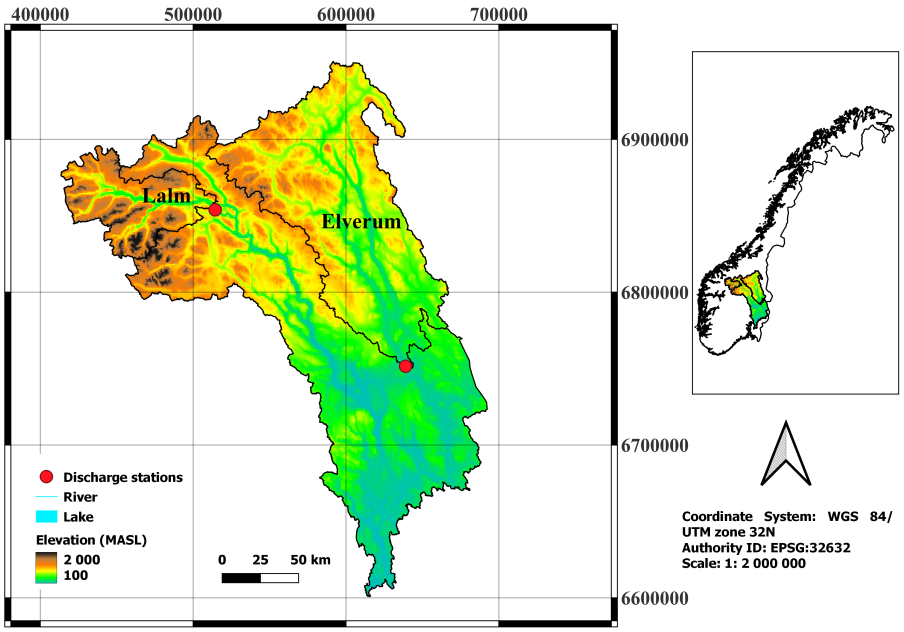

Figure 2.1: Topographic map of the catchments of Lalm and Elverum, which are sub-catchments of Glomma catchment.

Figure 2.2 shows the catchment area as a function of elevation for Lalm and Elverum catchment. 10% of Lalm catchment has an elevation less than 780 MASL, while 90% is lower than 1732 MASL. 50% of the catchment has an elevation of less than 1326 MASL. The elevation at Lalm is in the range of 355-2462 MASL. Elverum catchment is located further towards the east and therefore further away from mountain range of Jotunheimen. Consequently, Elverum is at a lower elevation than Lalm. The elevation range is 180-2170 MASL at Elverum. 10% of Elverum catchment is located below 466 MASL, while 90% is below 1155 MASL. 50% of the catchment has an altitude of less than 817 MASL.

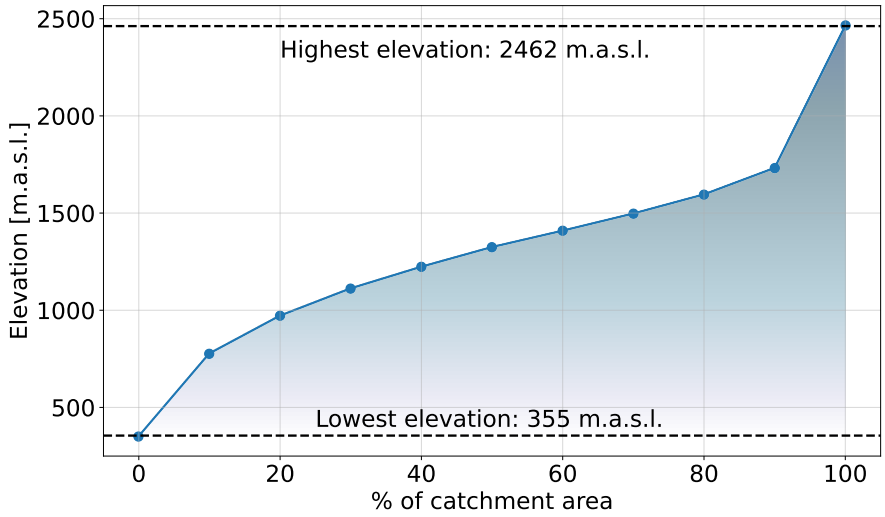

(a) Lalm.

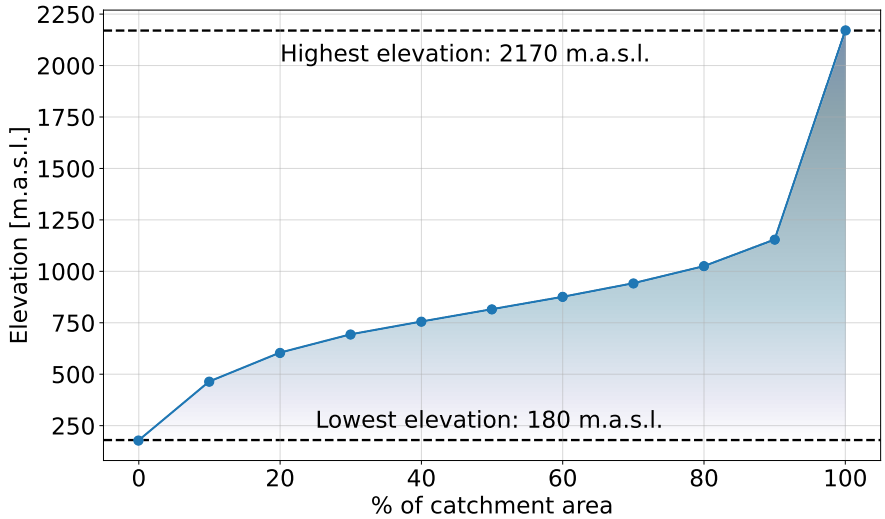

(b) Elverum.

Figure 2.2: Hypsographic curves for (a) Lalm and (b) Elverum. Data from NVE (n.d.[a]) and NVE (n.d.[b])).

2.2 Climate

The mean temperature and precipitation distribution based on the observed data (1957-2022 period) (The Norwegian Meteorological institute, MET Norway, 2022) is shown in Figure 2.3. Mean air temperature is lowest in the mountain regions. Accordingly, the mean temperature at Lalm is lower than at Elverum, since the former consists of more high altitude areas. The highest temperatures are found in the valleys. Elverum has quite evenly distributed precipitation, although with slightly more precipitation falling in the south compared to the north. In contrast, there is very high precipitation on the western border of Lalm catchment. At Lalm, the smallest amount of precipitation is located in the center of the catchment.

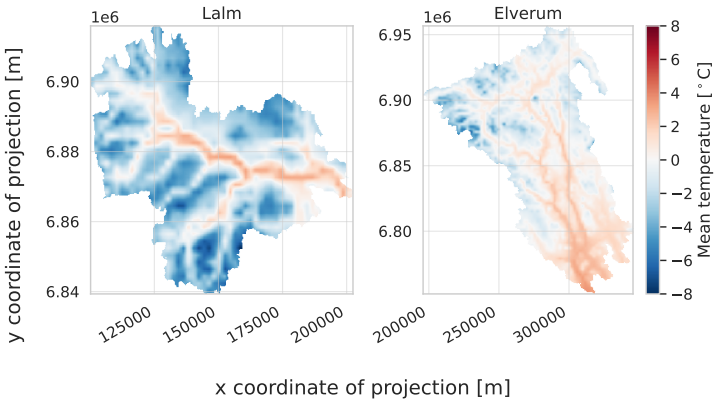

(a) Mean air temperature.

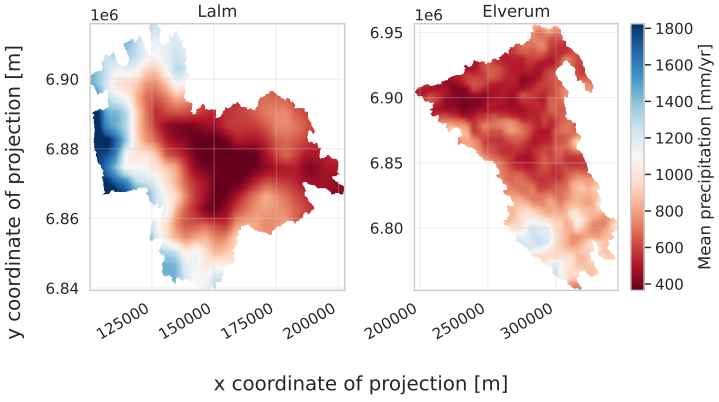

(b) Mean precipitation.

Figure 2.3: Mean (a) air temperature and (b) precipitation for Lalm and Elverum catchment in the period 1957 to 2022.

Figure 2.4 and Figure 2.5 show the seasonal temperature and precipitation means, respectively. Temperature is slightly higher during autumn than in spring. At Lalm, most precipitation falls in winter, while at Elverum most falls during summer. There is also quite high precipitation during autumn at the southern part of Elverum.

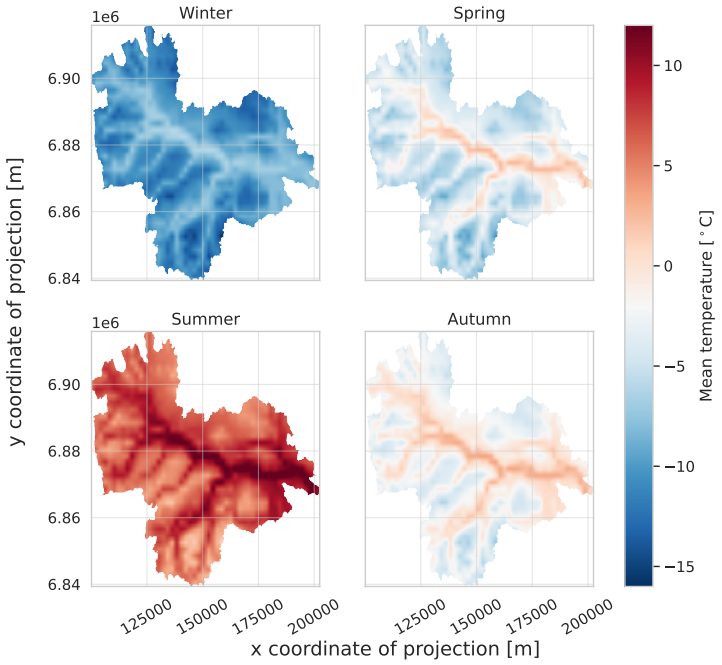

(a) Lalm.

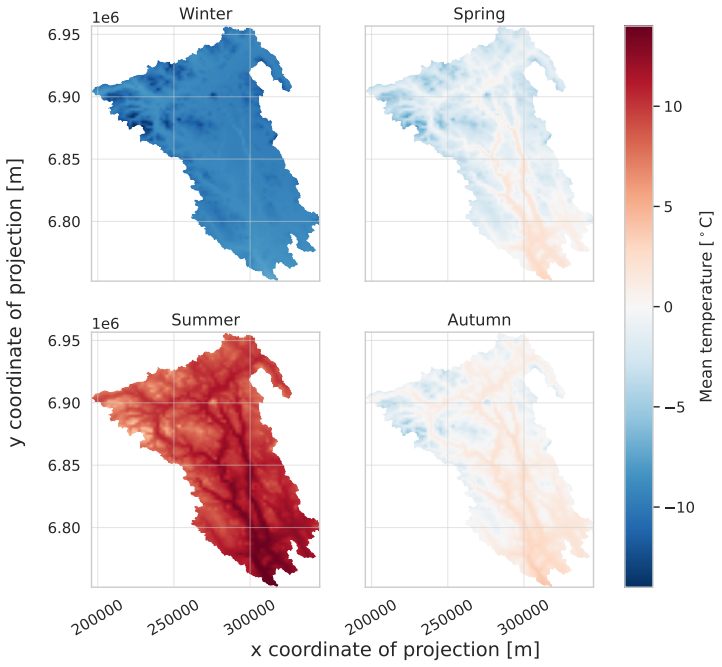

(b) Elverum.

Figure 2.4: Seasonal mean air temperature for (a) Lalm and (b) Elverum catchment in the period 1957 to 2022.

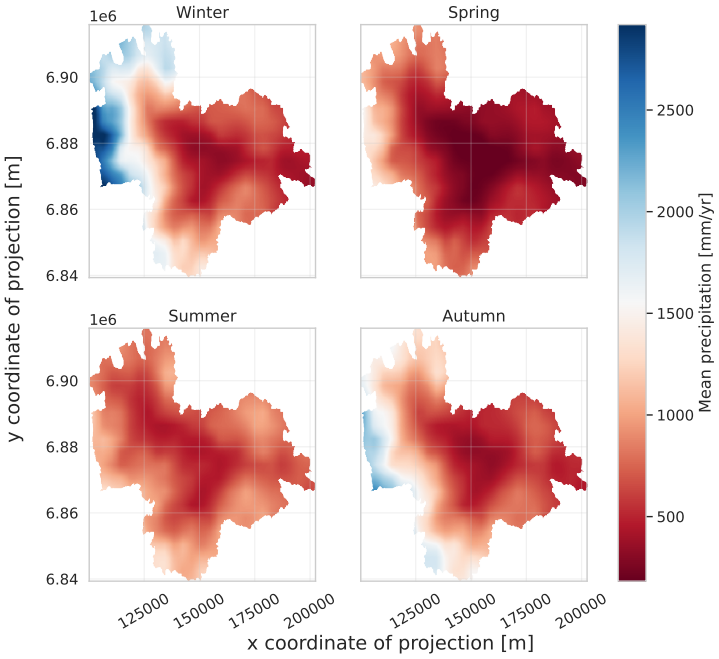

(a) Lalm.

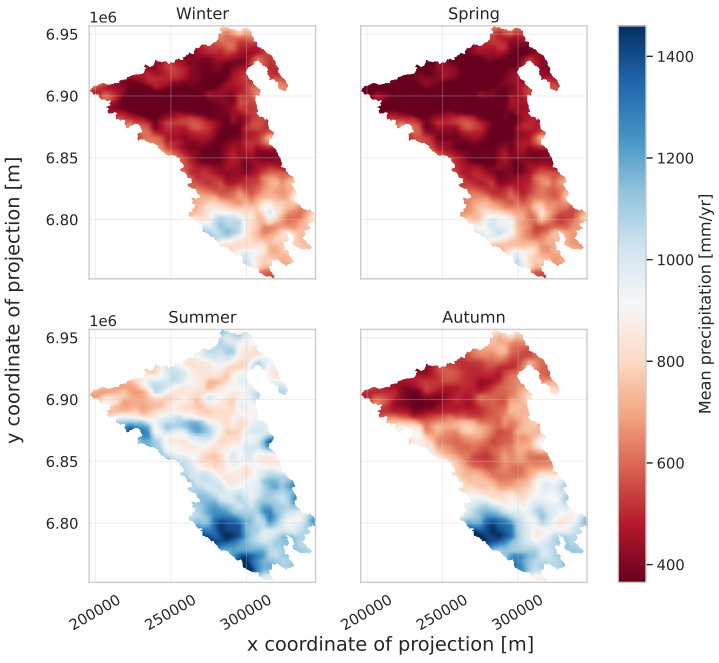

(b) Elverum.

Figure 2.5: Seasonal mean precipitation for (a) Lalm and (b) Elverum catchment in the period 1957 to 2022.

2.3 Discharge stations

There is one discharge measuring station at Lalm and one at Elverum. The discharge measurements from these stations are available through the database of the Norwegian Water Resources and Energy Directorate (NVE). Both stations are located in eastern Norway. Lalm station has been active since 1907 (Pettersson, 2014), and it has been regulated since 1956 (NVE, n.d.[b]). The percentage of regulation is 12.2% (Drageset, 2000). Lalm station is situated at 358 MASL. The geographical location of the station is at 61.817°N and 9.274°E. Elverum station has been operational since 1871, and was unregulated until 1917 (Pettersson, 2000). The percentage of regulation is 10% (Pettersson, 2014). This discharge station is situated at an elevation of 182 MASL. The station is geographically located at 60.874°N and 11.561°E. Lalm measuring station is situated in the river Otta, which is a tributary of the river Vorma-Lågen which again is a tributary of Glommavassdraget (NVE, n.d.[b]). Elverum measuring station is located in Glomma river, which is the longest river in Norway. Glomma river is part of Glommavassdraget.

2.4 Catchment hydrology

Flood characteristics (e.g. flood quantiles and mean floods) can vary greatly between different catchments. Physiographic characteristics such as catchment area, land use, soil type and geology can affect discharge within a catchment (Pilgrim et al., 1982). In addition, an increasing slope has also been found to decrease the seasonal discharge coefficient, which represented the fraction of rainfall that was measured as discharge (Taye et al., 2013). Table 2.1 shows floods with different selected return periods along with the corresponding water stage and discharge measured at Lalm and Elverum station. The mean flood is the largest at Elverum station with a value of 1420 m^3/s. In contrast, the mean flood at Lalm station is only 667 m^3/s. During a 50-year flood, the discharge is more than twice as large at Elverum (2529 m^3/s) than compared to Lalm (1103 m^3/s). Table 2.2 shows some characteristics of the two catchments.

Table 2.1: Flood characteristics at Lalm and Elverum measuring stations. Table from NVE (n.d.[a]) and NVE (n.d.[b]).

Station	Type	Water stage [MASL]	Discharge [m^3/s]
Lalm	50-year flood	359.0	1103.0
	20-year flood	358.7	981.0
	10-year flood	358.3	886.0
	5-year flood	358.0	788.0
	Mean flood	357.5	667.0
Elverum	50-year flood	181.8	2529.0
	20-year flood	181.4	2204.0
	10-year flood	181.1	1960.0
	5-year flood	180.8	1744.0
	Mean flood	180.3	1420.0

Table 2.2: Characteristics of the two catchments Lalm and Elverum. Table from NVE (n.d.[a]) and NVE (n.d.[b])).

Properties	Lalm	Elverum
River	Otta	Glommavassdraget
Catchment area	3977.8 km^2	15449.9 km^2
Catchment slope	24.0	No data
River gradient	7.1	2.0
Catchment length	109.3 km	226.0 km
River length	130.8 km	334.2 km

2.5 Land cover

There is a noticeable difference in the land cover of the two catchments. The main part of Lalm catchment consists of bare rock (70.3%) as seen in Figure 2.6. Furthermore, 14.6% of the area is made up of forests. Glaciers, cropland, sea and other make up less than 25% of the total area. More than half of Elverum catchment consists of forests (51.6%). 26.9% of the area is made up of bare rock and as much as 10.1% consists of marches. The remaining area consists of sea, cropland, other and urban areas. For both Lalm and Elverum, urban areas only make up 0.1% of the catchment area.

Lalm and Elverum catchments have other differences than the elevation profile and area. The forest, lake and glacier spatial distributions are displayed in Figure 2.7. Most of Elverum is covered by forests. Mainly, Lalm consists of a more alpine landscape and the forested areas are more concentrated to the valleys. Only a small part of both catchments consist of lakes, 3.8% at Lalm and 2.8% at Elverum. Lalm does have some glaciers (5.4%), most of which are found along the western catchment border. There are no glaciers at Elverum, mostly due to the catchment's lower elevation.

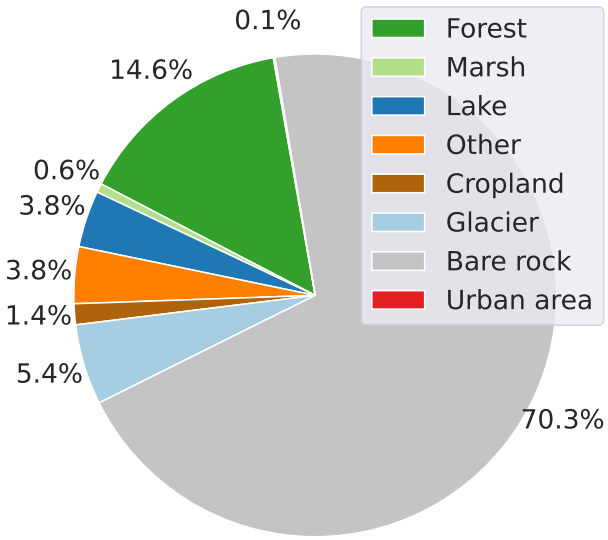

(a) Lalm.

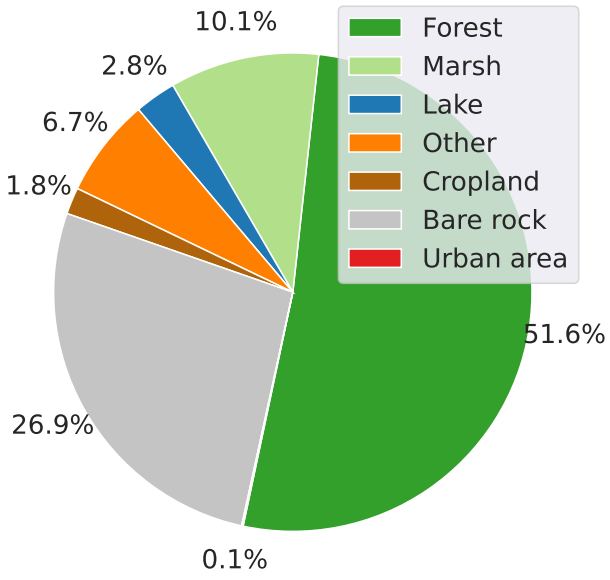

(b) Elverum.

Figure 2.6: Land cover of the two catchments (a) Lalm and (b) Elverum. Data from NVE (n.d.[a]) and NVE (n.d.[b])).

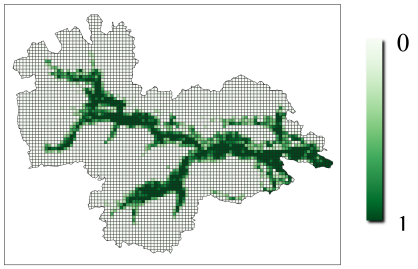

(a) Forest area at Lalm.

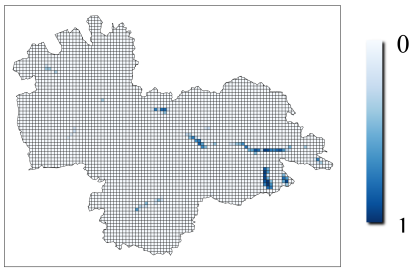

(b) Lake area at Lalm

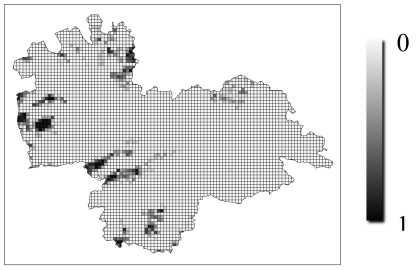

(c) Glacier area at Lalm.

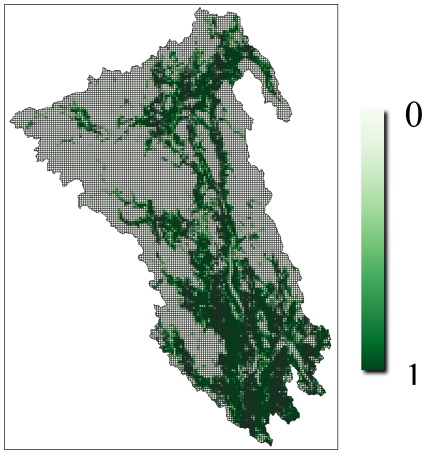

(d) Forest area at Elverum.

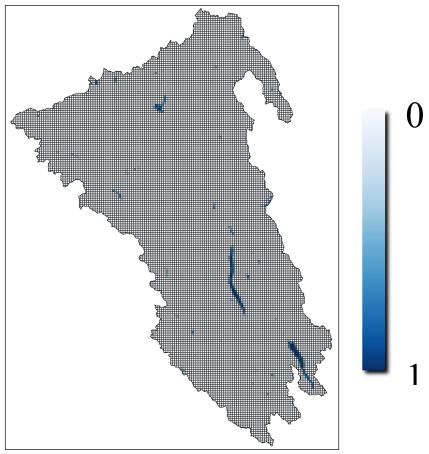

(e) Lake area at Elverum.

Figure 2.7: Area covered by forests, lakes and glaciers at catchments (a-c) Lalm and (d-e) Elverum. The grid has a 1 km x 1 km spatial resolution, and the colour bar represents the fraction of the three land use types forest, lake and glacier within each grid cell. Information about the land use covers were taken from GlobCover2009 (see Appendix A).

CHAPTER 3

Data

The data used for modelling can be separated into four categories: meteorological forcing data, observed discharge, climate model data and data for elevations and land cover. Furthermore, the meteorological forcing data include both gridded observational data and reanalysis data, which were used in combination with observed discharge, to calibrate the hydrological model (see Section 4.1). Data variables used consist of temperature, precipitation, wind speed, relative humidity and radiation. Climate model data was used as forcings for the hydrological model in order to simulate discharge for MWP, LIA and IT.

3.1 Meteorological forcing data

Shyft requires temperature, precipitation, wind speed, relative humidity and radiation. These data were found in three different datasets. Temperature and precipitation were taken from the seNorge_2018 dataset (The Norwegian Meteorological institute, MET Norway, 2022). seNorge is a collection of gridded datasets of daily aggregated two-meter air temperature and total precipitation observations made by the Norwegian Meteorological Institute (MET Norway). The datasets cover the Norwegian mainland and is made for application in climatological and hydrological research. Three datasets make up seNorge: seNorge version 1, seNorge version 2 and seNorge_2018, where seNorge_2018 is the newest, most up-to-date, dataset. The data are available from 1957 to 2022.

Wind speed was obtained from ERA_5-Land (Muñoz Sabater, 2019; Muñoz Sabater, 2021). Unlike seNorge_2018, ERA5-Land is a reanalysis dataset. Reanalysis datasets combine data from models with observations, in order to produce a dataset that is globally complete and consistent. ERA5-Land is a gridded dataset with a regular latitude-longitude grid. The dataset has a horizontal resolution of 0.1°x0.1°, and a native resolution of 9 km. Data is available from 1950 to present.

Relative humidity and radiation were taken from HySN2018v2005ERA5 (Haddeland, 2022; Huang et al., 2022; Erlandsen et al., 2019). This meteorological dataset was created by combining data from both seNorge2018v20.05 and ERA5. The dataset is a newer and more extended version of HySN (Erlandsen et al., 2019). It includes the variables: downward shortwave and longwave radiation, as well as surface pressure and relative humidity. Although, longwave radiation

and surface pressure was not used in this study. The spatial grid-cell resolution of the dataset is 1x1 km^2 and the temporal resolution is daily values. Moreover, data is available from 1960 to 2020.

3.2 Observed discharge

In addition to the five model forcings, temperature, precipitation, wind speed, relative humidity and radiation, Shyft also needs observed discharge for calibration. Observed discharge time series measured at discharge stations Lalm and Elverum were found in the database of NVE. Discharge for Lalm was obtained from NVE (n.d.[b]) and for Elverum from NVE (n.d.[a]) and is shown in Figure 3.1. The observed discharge was available for the periods 1971-2022 and 1969-2022 for Lalm and Elverum, respectively. It is clear that Elverum has a considerably higher mean discharge, which is due to a larger catchment area, compared to Lalm. At Lalm, the flood peaks usually reach about 1000 m^3/s, while the peaks at Elverum generally stay below 2000 m^3/s. However, Elverum was subject to a huge flooding event during 1995. The maximum discharge was 3239 m^3/s, which occurred on the 2nd of June. Interestingly, Lalm did not experience any unusual flooding during this huge flood, judging by Figure 3.1.

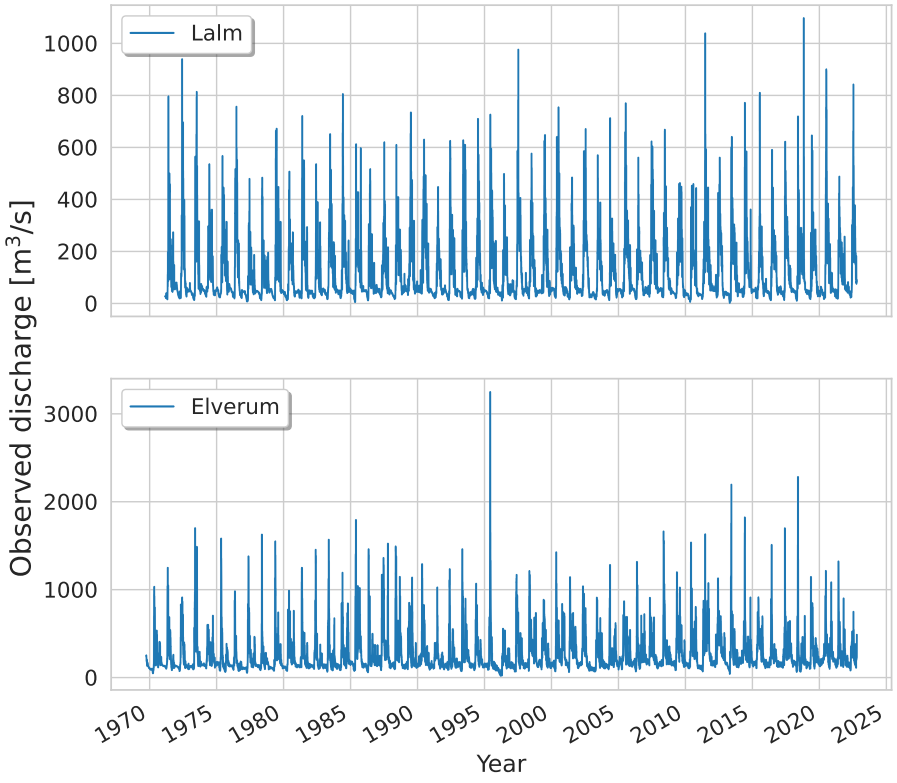

Figure 3.1: Observed daily discharge measured at Lalm and Elverum for the periods 1971-2022 and 1969-2022, respectively.

3.3 Climate model data

The climate model data of the past stem from a fast version of the NorESM1-F (Guo et al., 2019) simulations for the past 1000 years (from 851 to 1850) and historical simulations (from 1850 to 2005). The climate model data allow for discharge simulations for the three periods MWP, LIA and IT, by using the data as forcings to the hydrological model. Additionally, the data is at a daily timescale and at a horizontal resolution of around 2° and 1° for the atmosphere and land component, and for the ocean and sea ice component, respectively. The data is from the project Proxy Assimilation for Reconstructing Climate and Improving Model (PARCIM) that is hosted by Nansen Environmental and Remote Sensing Center (NERSC) (NERSC, 2022).

The past 1000 years climate model simulation consists of time-evolving forcings of solar radiation, volcanic aerosols, well-mixed greenhouse gases (GHGs) and orbital parameters. In the model experiments, two simulations of the past 1000 years were performed with different solar forcings, i.e., *Solar 1* scenario of low variability (Steinhilber et al., 2009) and *Solar 2* scenario of high variability (Egorova et al., 2018). However, there is no consensus yet, about which of the two solar-forcings that is "true" (R. Connolly et al., 2021). As a result, the climate model data for both Solar 1 and Solar 2 will be included in the study.

Moreover, the land cover and ozone concentrations are the same as for the pre-industrial experiment and the volcanic forcing is from Sigl et al. (2015) and implemented practically based on Bethke et al. (2017). Additionally, mixing ratios of GHGs based on the Community Climate System Model Version 4 (CCSM4) last millennium experiment following the PMIP3 protocol was used (Ault et al., 2013). The NorESM1-F historical simulation follows the CMIP5 protocol and includes time-varying well-mixed greenhouse gases, aerosols, ozone, volcanic and solar forcing (Guo et al., 2019). This historical simulation has been evaluated, which showed that it was able to capture the climate evolution of the 20th century reasonably well. More details are available in Guo et al. (2019).

Figure 3.2 shows the difference in Total Solar Irradiance (TSI) (R. Connolly et al., 2021) for the two solar variabilities Solar 1 and Solar 2. TSI is considerably lower for Solar 2, than compared to Solar 1, except for the two short periods of approximately 1775-1800 and 2000-present. For Solar, TSI fluctuates close to 1361, while it varies greatly between 1355 and 1360 for Solar 2. The difference between Solar 1 and Solar 2 is biggest during LIA and slightly smaller during MWP. During IT, the difference is considerably smaller.

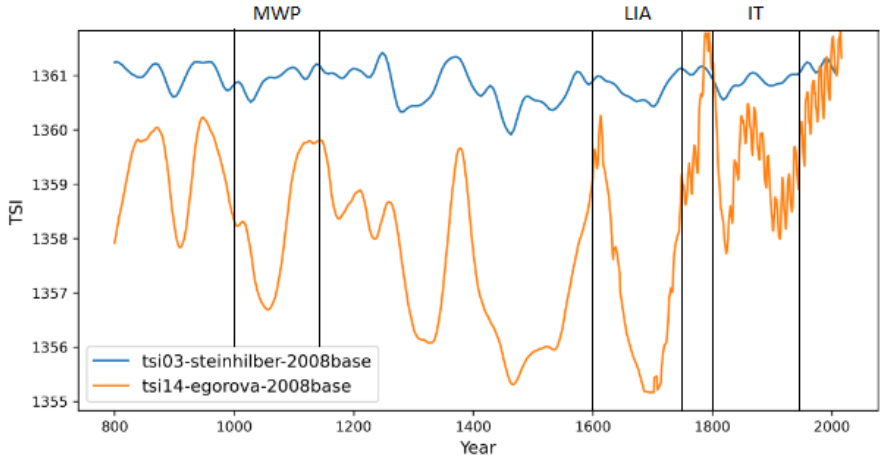

Figure 3.2: Time series of TSI for the past 1200 years, including MWP, LIA and IT. The blue line represents simulation with low variability (Solar 1) and the orange line represents simulation with high variability (Solar 2). Original figure shared by Chuncheng Guo.

3.4 Model elevation and land cover

Catchment elevation was obtained, as a Digital Elevation Model (DEM) with 1x1 km^2 spatial resolution, from the same database as the seNorge_2018 data (The Norwegian Meteorological institute, MET Norway, 2022). However, for wind speed (from ERA5-Land), elevation was calculated by using the modelled geopotential. From geopotential, elevation was obtained by division of the Earth's gravitational acceleration (g = 9.81 ms^{-2}). The modelled geopotential was downloaded from Hersbach et al. (2018). This data has a similar description as the wind speed, however, the resolution of the geopotential was only 0.25° x 0.25° as opposed to 0.1° x 0.1°. In order to fit the geopotential to the wind speed, the geopotential was interpolated using linear interpolation. The land cover characteristics (forest, lake and glacier fractions) were calculated based on Team et al. (2011), see Appendix A. No additional information about the river networks was required by Shyft.

3.5 Notation

In order to easier distinguish the different data used, the following notation is introduced: the meteorological forcing data is referred to as "observation-based data" and the climate model data is referred to as "paleo simulations" or "paleo simulated data".

CHAPTER 4

Methods

This chapter starts by describing the workflow of the study and the Shyft modelling framework used for creating the hydrological model. Secondly, the model evaluation criteria used for evaluating the hydrological model and bias correction approach used on the paleo simulations are described. Lastly, there are descriptions of the flood and extreme precipitation frequency analysis and the precipitation analysis of Storofsen.

4.1 Study design

An overview of the workflow of this study is shown in Figure 4.1. At first, the observation-based data, described in Section 3.1, was used to set up and configure a hydrological model using the Shyft modelling framework (Burkhart et al., 2021). An important note about notation: the Shyft modelling framework will be referred to as just "Shyft", while the hydrological model that was set up using Shyft will be referred to as the "Shyft model". The observation-based data was used for both calibrating and validating the Shyft model, and for creating a precipitation event for Storofsen. The paleo simulations were bias corrected (Section 4.4) and model forcings for MWP, LIA and IT were extracted (Section 4.5). Then, the Shyft model was used to simulate discharge for MWP, LIA and IT, and for simulating the Storofsen flood based on the precipitation event that was created (Section 4.7). The data output from the Shyft model was time series of discharge, snow parameters and model forcings for MWP, LIA and IT and discharge representing Storofsen. Lastly, these data were used for flood seasonality, frequency and magnitude analyses, comparisons to Storofsen and for precipitation analysis of Storofsen.

4.2 Shyft modelling framework

The hydrological modelling in this study was done using the modelling framework called Shyft. This is a streamflow forecasting software built for use in both research and hydropower production (Burkhart et al., 2021). Shyft offers a platform that is optimized for implementation of multiple well-known hydrological models from conceptual to physically based distributed hydrological models (Bhattarai et al., 2020). This separates Shyft from other hydrological models (Bhattarai et al., 2020).

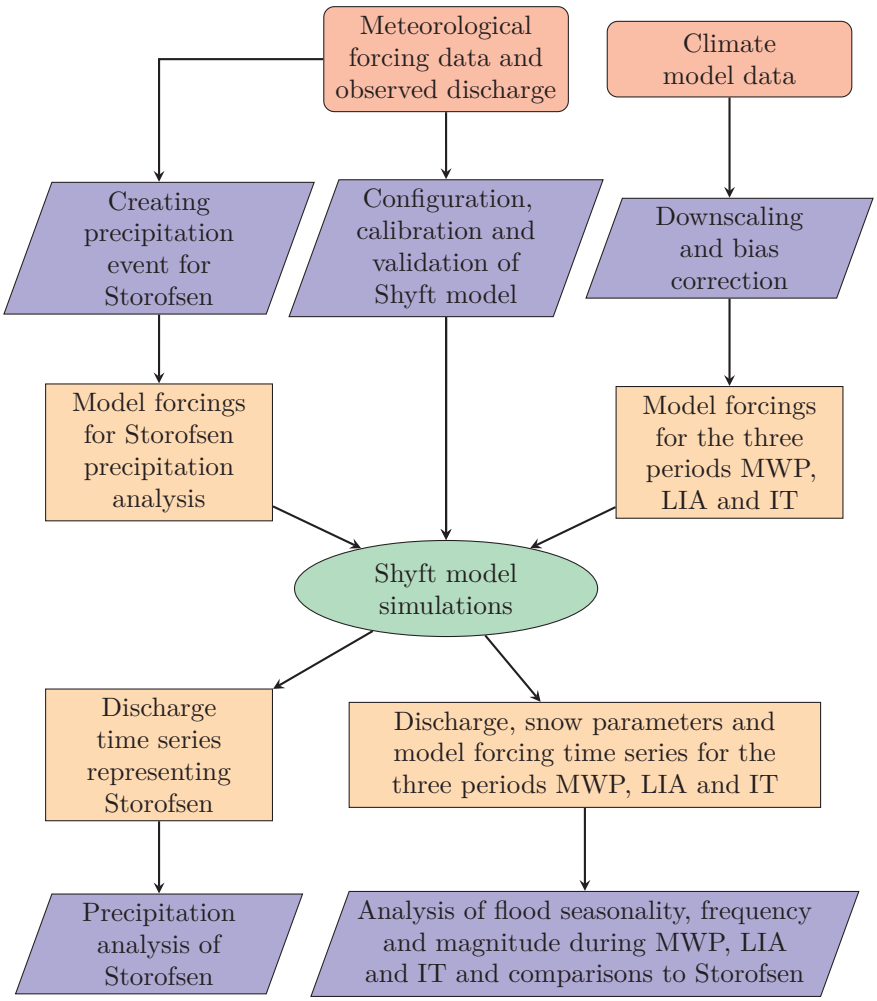

Figure 4.1: Conceptual figure showing the workflow behind the study. Red rectangles represent source data that was used in the thesis and blue trapezoids represent data processing. Orange rectangles represent new data that was obtained and the green ellipse represents the hydrological simulations performed with the Shyft model.

4.2.1 Hydrological model stack

Collections of hydrologic methods make up a hydrologic model, which in Shyft is referred to as a model stack (Burkhart et al., 2021). These different methods calculate the various processes that govern the hydrology in a region (i.e. evapotranspiration, snow routine, hydrologic response routine). The model stack used in this study is the Priestly Taylor Gamma Snow Kirchner (PTGSK) stack, as this is the only Shyft stack that offers an energy balance approach for snow accumulation and melt process calculation. This stack utilises calculations of evapotranspiration as described by Priestley and Taylor (1972), where temperature, radiation and relative humidity is used in order to calculate potential evaporation. Then, a simple scaling approach is applied in order to

estimate the actual evaporation based on the calculated potential evaporation, accounting for soil moisture deficits. Furthermore, it uses a snow routine from Kolberg et al. (2006). This is a routine based on energy balance, where a gamma function is used to model the sub-cell distribution of snow. In this routine, time series data of temperature, precipitation, wind speed, radiation and relative humidity are used in order to calculate snow accumulation and melt. Additionally, a simple temperature index approach from Hock (2003), is used to account for glacier melt. Lastly, PTGSK utilises a hydrologic response routine according to Kirchner (2009), in which the catchment response is calculated based on the snow and ice adjusted available liquid water (see Section 4.2.7 for description of river routing in Shyft).

Shyft does also provide six other model stacks, as seen in Figure 4.2. The routine Skaugen Snow (SS) is implemented according to Skaugen and Randen (2013) and Skaugen and Weltzien (2016). HBVstack is similar to the Hydrologiska Byråns Vattenbalansavdeling (HBV) model described in Bergström (1976). In addition, the routine HBV Snow (HS) is based on Lindström et al. (1997). The Radiation corrected algorithm (R) is based on Allen et al. (2006), while the Penman-Monteith evapotranspiration (PM) is available in full and standardized version from Walter et al. (2005). Lastly, the Snow Tiles (ST) algorithm is developed by Felix Matt (Burkhart et al., 2021).

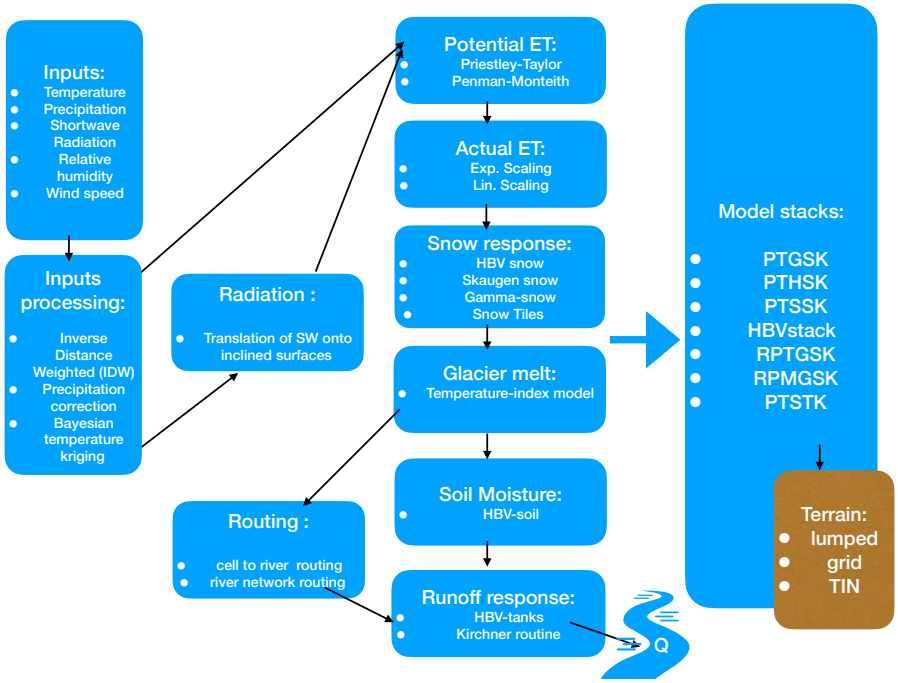

Figure 4.2: Flow chart showing the different routines and stacks in Shyft. Figure shared by Olga Silantyeva.

4.2.2 Required model forcings

The required model forcings that Shyft needs in order to simulate discharge are: (1) Air temperature, (2) Precipitation, (3) Wind velocity, (4) Relative humidity and (5) Down-welling solar radiation, as shown in Table 4.1.

Table 4.1: Model forcings required for running Shyft. Table from Burkhart et al. (2021).

Input variable	**Unit**	**Model stacks**
Temperature	°C	all model stacks
Precipitation	mm hr^{-1}	all model stacks
Wind speed	m s^{-1}	all model stacks
Relative humidity	%	PTGSK
Radiation	W m^{-2}	PTGSK

4.2.3 Output from the hydrological model

After running simulations with the Shyft model, the following variables can be extracted as output: discharge, temperature, precipitation, wind speed, relative humidity, radiation, Snow Water Equivalent (SWE) and Snow Covered Area (SCA). Snow melt is not an output variable from the Shyft model, although it was estimated by calculating the difference in SWE between two following days.

4.2.4 Interpolation

In Shyft the model region is made up of cells. The cells used in this study, have a spatial resolution of almost 2x2 km. In order to transfer the model forcing data from the source locations (e.g. grid points from atmospheric models or weather measuring stations) to the Shyft-cell locations, interpolation is performed. Thereafter, the hydrology of the region can be modelled by running a model stack cell-by-cell (Burkhart et al., 2021). Two different interpolation algorithms are implemented in Shyft: Inverse Distance Weighting (IDW) as described in Shepard (1968) and Bayesian Temperature Kriging (BTK). IDW is the main method that was used for distributing the model forcings to the region cells, as it was utilised on all forcings except for temperature. For temperature interpolation, the method of BTK was used.

4.2.5 Optimisation

In order to perform estimation of the model parameters, Shyft uses the two optimisation and global function search algorithms from *dlib* (King, 2009): *find_min_bobyqa* and *global_function_search*. The algorithm *find_min_bobyqa*, utilises Bound Optimization BY Quadratic Approximation (BOBYQA), which is an iteractive algorithm that is used for finding the minimum value of a function, that is subject to constrains on the variables (Powell, 2009). Additionally, the algorithm *global_function_search* conducts a global optimisation of a given function, that is subjected to constrains (Burkhart et al., 2021).

4.2.6 Grid cell attributes

In order for Shyft to perform any simulations it requires an input file containing information about the catchments. The information needed is latitude, longitude and elevation for each grid cell. Additional information is the forest, lake and glacier fraction within each grid cell (see Figure 2.7). These land cover fractions were calculated based on the land cover from Team et al. (2011), see Appendix A.

4.2.7 River routing

River routing is performed in two phases in Shyft: 1) cell-to-river routing and 2) river network routing (Burkhart et al., 2021). In 1) lateral inflow to the river is obtained by routing water from the cells to the closest river objects. In 2) water is routed from one river object to the next downstream river object, while there is also lateral inflow from the cells as described in 1). Upstream discharge and lateral inflow is summed and transferred to the next downstream river object. More detailed descriptions of routing in Shyft is described by Burkhart et al. (2021).

4.2.8 Calibration and validation of the hydrological model

The Shyft model was calibrated by using two different approaches. Firstly, a 2-fold cross calibration was performed, in order to check the robustness of the model. For Lalm, the two periods used for the 2-fold cross calibration was 1971-1996 and 1997-2022, while the two periods of 1969-1995 and 1996-2022 was used for Elverum. Afterwards, the Shyft model was calibrated on the complete observed discharge time series available from the measuring stations, which was 1971-2022 for Lalm and 1969-2022 for Elverum (see Section 3.2). This is referred to as the final calibration. All simulations performed with the Shyft model (except for the 2-fold cross validations) were done based on the final calibration. Table 4.2 shows all the calibration parameters and their corresponding range.

4.3 Model evaluation criteria

It is common practice in hydrological modelling to use various evaluation criteria in order to determine the accuracy and robustness of a particular model. These evaluation criteria are used during calibration and validation. They display in a single value how accurately the simulated discharge is compared to the observed discharge (Gupta et al., 2009).

4.3.1 Nash-Sutcliffe efficiency

The traditional efficiency coefficient, which is often used, is the Nash-Sutcliffe efficiency (NSE) (Nash and Sutcliffe, 1970). This evaluation approach is defined in Equation (4.1)

$$\mathrm{NSE} = 1 - \frac{\sum_{t=1}^{t=T}(Q_{obs}(t) - Q_{sim}(t))^2}{\sum_{t=1}^{t=T}(Q_{obs}(t) - \overline{Q_{obs}})^2} \tag{4.1}$$

Table 4.2: Range of the calibration parameters used for calibrating the Shyft model for both Lalm and Elverum.

Category	Parameter	Min	Max
ae	ae_scale_factor	1.5	1.5
gm	direct_response	0.0	0.0
	dtf	5.0	5.0
gs	calculate_iso_pot_energy	0	0
	fast_albedo_decay_rate	5.0	15.0
	glacier_albedo	0.4	0.4
	initial_bare_ground_fraction	0.04	0.04
	max_albedo	0.9	0.9
	max_water	0.1	0.1
	min_albedo	0.6	0.6
	n_winter_days	100	100
	slow_albedo_decay_rate	20.0	40.0
	snow_cv	0.4	0.4
	snow_cv_altitude_factor	0.0	0.0
	snow_cv_forest_factor	0.0	0.0
	snowfall_reset_depth	5.0	5.0
	surface_magnitude	30.0	30.0
	tx	-3.0	2.0
	wind_const	1.0	1.0
	wind_scale	1.0	6.0
	winter_end_day_of_year	100	100
kirchner	c1	-8.0	0.0
	c2	-1.0	1.2
	c3	-0.15	-0.05
msp	reservoir_direct_response_fraction	1.0	1.0
p_corr	scale_factor	0.5	2.0
pt	albedo	0.2	0.2
	alpha	1.26	1.26
routing	alpha	0.9	0.9
	beta	3.0	3.0
	velocity	0.0	0.0

where $Q_{obs}(t)$ is the observed discharge at time t, $Q_{sim}(t)$ is the simulated discharge at time t, $\overline{Q_{obs}}$ is the mean observed discharge and T is total number of time steps (Nash and Sutcliffe, 1970). A perfect model has NSE = 1. In this case the simulated discharge is equal to the observed discharge. If NSE = 0, it means that the model simulations explain as much as the mean of the observed discharge. When NSE < 0, it means that the mean observed discharge explain more than the model simulations. According to Yilmaz and Onoz (2020), NSE $\geq$ 0.7 is considered to be very good and 0.5 $\leq$ NSE < 0.7 is deemed to be good. The threshold value of NSE = 0 has been used to separate models that

are considered "good" and "bad" (Schaefli and Gupta, 2007).

4.3.2 Root mean square error

Models can also be evaluated by using the Root Mean Square Error (RMSE). RMSE is an evaluation indicator that is frequently used in hydrology, but also in meteorology as well as in climate research (Chai and Draxler, 2014; Ritter and Munoz-Carpena, 2013). RMSE is defined, as follows

$$\mathrm{RMSE} = \sqrt{\sum_{t=1}^{N} \frac{\left(Q_{sim}(t) - Q_{obs}(t)\right)^2}{N}} \tag{4.2}$$

where $Q_{obs}(t)$ is the observed discharge at time t, $Q_{sim}(t)$ is the simulated discharge at time t and N is total number of samples (Ritter and Munoz-Carpena, 2013). The range of RMSE goes from 0 to ∞, where 0 is a perfect model fit (Ritter and Munoz-Carpena, 2013). RMSE is the standard deviation of the residuals, thus it is a measure of how concentrated the residuals are around the line of best fit.

4.4 Bias correction

The paleo simulations (Section 3.3) had a coarser spatial resolution than the observation-based data (Section 3.1). As a result, the paleo simulations had to be downscaled into the same resolution as the observation-based data. The paleo simulations were downscaled by utilising nearest neighbour interpolation. This interpolation method maps each grid node with the value of the nearest neighbouring point (Desmet, 1997). The benefit of this interpolation approach is that the data retains it's original coarse looking structure. In contrast, other interpolation methods (e.g. linear and cubic interpolation) makes the data smoother, however, they both changes the structure of the data.

Outputs from Global Climate Models (GCMs) are typically subject to biases Tong et al. (2021). As a result, the data has to be bias corrected (Pierce et al., 2015). There are several bias correction methods available. Some examples are: linear, nonlinear, gamma-distribution and empirical distribution correction methods (Lafon et al., 2013). In this thesis, Quantile Delta Mapping (QDM) was used to bias correct the paleo simulations, as described by Tong et al. (2021). QDM bias correction is the equivalent to the equidistant and equiratio forms of the Quantile Mapping (QM) that is explained in Cannon et al. (2015), see Figure 4.3. In this study, the calibration period for bias correction was 1960-2020 and the projection period was 851-1959, while the model outputs are the paleo simulations. The first step in QDM is, to detrend by quantile (Equation (4.4) and Equation (4.7)) and bias correct to the observation-based data by QM (Equation (4.5)), the model outputs for the projection period (Cannon et al., 2015). Secondly, absolute/relative changes in quantiles for the projection period are superimposed on the bias corrected model outputs (Equation (4.6) and Equation (4.8)). The additive method was used for temperature and radiation, while the multiplicative method was used for precipitation, wind speed and relative humidity.

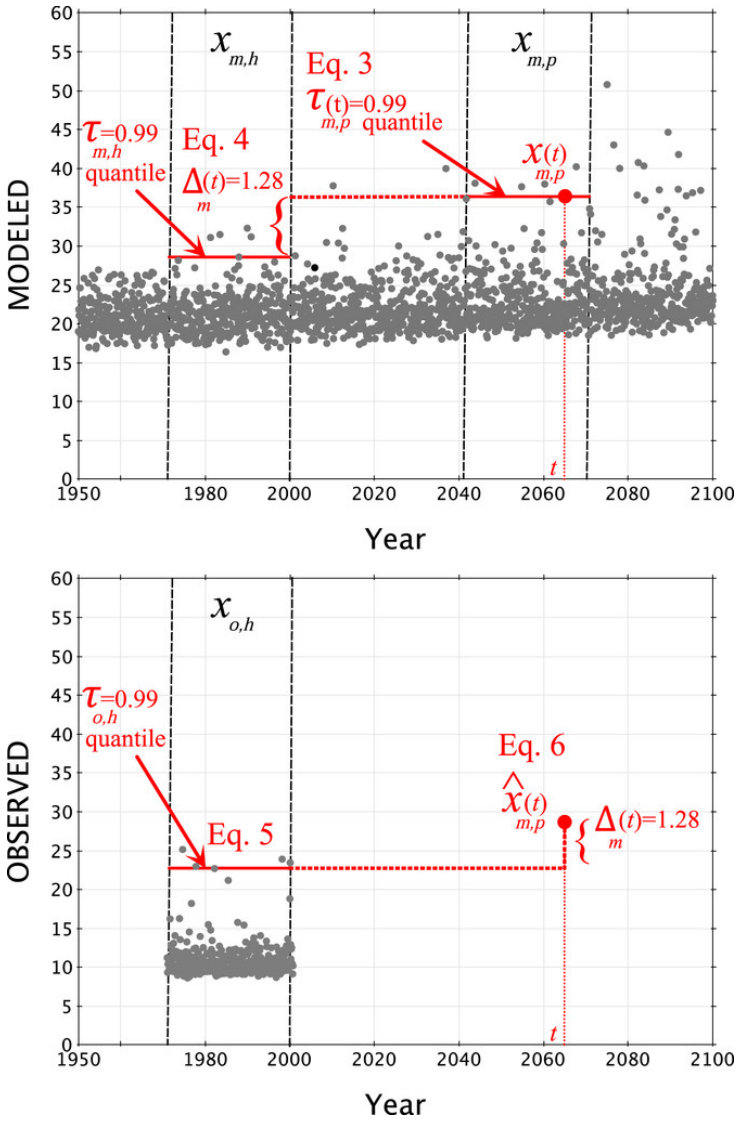

Figure 4.3: Illustration of QDM utilised on the modeled data point at $t = 2065$. At the top, there is modeled data for a historical (1971-2000) and projected (2041-2070) time window, denoted by dashed lines. At the bottom, there is simulated data for the historical period, which is used as base for the bias correction of modeled data. The labelled equations correspond to the equations presented in Cannon et al. (2015). The figure is taken from Cannon et al. (2015).

4.4.1 Additive method

The nonexceedance probability, $\varepsilon(t)$, related to a climate variable (i.e. temperature and radiation) at a given time t, is calculated by the equation

$$\varepsilon(t) = F^{(t)}_{sim,p}[x_{sim,p}(t)], \tag{4.3}$$

where $x_{sim,p}(t)$ is a simulated value at a time t that is within the projection period p (Tong et al., 2021). Moreover, the time-dependant Cumulative Distribution Function (CDF) $F^{(t)}_{sim,p}$ of the model projected series is estimated by mapping different distribution functions to the climate variables over a 30-year moving time window around t. The data used for calculating $F^{(t)}_{sim,p}$, was the paleo simulations for the period 851-1959. The nonexceedance probability has values within the interval $\varepsilon(t) \in \{0, 1\}$. Furthermore, the absolute quantile change between the calibration period and the projection period is

$$\phi(t) = F^{(t)-1}_{sim,p}[\varepsilon(t)] - F^{-1}_{sim,c}[\varepsilon(t)] = x_{sim,p}(t) - F^{-1}_{sim,c}\{F^{(t)}_{sim,p}[x_{sim,p}(t)]\}, \tag{4.4}$$

where $F^{-1}_{sim,c}$ denotes the inverse CDF of the simulations from the calibration periods (Tong et al., 2021). The data used for calculating $F^{-1}_{sim,c}$, was the paleo simulations for the period 1960-2020. Furthermore, the QM bias correction, $\hat{x}(t)$, for the calibration period t is calculated based on the equation

$$\hat{x}(t) = F^{-1}_{obs,c}[\varepsilon(t)], \tag{4.5}$$

where $F^{-1}_{obs,c}$ denotes the inverse CDF obtained from the observed values $x_{obs,c}$ at the calibration periods (Tong et al., 2021). The data used for calculating $F^{-1}_{obs,c}$, was the observation-based data for the period 1960-2020. Finally, the QDM bias corrected data is calculated as follows

$$\hat{x}_{bc}(t) = \hat{x}(t) + \phi(t), \tag{4.6}$$

where $\hat{x}(t)$ is the QM bias correction and $\phi(t)$ is the absolute change in quantiles (Tong et al., 2021).

4.4.2 Multiplicative method

In contrast to temperature, precipitation can never be negative. Additionally, precipitation may vary many orders of magnitude at different locations. As a consequence of this, a multiplicative bias correction method is more commonly used for performing bias correction on climate variables similar to precipitation (Beyer et al., 2020).

The multiplicative method shares the same calculations of the nonexceedance probability, $\varepsilon(t)$ (Equation (4.3)), and the QM bias correction, $\hat{x}(t)$ (Equation (4.5)), as the additive method. However, the relative quantile change between the calibration period and the model projected time t is expressed as

$$\phi(t) = \frac{F_{sim,p}^{(t)-1}[\epsilon(t)]}{F_{sim,c}^{-1}[\epsilon(t)]} = \frac{x_{sim,p}(t)}{F_{sim,c}^{-1}\{F_{sim,p}^{(t)}[x_{sim,p}(t)]\}}, \tag{4.7}$$

where $F_{sim,c}^{-1}$ again denotes the inverse CDF of the simulations from the calibration periods (Tong et al., 2021). The data used for calculating $F_{sim,c}^{-1}$, was the paleo simulations for the period 1960-2020. Finally, the QDM bias corrected data is calculated using the equation

$$\hat{x}_{bc}(t) = \hat{x}(t)\phi(t), \tag{4.8}$$

where $\hat{x}(t)$ is the QM bias correction and $\phi(t)$ is the relative change in quantiles (Tong et al., 2021).

4.4.3 Distribution functions

The Normal distribution is often assumed to fit temperature best and it has previously been used for bias correcting temperature data (Fang et al., 2015). The Normal distribution is expressed by Equation (4.9).

$$f(x) = \frac{1}{\sigma\sqrt{2\pi}} e^{-(x-\mu)2/2\sigma^2}, \quad -\infty < x < \infty, \tag{4.9}$$

where μ is the location parameter and σ is the scale parameter (Ahsanullah et al., 2014). For the Normal distribution, the parameter μ is the mean and σ is the standard deviation.

The Gamma distribution has been assumed to be a suitable distribution for precipitation events (Teutschbein and Seibert, 2012). In fact, wind speed has similar characteristic properties as precipitation (Yang et al., 2015). As a result of this, the Gamma distribution is used for bias correcting both precipitation and wind speed. Equation (4.10) shows the expression for the Gamma distribution.

$$f(x|\alpha,\beta) = x^{\alpha-1} \cdot \frac{1}{\beta^\alpha \cdot \Gamma(\alpha)} \cdot e^{\frac{-x}{\beta}}; \quad x \geq 0; \quad \alpha,\beta > 0, \tag{4.10}$$

where α is the shape parameter and β is the scale parameter (Thom, 1958). The shape and scale parameters control the properties of the Gamma distribution (Teutschbein and Seibert, 2012). Moreover, the profile of the distribution is determined by the shape parameter. If $a < 1$, the Gamma distribution will be exponentially shaped and asymptotic at both of the axes. Furthermore, the distribution will be exponential for $a = 1$. On the other hand, if the shape parameter is $a > 1$, the Gamma distribution turns into a skewed unimodal distribution curve. The scale parameter alters the distribution by changing its

dispersion. Smaller values of β reduces the probability of extreme events, since the distribution will be more compressed in this case. The opposite occurs for larger values of β, since the distribution will be more stretched, thus increasing the probabilities of extreme events.

Relative humidity is different from the other climate variables, in the sense that the values fall inside the interval of [0,1]. Due to this particular property, the Beta distribution is used for correcting the relative humidity data (Yang et al., 2015). The Beta distribution is written as

$$f(x) = \left[\frac{\Gamma(p+q)}{\Gamma(p)\Gamma(q)}\right] x^{p-1}(1-x)^{q-1} \tag{4.11}$$

where Γ is the gamma function, while p and q are the distribution parameters that determine the shape of the distribution (Yang et al., 2015). The Beta distribution is positively skewed for $p < q$ and negatively skewed for $p > q$ (Yao, 1974). For $p = q$, the distribution is symmetric. Equation (4.12) and Equation (4.13) display how the distribution parameters p and q can be fitted, respectively.

$$\mu = \frac{p}{p+q} \tag{4.12}$$

$$\sigma^2 = \frac{pq}{(p+q)^2(p+q+1)}, \tag{4.13}$$

where μ is the mean and σ is the standard deviation (Yang et al., 2015).

After bias correction, precipitation values below 0.1 mm/day (dry days), were set to zero, in order to adjust for the amount of wet days (Lindau and Simmer, 2013).

4.4.4 Goodness of fit measures

The goodness of fit of the bias correction is evaluated using mean absolute error (MAE) and mean relative error (MRE). All model forcings were evaluated by using the MRE, except for temperature. MAE was used for evaluating temperature, since temperature can take negative values. The closer both MAE and MRE are to zero, the better the goodness of fit is for the simulated values. MAE = 0 and MRE = 0 indicates a perfect fit between the observed and simulated values. The equation for MAE is defined as follows

$$\text{MAE} = \frac{1}{n}\sum_{i=1}^{n} |y_i - x_i|, \tag{4.14}$$

where n is the number of values, y_i and x_i is the observed and simulated value at point i, respectively. The equation for MRE is expressed as

$$\text{MRE} = \frac{\sum_{i=1}^{n} |y_i - x_i|}{\sum_{i=1}^{n} |y_i|}, \tag{4.15}$$

where n is the number of values, y_i and x_i is the observed and simulated value at point i, respectively.

4.5 Paleo simulation period division

The paleo simulations goes back to AD 851. Between AD 851 and 2020 there has been to distinct climate periods. From 950-1250 there was an unusually warm period, often referred to as the "Medieval Warm Period" (Markonis et al., 2012). Furthermore, there was a cooling period between AD 1500-1800, known as "Little Ice Age" (Huo et al., 2022). After AD 1800 the industrial revolution was already blooming, which by many has been suspected to cause a another warm period. However, when comparing flood statistics between different periods, it is essential to select periods of the same time scale, since the time scale significantly affects the extreme discharge statistics (Huo et al., 2022). As a result, three periods were extracted from the paleo simulations: 1000-1150 which represents MWP, 1600-1750 representing LIA and 1800-1950 for the period after the beginning of the industrial revolution, referred to as Industrial Time (IT).

4.6 Flood and extreme precipitation frequency analysis

Flood and extreme precipitation quantiles were estimated by using a Bayesian approach to fit a distribution to the annual maximum discharge and precipitation, respectively. The Bayesian approach is flexible, it allows for giving prior information of the shape parameter and uncertainty assessments for quantile estimates. For this approach, non-informative priors were applied for the location and scale parameter. In contrast, for the shape parameter, an *a priori* standard deviation of 0.2 and an expected value of 0, were given. This was done in order to get more reasonable estimates. Additionally, to make sure the estimation of the shape parameter was robust, a variance parameter for the "proposal distribution" was set to 0.01. This variance parameter is for the Markov Chain Monte Carlo (MCMC) algorithm. The calculations were done by using the *BayesianMCMC*-function from the R-package *nsRFA* (Viglione et al., 2020). The data was fitted to the Generalized Extreme Value (GEV) distribution (Jenkinson, 1955). The GEV distribution combines three extreme value distributions, Gumbel, Frechet and Weibull, into one framework (Ailliot et al., 2011). Equation (4.16) shows the equation of GEV

$$F(x) = \begin{cases} \exp\left\{-\left[1+\kappa\left(\frac{x-\beta}{\alpha}\right)\right]^{-1/\kappa}\right\}, & \kappa \neq 0 \\ \exp\left\{-\exp\left(-\frac{x-\beta}{\alpha}\right)\right\}, & \kappa = 0 \end{cases} \tag{4.16}$$

where β, α and κ are the location, scale and shape parameter, respectively (Ailliot et al., 2011). The Frechet distribution is obtained when $\kappa < 0$, while the Weibull distribution is obtained for $\kappa > 0$. Moreover, $\kappa = 0$ yields the Gumbel distribution.

4.7 Precipitation analysis of Storofsen

Storofsen is thought to have been a rainfall dominated flooding event (Roald, 2013). In order to investigate what precipitation amount could have produced a flood of such magnitude two approaches were utilised. The first and simplest approach was to calculate the specific discharge for both Lalm and Elverum. This was done by dividing the peak flood discharge, found in literature (Engeland et al., 2018; Engeland et al., 2020), by the catchment area. This approach gives a general idea of how much average precipitation was required to cause the flood. The other, more advanced approach was to create a precipitation event similar to what is described in the literature (Østmoe, 1985) and use the Shyft model to simulate how much precipitation was required to yield such a flood. As described in Østmoe (1985), rain began on July 20th of 1789. The rain intensified on July 21st and peaked on the 22nd, before decreasing on the 23rd. This precipitation event was created based on the observation-based precipitation at both Lalm and Elverum. Then the mean precipitation was increased in order to match the event described in the literature. Additionally, the Standard Precipitation Index (SPI) (McKee et al., 1993; McKee et al., 1995) was used in order to identify in which months the soil conditions were wet and dry. Based on these initial conditions, three separate simulations were performed for each catchment in order to compare the event precipitation that caused Storofsen.

4.7.1 Standard Precipitation Index

SPI is a measure used to identify periods of climatic variability (Khan et al., 2008). Moreover, SPI shows whether there are wet or dry land conditions based on monthly precipitation (McKee et al., 1993). There are wet conditions for SPI > 0, dry conditions for SPI < 0 and normal conditions for SPI $= 0$. SPI was estimated by using the function *spi* from the R-package *SPEI*, which is documented in (Beguería et al., 2017). A time scale of 3 months were chosen for the estimation, since this is the shortest time scale showcased in McKee et al. (1993), and it yields the most rapidly varying, detailed results.

CHAPTER 5

Results

This chapter presents the results, starting with the goodness of fit of the bias correction and the quality of the Shyft model. Secondly, the seasonality and flood characteristics during MWP, LIA and IT are presented. Lastly, the chapter includes a precipitation analysis of Storofsen. In order to avoid any confusion the notations are introduced for the rest of the thesis: "observations/observed" refers to the Shyft model output with the observation-based data as forcings, while "simulations/simulated" refers to the Shyft model output with the QDM bias corrected paleo simulations as forcings.

5.1 Bias correction of climate model data

The paleo simulations were bias corrected, in order to reduce the bias compared to the observation-based data. Table 5.1 shows the bias between the paleo simulations and the observation-based data before and after bias correction. For all model forcings, for both Lalm and Elverum catchment, the bias was substantially reduced. The bias was <1.0 for all variables. At both catchments, the paleo simulated temperature was several degrees higher than the observation-based temperature before the correction and less than 1 degree colder after correction. In contrast, paleo simulated precipitation, relative humidity and radiation had considerably less bias pre-correction and even less (<0.1) post-correction. The wind speed bias was around a couple of meters per second before correction and <0.1 after correction.

Table 5.2 and Table 5.3 compares the mean and standard deviation of the observation-based forcings and the bias corrected paleo simulated forcings. The model forcings with the biggest difference in mean is radiation and temperature. E.g. for Lalm, the observation-based mean radiation is 113.2 Wm^{-2}, and the Solar 1 and Solar 2 paleo simulated corrected radiation is 111.3 Wm^{-2} and 111.1 Wm^{-2}, respectively. In addition, the observation-based temperature mean is $-2.1°C$, while the paleo simulated temperature mean is $-2.8°C$ with Solar 1 and $-3.1°C$ with Solar 2. For both catchments, the paleo simulated temperature mean using Solar 1 is closer to the observation-based temperature mean than for Solar 2. Furthermore, the difference between observation-based and corrected paleo simulated mean precipitation, wind speed and relative humidity is small for both Lalm and Elverum.

Table 5.1: Catchment average goodness of fit values of bias correction. Temperature bias was evaluated by MAE and has °C as unit, while all the other variables were evaluated by MRE, thus their biases are dimensionless. The bias was calculated for the period 851-1959 for all variables.

		Solar 1		Solar 2	
Catchment	**Variable**	**Pre**	**Post**	**Pre**	**Post**
Lalm	Temperature	-5.63	0.73	-5.37	0.99
	Precipitation	-0.28	0.09	-0.27	0.09
	Wind speed	-2.27	0.02	-2.28	0.02
	Relative humidity	0.54	0.02	0.54	0.02
	Radiation	0.22	0.02	0.23	0.02
Elverum	Temperature	-3.78	0.72	-3.52	0.98
	Precipitation	-0.45	0.07	-0.45	0.07
	Wind speed	-1.33	0.02	-1.34	0.02
	Relative humidity	0.53	0.05	0.53	0.03
	Radiation	0.13	0.02	0.13	0.02

Similarly to the mean, the standard deviation difference between the observation-based and bias corrected paleo simulated forcings is the smallest for precipitation wind speed and relative humidity. The difference is the largest for temperature and radiation. At both catchments, the temperature and radiation for the observation-based data has a smaller standard deviation than for the paleo simulations. The observation-based temperature standard deviation for Elverum was 9.0°C, while for the Solar 1 and Solar 2 paleo simulated temperature was 9.6°C. Additionally, the standard deviation of observation-based radiation is 90.2 Wm^{-2}, and 92.5 Wm^{-2} for the Solar 1 paleo simulations and 92.3 Wm^{-2} for the paleo simulations using Solar 2.

Table 5.2: Mean of observation-based model forcings and bias corrected paleo simulated forcings. S1 and S2 refers to Solar 1 and Solar 2. Observation-based data are from 1960-2020 and paleo simulations from 851-1959.

Catchment	**Variable**	**Unit**	**Obs**	**S1**	**S2**
Lalm	Temperature	°C	-2.1	-2.8	-3.1
	Precipitation	mm hr^{-1}	0.1	0.1	0.1
	Wind speed	m s^{-1}	1.4	1.4	1.4
	Relative humidity	-	0.8	0.8	0.8
	Radiation	W m^{-2}	113.2	111.3	111.1
Elverum	Temperature	°C	-0.2	-0.9	-1.2
	Precipitation	mm hr^{-1}	0.1	0.1	0.1
	Wind speed	m s^{-1}	1.7	1.6	1.6
	Relative humidity	-	0.8	0.8	0.8
	Radiation	W m^{-2}	105.3	103.7	103.6

Table 5.3: Standard deviation of observation-based model forcings and bias corrected paleo simulated forcings. S1 and S2 refers to Solar 1 and Solar 2. Observation-based data are from 1960-2020 and paleo simulations from 851-1959.

Catchment	Variable	Unit	Obs	S1	S2
Lalm	Temperature	°C	8.4	9.0	9.1
	Precipitation	mm hr^{-1}	0.3	0.2	0.2
	Wind speed	m s^{-1}	0.8	0.7	0.7
	Relative humidity	-	0.1	0.1	0.1
	Radiation	W m^{-2}	94.7	96.9	96.6
Elverum	Temperature	°C	9.0	9.6	9.6
	Precipitation	mm hr^{-1}	0.2	0.1	0.1
	Wind speed	m s^{-1}	0.9	0.9	0.9
	Relative humidity	-	0.1	0.2	0.2
	Radiation	W m^{-2}	90.2	92.5	92.3

5.1.1 Seasonal mean and standard deviation

Figure 5.1 shows the seasonal mean and standard deviation of the observation-based, paleo simulated and bias corrected paleo simulated model forcings for Lalm with Solar 1. Similar figures for Lalm and Elverum with Solar 2 is shown in Appendix A. Overall, the seasonal mean and standard deviation of the paleo simulations are more similar to the observation-based forcings after bias correction. However, for December, January and February the precipitation mean was 280.8 mm/season for the observation-based forcings and the paleo simulations. After bias correction, precipitation for the winter period was reduced to 194.4 mm/season. In addition, the observation-based winter radiation mean was 19.2 Wm^{-2} and the paleo simulated mean was 14.4 Wm^{-2}. After bias correction, the paleo simulated mean was increased to 25.1 Wm^{-2}. In other words, the difference between the observation-based forcings and the paleo simulations went from 4.8 Wm^{-2} before correction to 6.0 Wm^{-2} after correction. Figures that show the difference between Solar 1 and Solar 2 temperature and precipitation time series are included in Appendix A.

Figure 5.2 shows the seasonal mean and standard deviation of the observation-based, paleo simulated and bias corrected paleo simulated model forcings for Elverum with Solar 1. Similarly to the results from Lalm using Solar 1, seasonal mean and standard deviation is closer to the observation-based forcings for the paleo simulations after bias correction than compared to before correction. However, paleo simulations of mean precipitation during June, July and August was reduced during bias correction. The observation-based mean precipitation was 238.5 mm/season, while it was 251.1 mm/season for the paleo simulations and 160.2 mm/season for the bias corrected paleo simulations. This means that difference in mean precipitation between the observation-based forcings and the paleo simulations went from 12.6 mm/season to 90.9 mm/season after bias correction. Additionally, the difference in the observation-based mean radiation compared to the paleo simulations in December, January and February were slightly increased after bias correction. The observation-based mean radiation

was 18.4 Wm^{-2} and 15.1 Wm^{-2} for the paleo simulations, while it was 22.1 Wm^{-2} for the bias corrected paleo simulations. This means that the difference went from 3.3 Wm^{-2} before correction to 3.7 Wm^{-2} after correction.

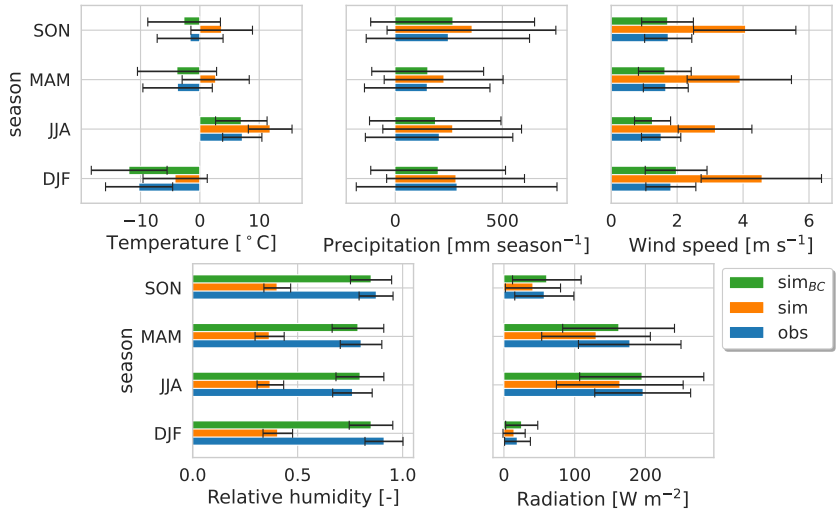

Figure 5.1: Seasonal mean and standard deviation for Lalm with Solar 1. Bars represent means and error bars represent standard deviations. The notation *BC* denotes bias corrected. Observation-based data are from 1960-2020 and paleo simulations from 851-1959.

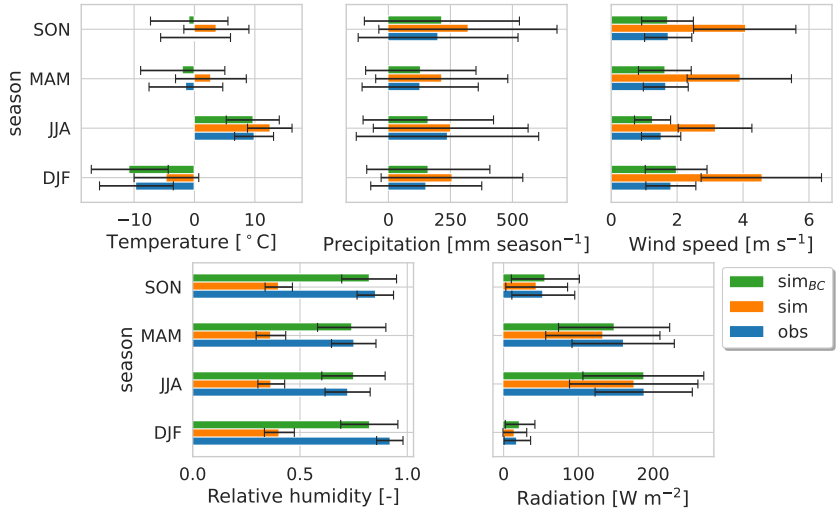

Figure 5.2: Seasonal mean and standard deviation for Elverum with Solar 1. Bars represent means and error bars represent standard deviations. The notation *BC* denotes bias corrected. Observation-based data are from 1960-2020 and paleo simulations from 851-1959.

5.2 Calibration and validation of the hydrological model

The calibrated Shyft model parameters for Lalm and Elverum after the final calibration (see Section 4.2.8) are shown in Table 5.4. Most of the parameters were the same for both catchments. The parameters that varied between the two catchments were: fast_albedo_decay_rate, slow_albedo_decay_rate, tx, wind_scale and the Kirchner hydrologic response routine parameters c1, c2 and c3.

Table 5.4: Calibration parameter values after final calibration of the Shyft model for Lalm and Elverum.

Category	**Parameter**	**Lalm**	**Elverum**
ae	ae_scale_factor	1.5	1.5
gm	direct_response	0.0	0.0
	dtf	5.0	5.0
gs	calculate_iso_pot_energy	false	false
	fast_albedo_decay_rate	10.5	5.0
	glacier_albedo	0.4	0.4
	initial_bare_ground_fraction	0.04	0.04
	max_albedo	0.9	0.9
	max_water	0.1	0.1
	min_albedo	0.6	0.6
	n_winter_days	100	100
	slow_albedo_decay_rate	31.38	20.61
	snow_cv	0.4	0.4
	snow_cv_altitude_factor	0.0	0.0
	snow_cv_forest_factor	0.0	0.0
	snowfall_reset_depth	5.0	5.0
	surface_magnitude	30.0	30.0
	tx	-2.43	-2.07
	wind_const	1.0	1.0
	wind_scale	4.36	4.49
	winter_end_day_of_year	100	100
kirchner	c1	-4.43	-3.88
	c2	0.12	0.68
	c3	-0.10	-0.05
msp	reservoir_direct_response_fraction	1.0	1.0
p_corr	scale_factor	0.86	0.86
pt	albedo	0.2	0.2
	alpha	1.26	1.26
routing	alpha	0.9	0.9
	beta	3.0	3.0
	velocity	0.0	0.0

The result of the Shyft model simulations is summarised in Table 5.5. The final calibration of the model on the full observed discharge period (1971-2020 for Lalm and 1969-2020 for Elverum), yielded very good NSE values for both catchments, with 0.83 and 0.81 for Lalm and Elverum, respectively. In this case, Lalm has lower RMSE (48.31) compared to Elverum (95.02). For the 2-fold cross validation, Lalm has very good NSE overall (NSE ≥ 0.7), even for the validation periods. In contrast, Elverum has NSE = 0.65 for the 1995-2020 validation period, even though the 1969-1995 calibration period had a very good model efficiency (NSE = 0.83). Additionally for the 1995-2020 validation period, the RMSE is high at 130.3. Furthermore, for the 1995-2020 calibration period, NSE is surprisingly low at 0.68. However, the 1969-2020 validation period has a very good efficiency of (NSE = 0.78). Elverum was subject to a large flood in 1995, which was thought to be the reason that the validation NSE was higher then for the calibration. Thus another calibration and validation was performed, where the validation period was expanded to include the 1995 flooding. Even after including the 1995 flood in the validation period, instead of in the calibration period, NSE was still higher in the former.

Table 5.5: Efficiency coefficients of the Shyft model calibration. RMSE has m^3/s as unit. * Denotes the calibration and validation with the 1995 flood in the validation period, instead of in the calibration period.

Catchment	**Period**	**Type**	**NSE**	**RMSE**
Lalm	1971-2020	Calibration	0.83	48.31
	1971-1996	Calibration	0.82	49.73
	1996-2020	Validation	0.74	60.10
	1996-2020	Calibration	0.77	56.52
	1971-1996	Validation	0.75	57.89
Elverum	1969-2020	Calibration	0.81	95.02
	1969-1995	Calibration	0.83	89.09
	1995-2020	Validation	0.65	130.3
	1995-2020	Calibration	0.68	124.4
	1969-1995	Validation	0.78	101.0
	1995-2020*	Calibration	0.73	107.2
	1969-1995*	Validation	0.80	102.6

Figure 5.3 and Figure 5.4 show the simulated daily discharge of the calibration and validation periods compared to the observed discharge for Lalm and Elverum, respectively. The NSE and RMSE coefficients for the calibration and validation simulations are shown in Table 5.5. For Lalm, the observed discharge only exceeds 1000 m^3/s once. This happened on the 11th of June 2011, when the discharge was 1019 m^3/s. Additionally, the discharge was 998 m^3/s on the 15th of October 2018. In contrast, the simulated discharge goes above 1000 m^3/s twice, although within the same flood event. This event occurred on the 20th and 21st of June 2020, where the discharge was 1014 and 1042 m^3/s, respectively (1971-2020 calibration period).

In June 1995, there was an extreme flooding event, which is prominent in the Elverum observed discharge time series. On the 2nd of June 1995 the observed discharge was 3185 m^3/s, while the simulated discharge was 3183 m^3/s

(1969-2020 calibration). However, for the 2-fold cross validation, the 1995 flood event is not very accurately simulated.

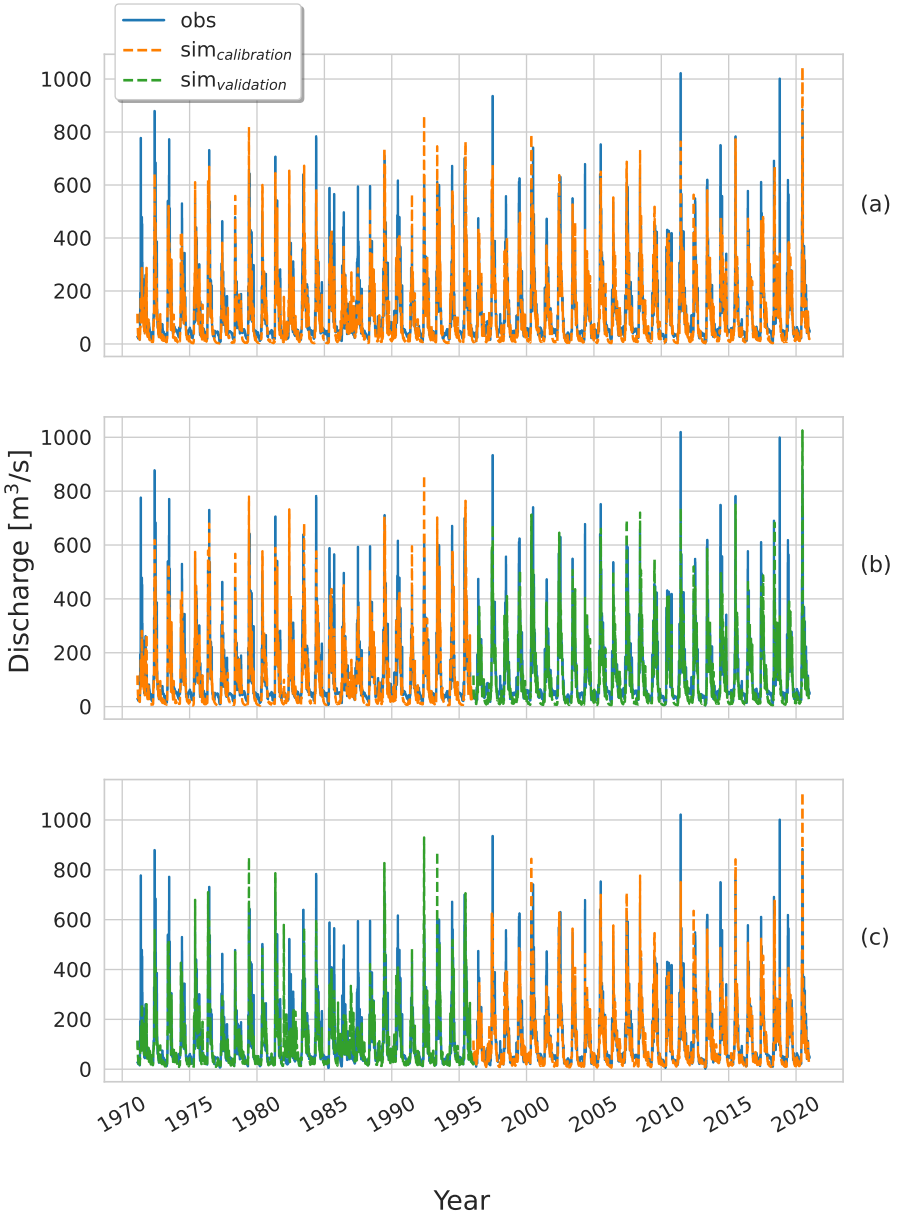

Figure 5.3: Shyft model calibration at Lalm: (a) final calibration and (b)-(c) 2-fold cross calibration and validation.

Figure 5.5 shows how accurately the model simulates the peak floods. When looking at the 150 highest observed flood peaks, there is a slight underestimation of the corresponding simulated discharge for both catchments. For the annual maximum floods, there is a slight underestimation of the simulated floods, but only noticeable at Lalm. There is also a small underestimation of the 150

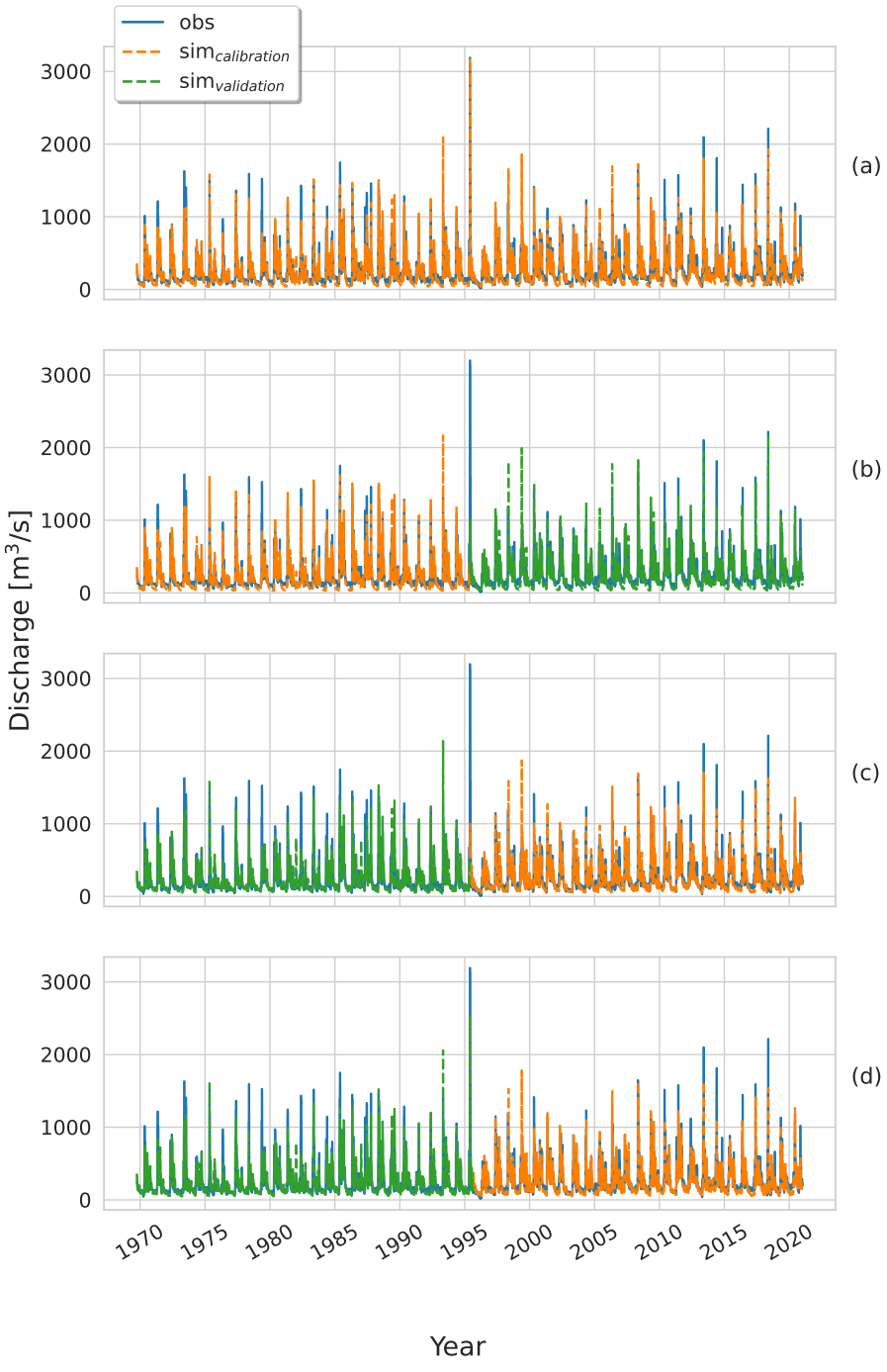

Figure 5.4: Shyft model calibration at Elverum: (a) final calibration, (b)-(c) 2-fold cross calibration and validation and (d) calibration and validation with the 1995 flood in the validation period.

highest simulated peak floods compared to the 150 highest observed peak floods at Lalm, and a barely noticeable underestimation at Elverum. Interestingly, the 1995 flood (at 3185 m^3/s) is precisely simulated for Elverum.

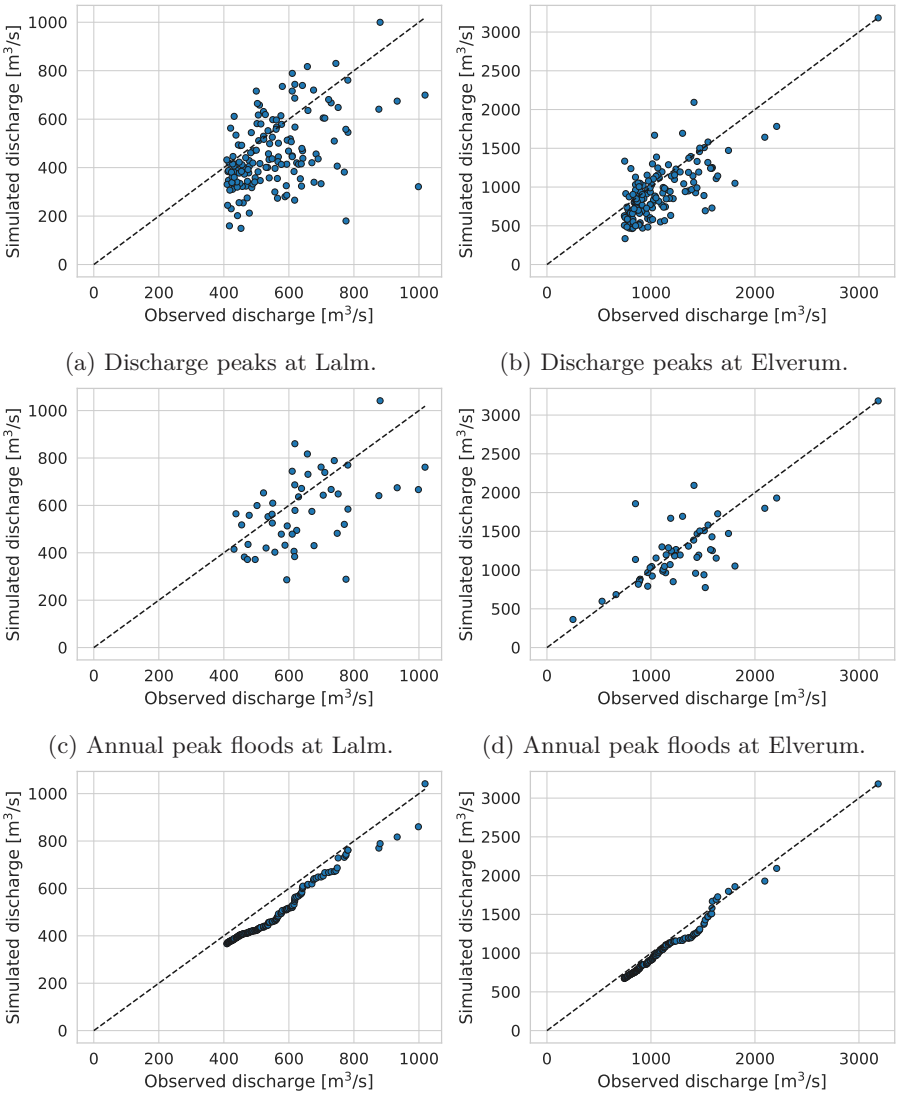

(a) Discharge peaks at Lalm.

(b) Discharge peaks at Elverum.

(c) Annual peak floods at Lalm.

(d) Annual peak floods at Elverum.

(e) Discharge peaks at Lalm.

(f) Discharge peaks at Elverum.

Figure 5.5: Figures (a)-(f) compares the observed and simulated peak discharge at Lalm and Elverum. In (a) and (b), the 150 highest observed peaks are plotted against the corresponding simulated peaks. For (c) and (d), the observed annual maximum discharge is plotted against the simulated annual maximum. Lastly, in (e) and (f) the 150 highest observed discharge peaks are plotted against 150 highest simulated peaks.

5.3 Seasonality of paleo simulations

5.3.1 Mean discharge, temperature and precipitation

The mean discharge, temperature and precipitation simulated for the three periods MWP, LIA and IT, and for observations are shown in Table 5.6, Table 5.7 and Table 5.8, respectively. At Lalm, the mean discharge is slightly overestimated compared to the observations, while there is a slight underestimation at Elverum. Mean temperature is underestimated at both catchments, and LIA is colder than MWP for every simulation, although the difference is only 0.1°C. IT has the same mean temperature as LIA for both solar 1 simulations. Simulated precipitation is a bit higher than observed precipitation at Lalm and vice versa at Elverum.

Table 5.6: Mean discharge [m^3/s]. S1 and S2 refers to Solar 1 and Solar 2.

Station	S	MWP	LIA	IT	Obs
Lalm	1	122.0	121.8	122.1	105.6
	2	119.9	117.9	122.3	105.6
Elverum	1	231.7	231.9	230.9	243.3
	2	230.2	229.3	233.3	243.3

Table 5.7: Mean temperature [°C]. S1 and S2 refers to Solar 1 and Solar 2.

Station	S	MWP	LIA	IT	Obs
Lalm	1	-2.6	-2.7	-2.7	-1.4
	2	-3.1	-3.2	-2.7	-
Elverum	1	-1.0	-1.1	-1.1	0.8
	2	-1.5	-1.6	-1.2	-

Table 5.8: Mean precipitation [mm/yr]. S1 and S2 refers to Solar 1 and Solar 2.

Station	S	MWP	LIA	IT	Obs
Lalm	1	914.7	911.8	912.9	877.6
	2	902.6	891.4	916.7	-
Elverum	1	679.2	680.7	676.4	722.2
	2	674.7	671.7	682.0	-

The fraction of wet and dry days are shown in Table 5.9. It is clear that the fraction of wet and dry days for the simulation are very comparable to observations at Lalm. In contrast, the difference between the simulation and observations are somewhat bigger at Elverum. The period with the lowest wet day fraction was MWP and LIA with Solar 2 at Lalm (0.43) and at Elverum the lowest wet day fraction was found in MWP (Solar 2) and IT (Solar 1; 0.38). On the other hand, the highest wet day fraction was in IT (Solar 2; 0.44) at Lalm and in LIA (Solar 1) and IT (Solar 2; 0.39) at Elverum.

Table 5.9: Fraction of wet and dry days to total amount of days in each period. Threshold precipitation value that separates wet and dry days is 1 mm/day. Subscripts 1 and 2 denotes Solar 1 and Solar 2, respectively

Station	Period	Wet	Dry
Lalm	MWP_1	0.44	0.57
	MWP_2	0.43	0.57
	LIA_1	0.43	0.57
	LIA_2	0.43	0.57
	IT_1	0.43	0.57
	IT_2	0.43	0.56
	Obs	0.48	0.52
Elverum	MWP_1	0.39	0.61
	MWP_2	0.38	0.62
	LIA_1	0.39	0.61
	LIA_2	0.39	0.62
	IT_1	0.38	0.62
	IT_2	0.39	0.61
	Obs	0.44	0.56

5.3.2 Mean monthly discharge, temperature, precipitation and snow properties

The simulated mean monthly discharge for the three periods MWP, LIA and IT for both Solar 1 and 2 and both catchments are shown in Figure 5.6. Plots of mean monthly temperature, precipitation, SWE and SCA is presented in Figure 5.7 - Figure 5.10. The simulated discharge has similar seasonality as the observed discharge, both for Lalm and Elverum. Although, the increased discharge during August is delayed until October, for the simulations compared to the observations at Elverum. The peak discharge in May is accurately estimated for Elverum. However, the peak in June is overestimated by around 60 m^3/s. There are only minor differences between the simulation periods, and it is MWP (Solar 2) that deviates the most from the reference period (IT with Solar 1) at both catchments, but the difference is only noticeable between January and May.

Both Lalm and Elverum has a simulated temperature that is slightly lower than the observations for all periods for both Solar 1 and Solar 2. This difference is most noticeable during winter, although the maximum temperature is also somewhat underestimated. However, the simulated seasonality is very much the same as for the observations, with low temperatures around $-10°C$ in January and around $10°C$ in July. There is only minor differences in temperature between the simulations periods, and it is MWP and LIA with Solar 2 that has the biggest differences compared to the reference.

Simulated precipitation shows longer deviations in seasonality compared to observations. At Lalm, the simulated precipitation is quite low during winter, then it is higher than the observations during spring. During summer the simulations and observations are close to identical. However, during autumn

there is a decrease in precipitation for observations while there simultaneously is a peak in the simulated discharge. Elverum also has a noticeable difference in seasonality. The observed peak precipitation occurs in August, while the simulated peak precipitation occurs in October. The observed peak is also around 10 mm/month higher than for the simulations. Furthermore, the difference between the simulation periods are also quite small for precipitation. Although MWP (Solar 1) and LIA (Solar 2) has clearly lower precipitation during March-April for both catchments, compared to the reference period.

The SWE is very accurately simulated at Elverum, when compared to the observations, both in seasonality and magnitude. The seasonality is also well simulated at Lalm, however for this catchment the magnitude is much higher for the observed time than for the simulations. Between the simulations there is very little to no difference from July to September. The differences are biggest between January and June, for both catchments.

SCA for the simulations are quite comparable to the observed period, especially for Elverum. At Lalm, SCA does reach zero during summer, while this is not the case for the observations. The differences between the periods are biggest in June and during autumn at Lalm and in May and autumn at Elverum.

Tables with seasonal mean discharge, temperature and precipitation for Lalm and Elverum is included in Appendix A.

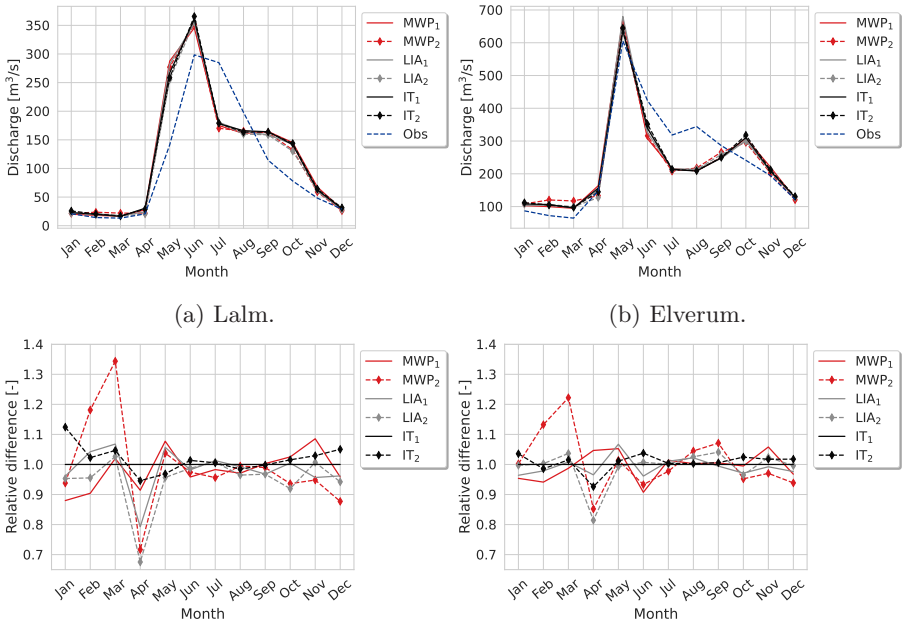

(a) Lalm.

(b) Elverum.

(c) Lalm difference.

(d) Elverum difference.

Figure 5.6: Mean monthly discharge for (a) Lalm and (b) Elverum, with corresponding mean monthly discharge difference for (c) Lalm and (d) Elverum. The most recent period (IT with Solar 1) is used for reference.

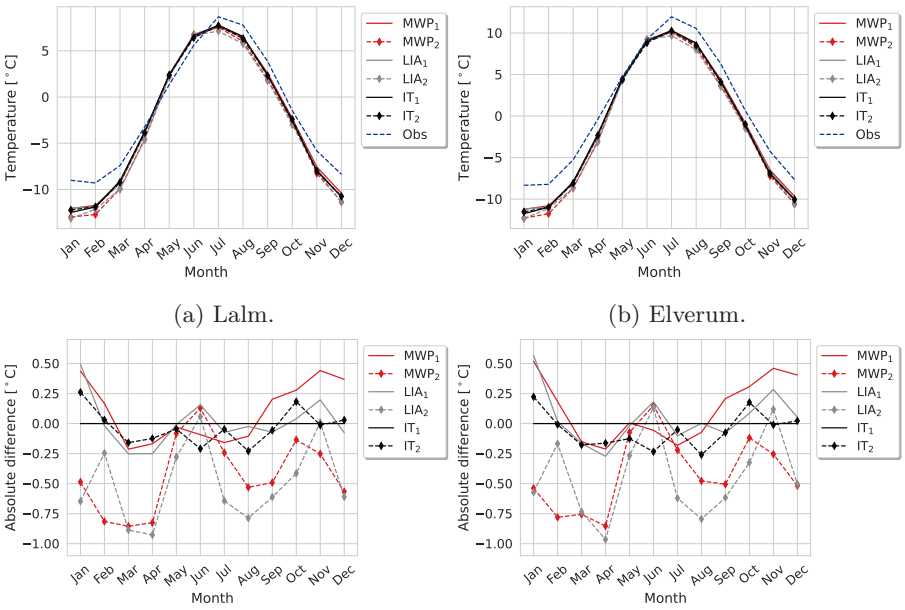

(a) Lalm. (b) Elverum.

(c) Lalm difference. (d) Elverum difference.

Figure 5.7: Mean monthly temperature for (a) Lalm and (b) Elverum, with corresponding mean monthly temperature difference for (c) Lalm and (d) Elverum. The most recent period (IT with Solar 1) is used for reference.

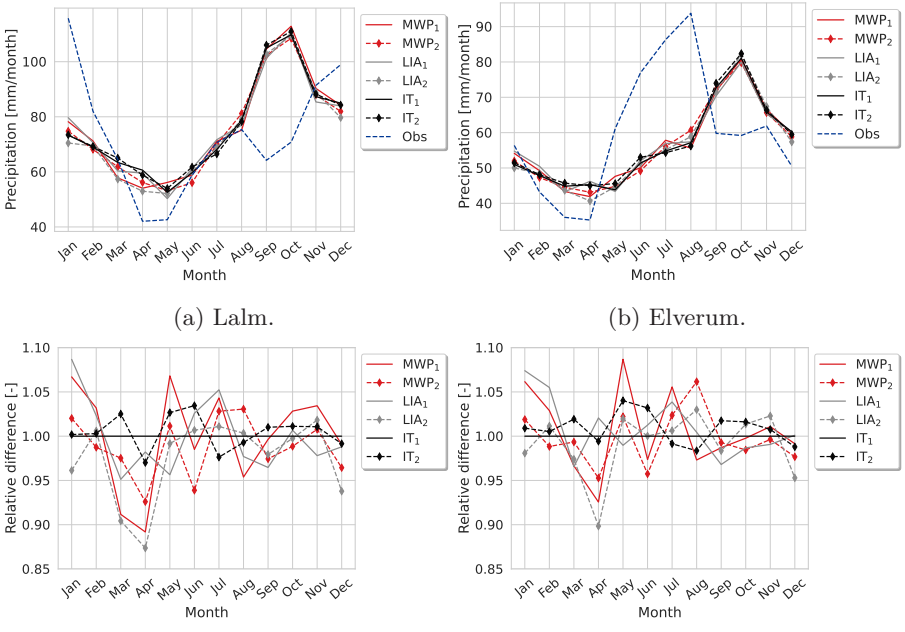

(a) Lalm. (b) Elverum.

(c) Lalm difference. (d) Elverum difference.

Figure 5.8: Mean monthly precipitation for (a) Lalm and (b) Elverum, with corresponding mean monthly precipitation difference for (c) Lalm and (d) Elverum. The most recent period (IT with Solar 1) is used for reference.

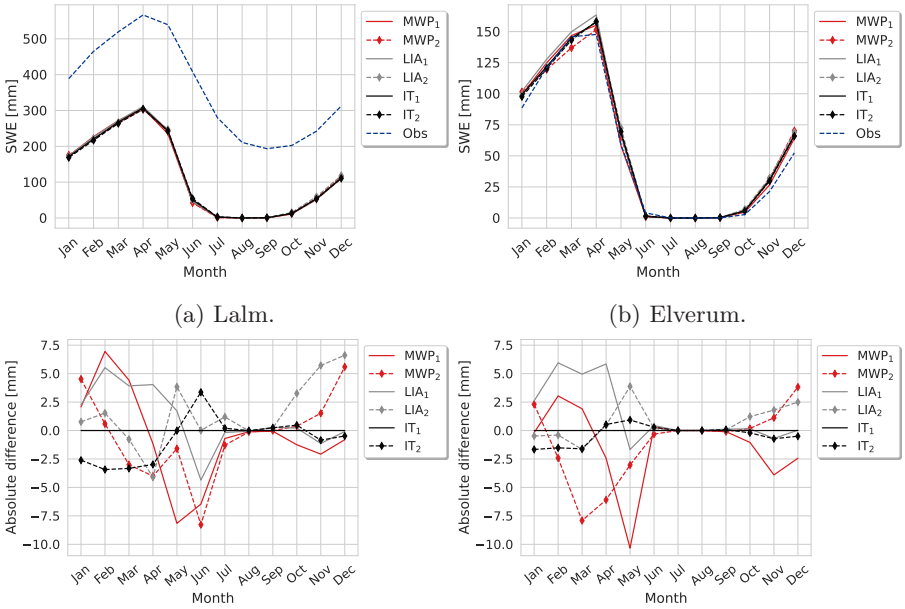

(a) Lalm. (b) Elverum.

(c) Lalm difference. (d) Elverum difference.

Figure 5.9: Mean monthly SWE for (a) Lalm and (b) Elverum, with corresponding mean monthly SWE difference for (c) Lalm and (d) Elverum. The most recent period (IT with Solar 1) is used for reference.

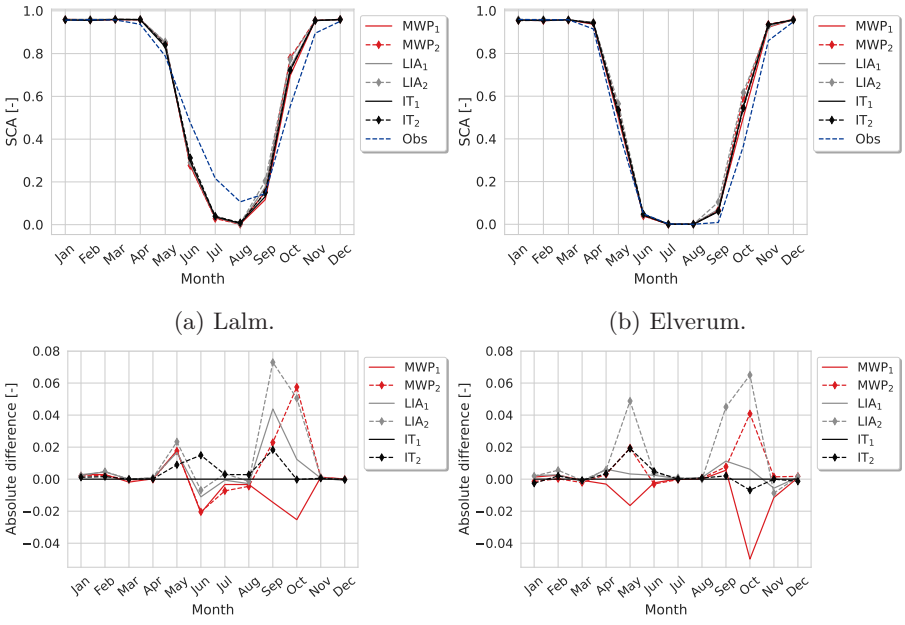

(a) Lalm. (b) Elverum.

(c) Lalm difference. (d) Elverum difference.

Figure 5.10: Mean monthly SCA for (a) Lalm and (b) Elverum, with corresponding mean monthly SCA difference for (c) Lalm and (d) Elverum. The most recent period (IT with Solar 1) is used for reference.

Flood roses of the observed annual maximum floods for Lalm (1971-2022) and Elverum (1969-2022) are shown in Figure 5.11. Evidently, Lalm has a broader time interval of the flooding season, since it experiences floods from the beginning of May to the end of July. On the other hand, Elverum also has a flooding season the starts in May, however it does not last longer than until the end of June. The flood seasonality is also a bit different as Elverum has the highest flood peak in the beginning of June, while Lalm has the highest flood peak towards the end of June. At Elverum most of the maximum floods occurs in May, while the floods are occurring during the entire summer season at Lalm. Furthermore, the maximum flood at Elverum (around 3000 m^3/s) has about three times the discharge than that at Lalm (around 1000 m^3/s).

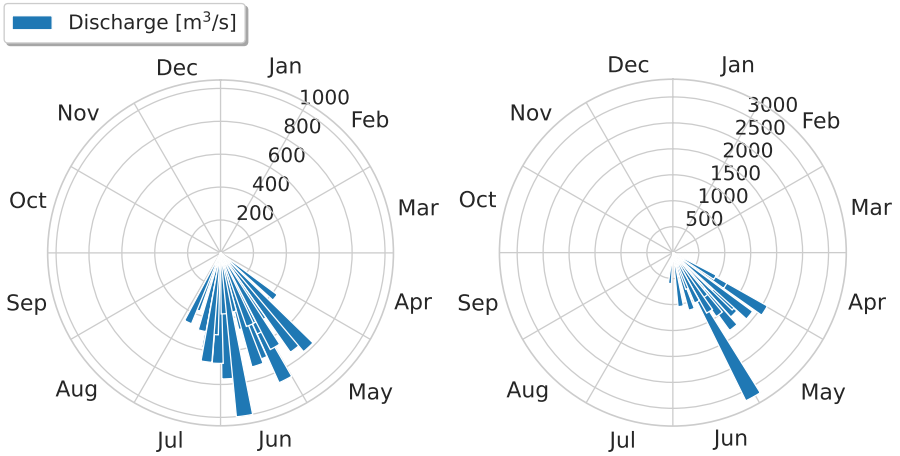

(a) Lalm. (b) Elverum.

Figure 5.11: Flood roses of annual maximum floods at (a) Lalm and (b) Elverum.

Figure 5.12 and Figure 5.13 show the flood roses of the simulated annual maximum floods for Lalm and Elverum, respectively. The seasonality of floods are similar to the observations for both catchments, as Lalm experiences floods from around the beginning of May and until the end of July, and at Elverum most of the floods occurs during the month of May. Although, there are some floods that occur during April as well, for the simulations. In fact, Elverum has two floods between February and March for MWP with Solar 2. The timing of the maximum flood varies slightly at Lalm. During MWP, the maximum floods occur in June for both Solar 1 and 2, as well as for LIA (Solar 2). In contrast, for IT and LIA (Solar 1), the maximum floods occur during the end of May. At Elverum, all the maximum floods occur in May. For MWP and LIA (Solar 2), the maximum floods take place in the middle of June and for IT and LIA (Solar 1), they take place at the end of May. The biggest difference between the observations and the simulations are the flood magnitudes. At Lalm, the simulated maximum floods lies around the 1500-2500 m^3/s interval, which is considerably higher than for the observations. Similarly, the simulated maximum floods at Elverum lies around the 4000-5000 m^3/s interval, which also is comfortably higher than for the observations. In both catchments the simulated maximum flood happened during LIA with Solar 1.

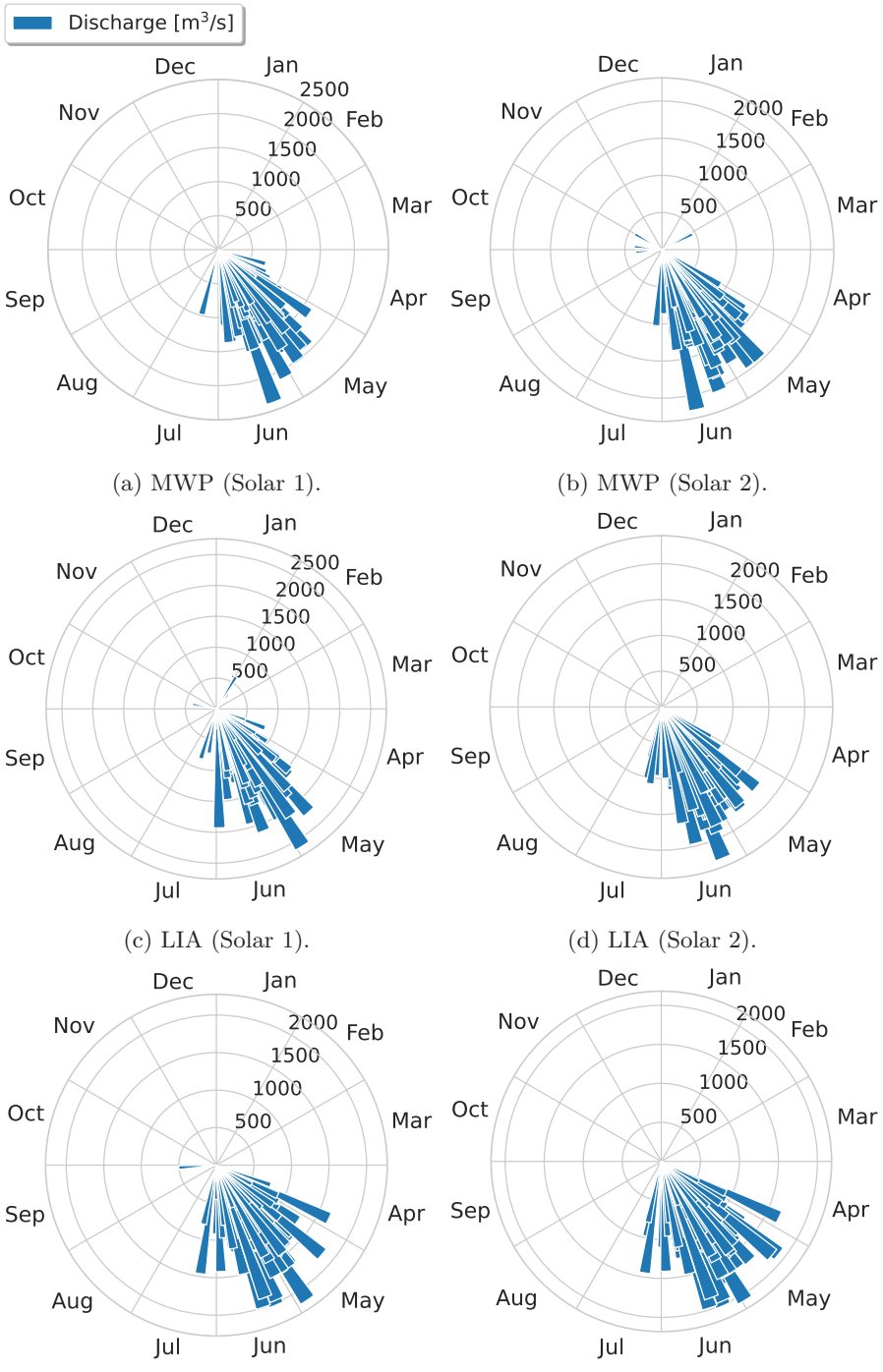

(a) MWP (Solar 1).

(b) MWP (Solar 2).

(c) LIA (Solar 1).

(d) LIA (Solar 2).

(e) IT (Solar 1).

(f) IT (Solar 2).

Figure 5.12: Flood roses of simulated annual maximum floods during (a)-(b) MWP, (c)-(d) LIA and (e)-(f) IT at Lalm.

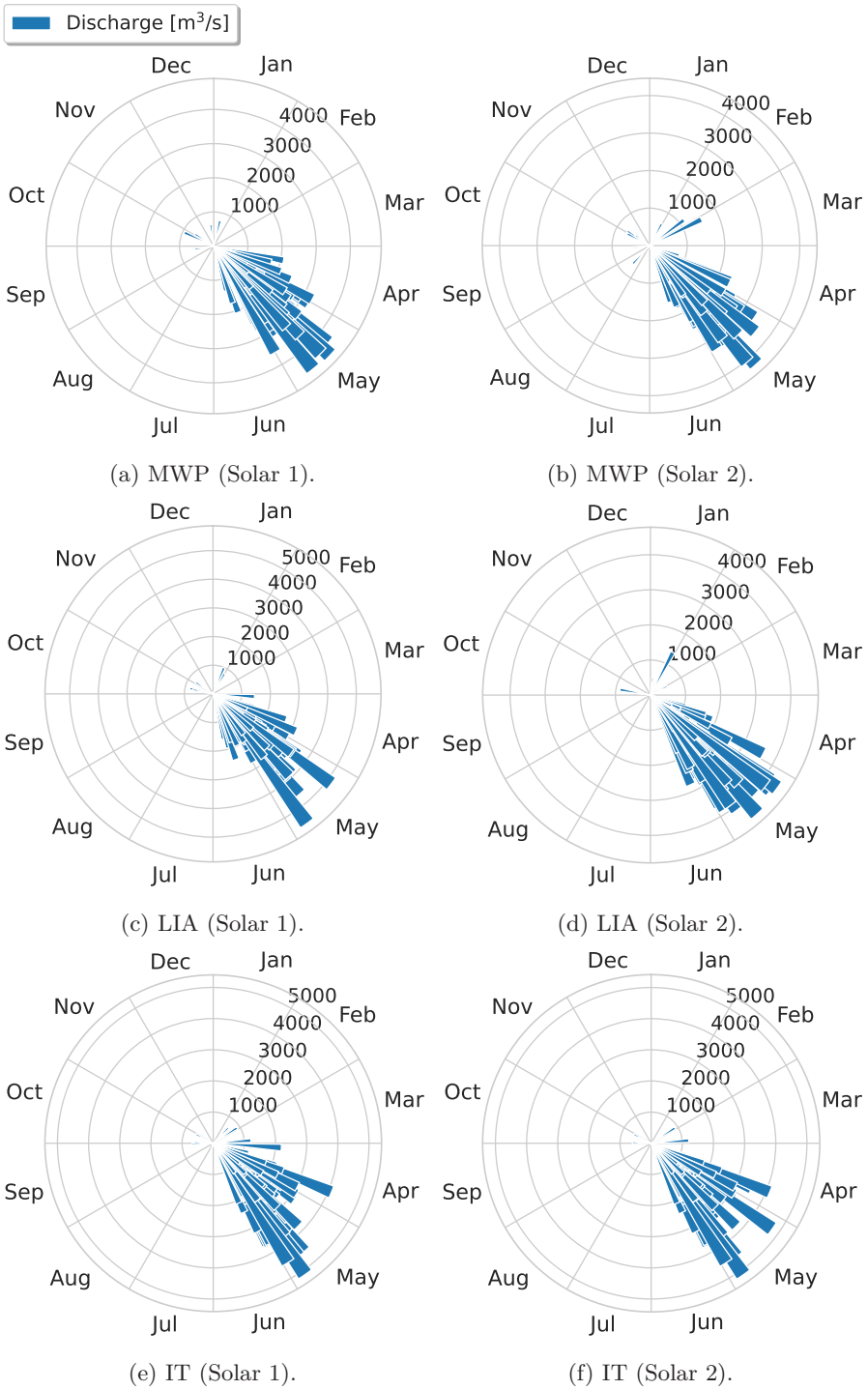

(a) MWP (Solar 1).

(b) MWP (Solar 2).

(c) LIA (Solar 1).

(d) LIA (Solar 2).

(e) IT (Solar 1).

(f) IT (Solar 2).

Figure 5.13: Flood roses of simulated annual maximum floods during (a)-(b) MWP, (c)-(d) LIA and (e)-(f) IT at Elverum.

5.4 Flood frequency analysis of paleo simulations

The simulated mean floods are displayed in Table 5.10. The highest mean floods occur during LIA, with the exception of IT at Elverum with Solar 2. MWP and LIA has very similar mean floods for Solar 1 and 2 at Lalm. The difference between Solar 1 and Solar 2 is biggest during IT, but the difference is only 15 m^3/s, which is smaller than the standard error. However, the opposite is true for Elverum, as IT is the period with the smallest difference between the Solar 1 and 2. The highest mean flood takes place in LIA (Solar 1) and the lowest in MWP (Solar 2) at both catchments.

Table 5.10: Mean floods [m^3/s]. Lalm and Elverum are denoted L and E. S1 and S2 refers to Solar 1 and 2, respectively.

	S	**MWP**	**LIA**	**IT**	**Obs**
L	1	1107.5 ± 30.3	1137.8 ± 33.5	1130.5 ± 30.5	590.9 ± 31.0
	2	1104.2 ± 30.9	1130.8 ± 30.7	1114.3 ± 32.3	590.9 ± 31.0
E	1	1962.8 ± 79.7	2086.2 ± 86.0	2054.0 ± 83.6	1323.7 ± 92.5
	2	1872.3 ± 70.6	1982.9 ± 86.7	2018.9 ± 83.1	1323.7 ± 92.5

Table 5.11 shows the simulated 100-year floods. The highest 100-year flood occurs during LIA, with the exception of IT at Lalm with Solar 2. Similarly to the mean floods, the highest 100-year flood at Lalm occurs during LIA (Solar 1). However, at Elverum the highest 100-year flood occurs during LIA (Solar 2). Furthermore, the smallest 100-year flood happens during MWP (Solar 1) at Lalm and during MWP (Solar 2) at Elverum. The biggest difference between Solar 1 and 2 occurs during IT (148.4 m^3/s) at Lalm. Despite this, the smallest difference (98.9 m^3/s) takes place during IT at Elverum. There is a small difference between the Solar 1 and 2 during LIA (76.7 m^3/s) at Lalm. At Elverum, Solar 1 and 2 differ by 1095.3 m^3/s during MWP. Corresponding 95% confidence intervals to the 100-year floods are included in Appendix A.

Table 5.11: 100-year floods [m^3/s].

Station	**Variability**	**MWP**	**LIA**	**IT**	**Obs**
Lalm	Solar 1	2082.1	2345.2	2165.6	1090.2
	Solar 2	2202.2	2268.5	2314.0	1090.2
Elverum	Solar 1	5232.2	5753.2	5373.4	2830.5
	Solar 2	4136.9	6244.6	5274.5	2830.5

The number of simulated annual maximum floods exceeding the observed 100-year flood is displayed in Table 5.12. The most exceedances occur during LIA for Solar 1 and during IT for Solar 2, at both catchments. LIA contains the biggest difference in the number of annual exceedances between the Solar 1 and 2 at both catchments, while IT has the smallest difference. At Lalm, the period with the highest number of exceedances (34) is LIA (Solar 1) and MWP (Solar 1) has the lowest (23). Similarly, Elverum also has the highest number of exceedances (39) during LIA (Solar 1), but the lowest (31) during MWP (Solar 1).

Table 5.12: Number of annual maximum floods exceeding the 100-year flood, obtained by the observed discharge.

Station	Variability	MWP	LIA	IT
Lalm	Solar 1	23	34	31
	Solar 2	27	27	30
Elverum	Solar 1	34	39	35
	Solar 2	31	32	33

Table 5.13 shows the number of annual maximum floods exceeding the Storofsen peak discharge. The most exceedances occur during LIA at both Lalm and Elverum, with the exception of IT with Solar 1. There is no difference between the Solar 1 and 2 at Lalm during MWP. However, IT (Solar 2) has seven more floods compared to Solar 1. At Elverum, there is no difference between Solar 1 and 2 during IT, however, they differ by five for both MWP and LIA. Elverum has most exceedances (13) during LIA (Solar 2) and fewest (three) during MWP (Solar 2). In contrast, MWP (Solar 1 and 2) has fewest exceedances (12) for Lalm, while LIA (Solar 2) and IT (Solar 2) has the most (20). Lalm has more annual maximum floods exceeding the Storofsen peak discharge than Elverum, although Elverum had more annual maximum floods exceeding the observed 100-year flood.

Table 5.13: Number of annual maximum floods exceeding the peak discharge during Storofsen.

Station	Variability	MWP	LIA	IT
Lalm	Solar 1	12	19	13
	Solar 2	12	20	20
Elverum	Solar 1	8	8	9
	Solar 2	3	13	9

Simulated and observed flood quantiles are shown in Figure 5.14. Similarly, precipitation quantiles are shown in Figure 5.15. It is clear that the simulated flood quantiles are substantially larger than compared to the observations for both catchments. On the other hand, the opposite is the case for precipitation, where the simulated precipitation quantiles are smaller than for the observations. MWP has the smallest flood quantiles at both catchments, while LIA has the largest. The only exception is at Lalm (Solar 2) where IT has slightly larger flood quantiles than LIA. At Elverum, there are rather small differences between the three periods for Solar 1 and quite large differences for Solar 2. The difference between the three periods are relatively small at Lalm, although the differences between the periods are bigger for Solar 1 than compared to Solar 2. In contrast, precipitation quantiles are not as consistent as the flood quantiles. LIA has the highest precipitation quantiles at both catchments, with the exception of Lalm with Solar 2. IT has the lowest precipitation quantiles for both catchments, except for Elverum with Solar 2. There is a large difference between the three periods at Elverum (Solar 2), and smaller differences for Solar 1. Additional figures showing how well the GEV distribution fit the observations for both the

flood and precipitation quantiles, along with the 95% confidence interval, is included in Appendix A.

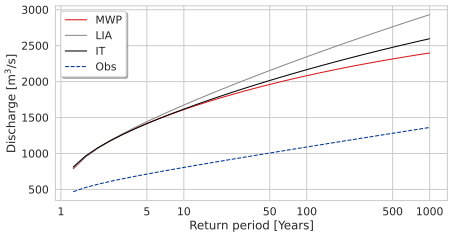

(a) Lalm (Solar 1).

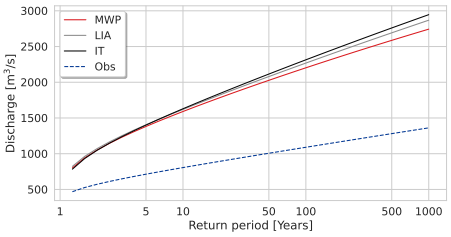

(b) Lalm (Solar 2).

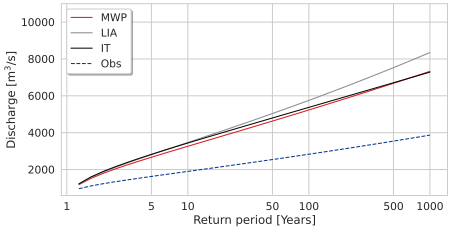

(c) Elverum (Solar 1).

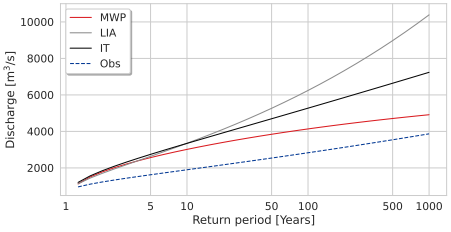

(d) Elverum (Solar 2).

Figure 5.14: Flood quantiles for (a)-(b) Lalm and (c)-(d) Elverum.

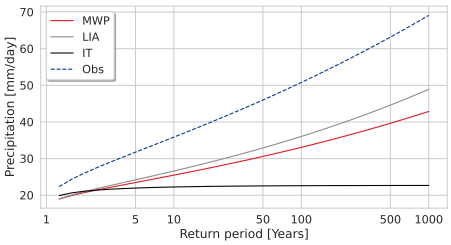

(a) Lalm (Solar 1).

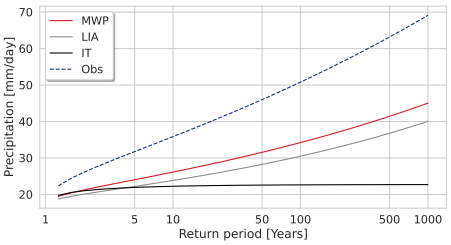

(b) Lalm (Solar 2).

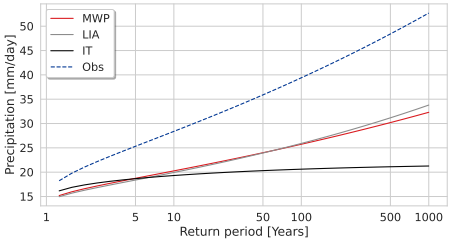

(c) Elverum (Solar 1).

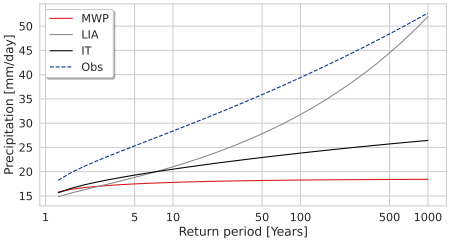

(d) Elverum (Solar 2).

Figure 5.15: Precipitation quantiles for (a)-(b) Lalm and (c)-(d) Elverum.

Figure 5.16 shows discharge, temperature, precipitation, SWE and snow melt at Lalm for two different years where a large flood occurred: 1050 for simulations of MWP (Solar 1) and 2020 for observations. The flood peak is more than twice as high for the simulations compared to observations. There is a spike in both simulated temperature and observed temperature at the time of the flood peak, however, the temperature spike for the simulations is higher and more sudden. In addition, there is a higher precipitation peak for simulations compared to observations at the time of the flood peak. SWE is highest for the observations, but the decrease in SWE during the flood peak is more prominent and sudden for the simulations. There is huge spike in snow melt at the time of the flood peak for the simulations, while the snow melt spike is small for the observations.

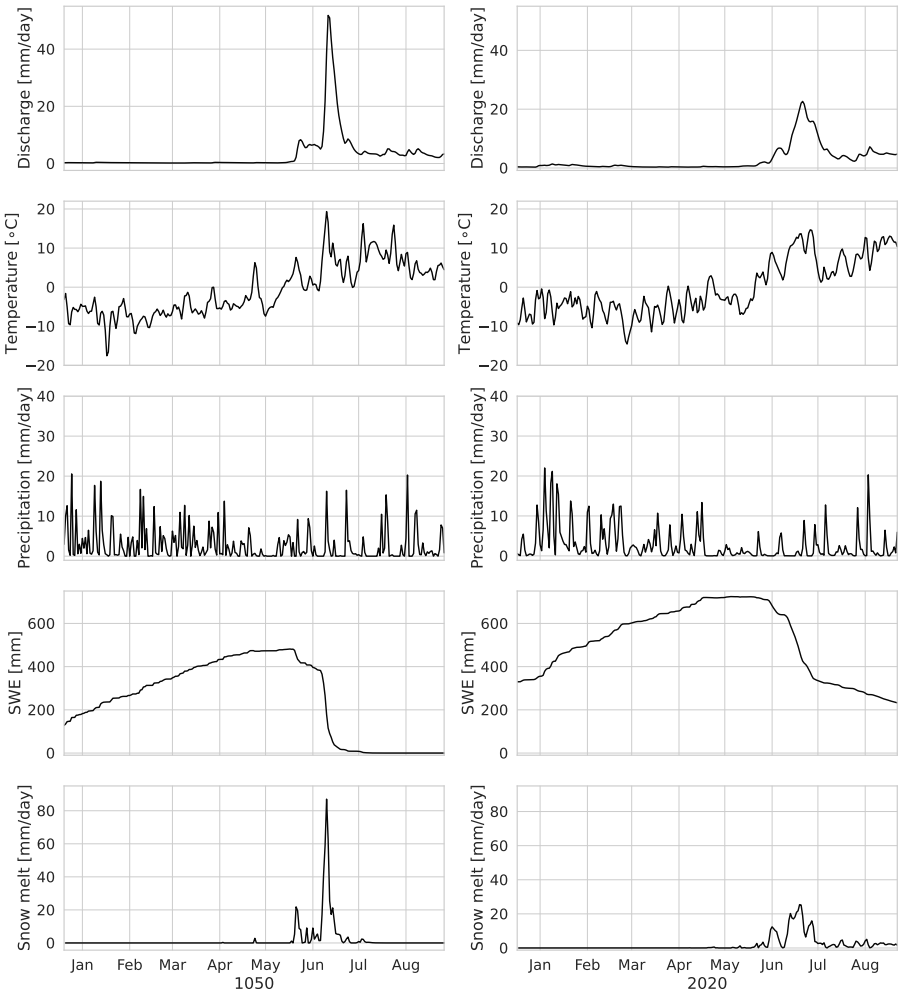

(a) MWP (Solar 1). (b) Observations.

Figure 5.16: Discharge, temperature, precipitation, SWE and snow melt in the period January-August during the years (a) 1050 and (b) 2020, in which a large flood occurred at Lalm.

Figure 5.17 shows discharge, temperature, precipitation, SWE and snow melt at Elverum for two different years where a large flood occurred: 1747 for simulations of LIA (Solar 2) and 1995 for observations. The flood peak is almost twice as high for the simulations compared to observations. There is a spike in both simulated temperature and observed temperature at the time of the flood peak, however, the temperature spike for the simulations is slightly higher and much more sudden. At the time of the flood peak, there is a higher precipitation peak for observations compared to simulations. SWE is slightly higher for the simulations, which also has a more prominent and sudden decrease in SWE during the flood peak compared to observations. There is huge spike in snow melt at the time of the flood peak for the simulations. In contrast, the spike in the observed snow melt is small during the flood peak.

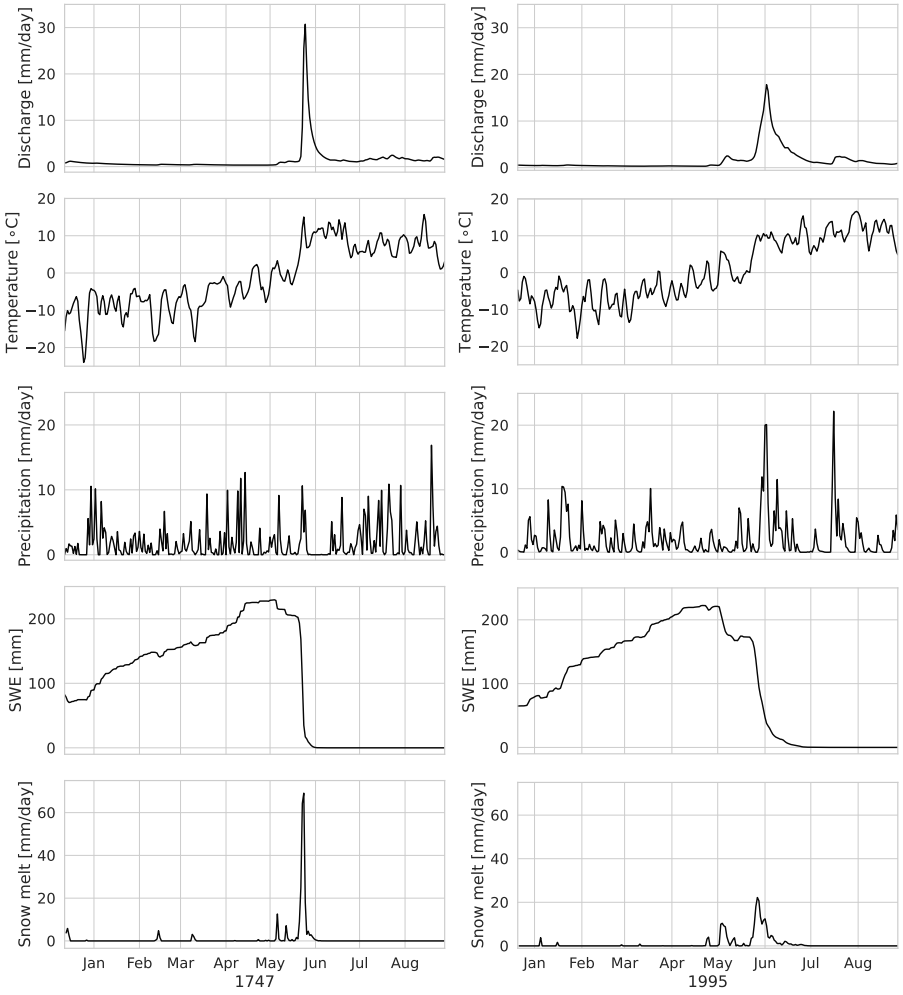

(a) LIA S2. (b) Observations.

Figure 5.17: Discharge, temperature, precipitation, SWE and snow melt in the period January-August during the years (a) 1747 and (b) 1995, in which a large flood occurred at Elverum.

5.5 Precipitation analysis of Storofsen

5.5.1 Basic approach

The result of the simple precipitation estimate required to reach the flood magnitude of Storofsen is shown in Table 5.14. Lalm, which has a catchment area of 3977.8 km^2, needs precipitation of 35.8 mm/day to reach a flood peak of 1648 m^3/s. Similarly, Elverum has a larger catchment area (15449.9 km^2), which requires 21.8 mm/day precipitation to reach a flood peak of 3900 m^3/s.

Table 5.14: Precipitation estimates of Storofsen.

Station	**Peak flood [m^3/s]**	**Prec [mm/hr]**	**Prec [mm/day]**
Lalm	1 648	1.4	35.8
Elverum	3 900	0.9	21.8

5.5.2 Simulation approach

The results of the more advanced precipitation simulation approach is shown in Table 5.15. These mean precipitation inputs resulted in the discharge simulations seen in Figure 5.18. At Lalm, with wet initial conditions (soil), a mean precipitation of 612.4 mm/day on the day of peak precipitation (22nd of July) were enough to result in a maximum discharge of 1648 m^3/s. For similar wet conditions at Elverum, a mean precipitation of 93.7 mm/day on the 22nd of July was sufficient to cause a maximum discharge of 3900 m^3/s. In contrast, for the dry conditions, it was not possible to simulate a flood comparable to Storofsen. Despite the high precipitation of 1558.3 and 382.3 mm/day at Lalm and Elverum, respectively, the corresponding discharge was only 98 and 83 m^3/s. For the normal conditions, the Storofsen peak discharge was simulated with 2478.4 and 2491.4 mm/day mean precipitation on the 22nd of July.

Table 5.15: Mean precipitation causing peak flood magnitude of Storofsen. SPI is dimensionless.

		Precipitation [mm/day] July 1789			
Catchment	**SPI**	**20th**	**21st**	**22nd**	**23rd**
Lalm	3.0	159.5	337.6	612.4	113.2
	-3.3	402.3	791.4	1558.3	280.0
	0.1	633.4	1270.9	2478.4	479.3
Elverum	3.0	23.7	50.4	93.7	17.0
	-2.7	99.7	193.2	382.3	71.4
	0.1	614.4	1286.0	2491.4	477.6

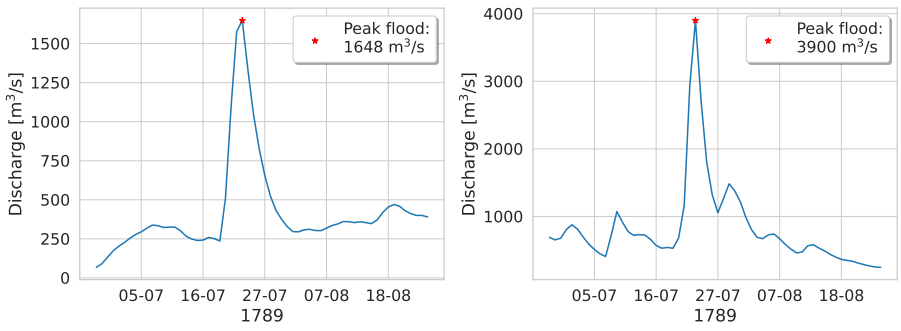

(a) Lalm (wet, SPI: 3.0).

(b) Elverum (wet, SPI: 3.0).

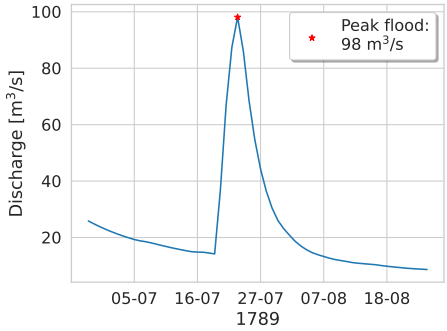

(c) Lalm (dry, SPI: -3.3).

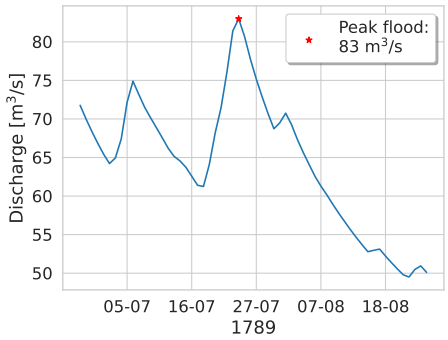

(d) Elverum (dry, SPI: -2.7).

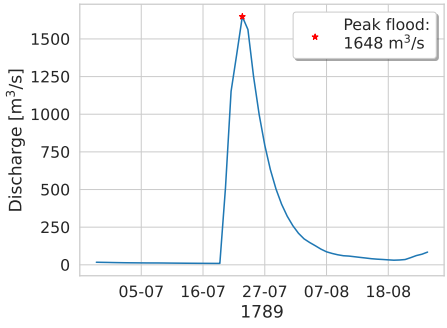

(e) Lalm (normal, SPI: 0.1).

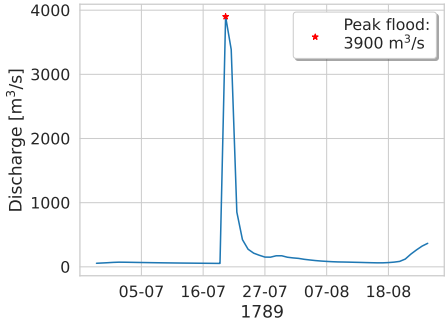

(f) Elverum (normal, SPI: 0.1).

Figure 5.18: Simulations of Storofsen at Lalm and Elverum based on the four-day precipitation event during 20th-23rd of July 1789, similar to descriptions from the literature. Initial (soil) conditions are (a)-(b) wet, (c)-(d) dry and (e)-(f) normal. The red star denotes the peak flood, which occurred during the 22nd of July 1789.

CHAPTER 6

Discussion

This chapter presents the discussion of the bias correction and the quality of the Shyft model. Secondly, the seasonality and flood characteristics during MWP, LIA and IT are discussed. Furthermore, the chapter includes a comparison of Storofsen to the flood characteristics during MWP, LIA and IT. Lastly, the impact of solar variability and the Storofsen precipitation analysis are discussed.

6.1 Bias correction of climate model data

All Shyft model forcings were bias corrected, in order to adjust the modeling bias that exists in climate models. The bias correction was performed based on the current climatology, i.e. the observation-based variables: temperature, precipitation, wind speed, relative humidity and radiation. Table 5.1 shows the goodness of fit measures of the bias correction and it is evident that the difference between the paleo simulated and the observation-based forcings is minimised after correction. Additionally, the difference in mean and standard deviation is small between the paleo simulations and observation-based forcings, as seen in Table 5.2 and Table 5.3, respectively. However, the observed precipitation seasonality, as seen in Figure 5.8, is not found for the paleo simulations. For Lalm, the seasonality of the simulations is similar to the observations from January to August, but between August and November, there is a positive peak in simulated precipitation and a negative peak in observed precipitation. At Elverum, the maximum observed precipitation occurs in July, whereas the maximum simulated precipitation occurs in October. Thus it is an obvious shift in the simulated precipitation seasonality compared to the observed seasonality. One challenge with the bias correction used in this study, is that it is not dependant on season. This means that the bias correction approach is unable to assign the seasonality of the observed data to the paleo simulations. As a result, the bias corrected paleo simulations will have a seasonality stemming from the NorESM1-F model, which is the most probable cause of the discrepancy in seasonality between the observed and paleo simulated precipitation. Another possible explanation for this difference in seasonality between observed and corrected simulated precipitation, is the fact that precipitation was bias corrected using only the gamma distribution, since the left tail of the sample can have influence on the right tail (Van Montfort and Witter, 1986). Even though precipitation usually follows the gamma distribution, the tails are known to fit the Generalised Pareto (GP) distribution. The bias correction, could also

have been improved by including a separate distribution for extremes. The GEV and Gumbel distributions have been broadly used for handling extreme precipitation events (Heo et al., 2019). However, adding more distribution to the bias correction approach was deemed too time consuming considering the huge data file size utilised for this study.

The QDM bias correction was performed for 30-year moving time windows. This means that the CDFs would vary between the three periods MWP, LIA and IT, which lasted 150 years each. As a result, the bias correction would conserve the differences between the periods. On the other hand, if the bias correction had been performed with one single CDF for all periods, then differences between the periods could be reduced. During detrending by quantile and QM, the statistical properties of the historical observations will be imposed on the simulated data to be bias corrected (Cannon et al., 2015). However, when the absolute/relative change in quantiles $[\phi(t)]$ is added/multiplied to the QM bias corrected data, the projected climate signal (trend) is reintroduced to the simulated data (Cannon et al., 2015). This suggests that the small differences in the mean monthly values (Figure 5.6-Figure 5.10) between MWP, LIA and IT are not caused by the bias correction. Thus the small differences between the periods stem from the NorESM1-F model.

6.2 Calibration and validation of the hydrological model

The Shyft model was found to be robust and the efficiency coefficients were high for all calibration runs (see Table 5.5). After the 2-fold cross validation at Lalm, the lowest validation NSE was 0.74, which is considered to be very good (Yilmaz and Onoz, 2020). At Elverum, the lowest validation NSE was 0.65, which is still considered to be good (Yilmaz and Onoz, 2020). For calibration on the entire observed discharge time series, the efficiency coefficients were NSE = 0.83 and NSE = 0.81 at Lalm and Elverum, respectively. These are both excellent model efficiencies. Interestingly, Elverum has a higher validation efficiency for 1969-1995 than for the corresponding calibration period 1995-2020. This is unusual, although it is possible (Knoche et al., 2014). The reason for this high validation efficiency was thought to be the large flood event of "Vesleofsen" in June, 1995. However, this was found to not be the case after increasing the validation period to include the 1995 flood, although this increased both the calibration and validation efficiency. Still, the validation efficiency was larger than the calibration efficiency. An important note about both catchments, and Elverum in particular, is that they are both subject to regulations. Lalm has been regulated since 1956, while Elverum has been regulated since 1917. The percentage of regulation is 12.2% at Lalm and 10.0% at Elverum. These regulations can influence the discharge as water is artificially stored and released. This can lead to decreased discharge during autumn and increased discharge during winter, were water is released in order to produce electricity for heating. Although, the regulations did not seem to reduce the model efficiency much, since the efficiencies were mostly very good. Additionally, reservoirs also has a similar impact on discharge as lakes does, they slow the flowing water down and can thus decrease small flooding events. Although, reservoirs do not reduce the absolute largest floods. On the other side, reservoirs can lead to increased flooding events, e.g. by dam failure. While

model efficiencies are important to check how accurately a model is, it is also important to identify how well the model simulates peak discharge, especially when researching flood events. Figure 5.5 contains plots that show how well maximum discharge and annual floods are simulated by the model. It is evident, that there is a slight underestimation of discharge peaks at Lalm, and there is a minor underestimation of peak floods at Elverum. Despite this, the 1995 flood is simulated spot on.

6.3 Seasonality of paleo simulations

6.3.1 Monthly seasonality

Differences in the monthly seasonality of discharge, temperature and precipitation for the three periods MWP, LIA and IT are very small and there does not seem to be a distinct difference between them. The explanation for this could potentially be found in the way the data was bias corrected. As previously mentioned, the paleo simulations were adjusted based on the current climatology, i.e. the climate from 1957 to 2020. However, the climate signals (trends) of the paleo simulations were reintroduced to the data during the bias correction, which suggests that the correction should not have reduced the differences between the three periods. This is supported by the figures showing time series of temperature (Figure A.3) and precipitation (Figure A.4) before and after bias correction, which show that there are no clear differences in neither temperature nor precipitation trends after correction compared to before (see Appendix A). As a result, the findings of this study suggests that the three periods MWP, LIA and IT have similar monthly seasonality of the variables: discharge, temperature and precipitation.

There is a very large difference between the observed and simulated SWE at Lalm, as seen in Figure 5.9. This could be explained by the high amount of precipitation occurring during January and February (Figure 5.8). Simultaneously, there are temperatures well below 0°C, as seen in Figure 5.7. Moreover, Lalm is a high altitude catchment which mostly consists of bare rock (70.3%). As a result of this, the large snow accumulation during winter may have prevented the snow from melting out during summer, as it did for the simulations. Additionally, Lalm catchment has some glaciers (5.4%). In these glaciated areas snow is stored through the summer season, which could also explain why the observed SWE does not melt out during summer. It is possible that accurately simulating glaciers is challenging in Shyft, which could be an explanation for why all the simulated snow melts out during summer in a catchment subject to glaciers. This is supported by Figure 5.10, which show that 0% of Lalm catchment area is covered by snow in August. In other words, the glaciers melted away in August for the simulations.

6.3.2 Flood timing during MWP, LIA and IT

The flood roses (Figure 5.12 and Figure 5.13) show that the seasonality is consistent between all the three periods MWP, LIA and IT, where the annual maximum floods occur in May/June for Lalm and in May for Elverum. Additionally, the flood roses also show that there were no large annual maximum

floods occurring in late July for any of the three periods MWP, LIA and IT. This confirms that Storofsen was an exceptional flood event. In eastern Norway, floods most often occur in spring or early summer, and are caused by snow melt or a combination of snow melt and rainfall (Gottschalk et al., 1979). Floods can also occur during autumn, in which the floods are mostly driven by rainfall. To put this in context of Storofsen, it means that the timing of Storofsen was to late to be a usual snow melt-driven flood and to early to be a usual rainfall-driven flood. This means that an extraordinary weather event, i.e. the Vb cyclone track (Bebber, 1891), is required in order to yield a large flood event in late July (Roald, 2013). Although, no evidence for such a weather event was found during any of the three periods MWP, LIA and IT.

However, a normal Vb cyclone track is not sufficient to cause a flood of the size of Storofsen. In order to create a flood of a magnitude comparable to Storofsen, there would have to be an extreme Vb event caused by high temperatures and very humid air (Roald, 2013; Østmoe, 1985). Moreover, snow melt was a considerable driver of Storofsen (Roald, 2013), this would have required large amounts of snow stored in the mountains until the end of July. Figure 5.9 and Figure 5.10 show that all the snow had melted out by the beginning of July for Elverum, while Lalm still had around 5% of the catchment area covered by snow for the simulations. Additionally, mean monthly precipitation peaks during autumn for the simulations and there is no evidence for particularly wet summers. Another important factor was the wet soil conditions prior to Storofsen, which were caused by thawing of the deep frost in the soil, due to an extremely cold winter and cold weather that lasted until April (Sommerfeldt, 1972). Figure 5.7 shows that mean monthly air temperature is below 0°C until the middle of April at both Lalm and Elverum for the simulations. This suggests that deep frost in the ground could have occurred during MWP, LIA and IT. Although, it is important to note that these figures show the mean monthly values, and there could have been years were the variables deviated from the monthly mean values.

6.4 Flood magnitude analysis of paleo simulations

Floods were found to be slightly higher (Table 5.10 and Table 5.11) and more frequent (Table 5.12 and Table 5.13) overall during LIA, than compared to MWP and IT. LIA is the period, in which Storofsen occurred. Multiple studies have found an increased flood frequency during LIA (Grove, 1972; Huo et al., 2022). Increased flood magnitude and frequency in LIA could be due to larger amounts of snow and glaciers storing water available for melting, while the summer temperatures were still positive and could produce floods by melting. This is the situation described in Brázdil et al. (2010), where high rates of snow accumulation and frozen soils combined with sudden warming and rainfall caused numerous floods across Europe in 1783/84. However, LIA could also be subject to larger floods due to lower temperatures, which reduce evaporation and thus increase soil moisture, causing larger floods (Blöschl et al., 2020). There was also periods of increased precipitation during LIA (Hanssen-Bauer et al., 2009), however, this was winter precipitation (most likely snow), which could not have directly resulted in large flood events, however it could contribute to increased spring floods.

It is clear that the simulated flood peaks are unrealistically high, since the 100-year floods (Table 5.11) are higher than the peak discharge during Storofsen (Table 5.14), which is the largest known historical flood in Norway. In addition, there were 23-39 simulated floods that exceeded the observed 100-year (Table 5.12) for each period MWP, LIA and IT, which all lasted 150 years. The expected number of exceedances of a 100-year flood within a 150 year time period would be 1-2. There was also up to 20 floods that exceeded the Storofsen peak discharge in each period, as seen in Table 5.13. The flood quantiles are also much higher for the simulations compared to observations (Figure 5.14). Precipitation is the most influential forcing variable on discharge, and could thus potentially be the cause of the unreasonable high simulated flood peaks. However, Figure 5.15 reveal that the simulated precipitation quantiles actually are lower than compared to the observations. Despite this, the simulated peak precipitation could have been lower than the observed, but that there were more wet days, which would result in wetter soil conditions and create a more sensitive flood response to smaller amounts of precipitation. As revealed in Table 5.9, there are actually fewer wet days for the simulations than compared to the observations at both catchments. Furthermore, Lalm has slightly higher mean precipitation for simulations as compared to observations, while Elverum has mean precipitation that is slightly lower. This means that Lalm could have soil conditions that are as wet as for the observations, although Elverum would have drier conditions, based on precipitation.

Figure 5.16 and Figure 5.17 might reveal the cause of the high flood peaks. It is evident that snow melt is the most important flood generating process. Snow melt was four times as high precipitation for Lalm and six times higher for Elverum at the time of the flood peak for simulations. For observations, snow melt and precipitation were of the same magnitude at the time of the flood peak for both catchments. Additionally, snow melt is three and four times as high for the simulations compared to the observations for Elverum and Lalm, respectively. The cause of this high snow melt could be explained by the spike in temperature at the time of the flood peak. For the simulations the temperature peak is higher and sharper, meaning that the peak occurred more suddenly compared to the observations. This sudden and higher peak in temperature, seems to have caused very rapid snow melt. SWE drops from around 400 and 200 mm at Lalm and Elverum, respectively, to about 0 mm in the span of a few days for the simulations. In contrast, this melting process takes considerably more time for the observations, especially at Lalm. These findings suggest that the unrealistically high flood peaks are caused by too high and sudden spikes in temperature. These temperature spikes can either stem from the NorESM1-F model or they could be imposed during the bias correction.

6.5 Effect of solar variability

The two solar variabilities, Solar 1 (low variability) and Solar 2 (high variability), have different TSI as seen in Figure 3.2. Since Solar 1 has a higher TSI overall as compared to Solar 2, there are noticeable differences in the mean temperatures (Table 5.7). This is evident for both Lalm and Elverum for all periods, with only one exception, during IT at Lalm where the mean temperature was -2.7°C for both Solar 1 and 2. However, the difference between the two solar variabilities

was the smallest during IT, and at Elverum the difference was only 0.1°C. Solar 2 was 0.5°C colder than Solar 1 during LIA, for both catchments, which was the biggest difference in mean temperature. Despite this considerable difference in mean temperature, mean discharge and precipitation have only minor differences. Similarly, the seasonality of temperature, precipitation discharge, SWE, SCA and annual maximum floods is close to the same. The reason for the small differences between Solar 1 and Solar 2 could be the similar fluctuation timing of TSI. TSI varies in a similar pattern for both Solar 1 and 2. Only the flood magnitude and frequency differs considerably between Solar 1 and 2, although the difference is inconsistent across the three periods and the two catchments. Generally, it would be expected that higher temperatures lead to higher floods, due to snow melt and more precipitation falling as rain, which would mean that Solar 1 should experience larger floods compared to Solar 2. However, this is not consistently the case, which suggests that the reinforcing effect of decreased evaporation on floods, due to lower temperatures (Blöschl et al., 2020) is comparable to the reinforcing effect of more snow melt and rainfall due to higher temperature.

It is clear that the mean temperature is lower during LIA than in MWP (Table 5.7), which is what would be expected. On the other hand, for Solar 1 at both catchments, the mean temperature is the same for LIA as for IT. This suggests that Solar 2 is the more accurate solar variability in regards to temperature than compared to Solar 1, since it is more realistic that the period after the industrial revolution would be warmer than the period referred to as a little ice age.

6.6 Storofsen precipitation analysis

In the literature (Østmoe, 1985; Roald, 2013), it is described that there was very wet soil conditions before the intense rainfall event that began on the 20th of July 1789 and ended four days later, which resulted in the Storofsen flood. In order to investigate what impact the soil conditions had on the flood, it was important to run simulations and comparing the different conditions. However, soil moisture is not a variable that is available as output in Shyft. As a result of this, the soil conditions were estimated by calculating SPI based on precipitation. Table 5.15 shows the impact of the soil conditions prior to the flood event. The result of the corresponding discharge simulation is seen in Figure 5.18. For the wet initial conditions (positive SPI) 612.4 and 93.7 mm/day mean precipitation on the day of peak precipitation (22nd of July) caused a peak discharge similar to the literature (Engeland et al., 2018; Engeland et al., 2020) for Lalm and Elverum, respectively. Those precipitation values are considered to be heavy showers (Lalm) and heavy rain (Elverum). For the dry conditions (negative SPI), the soil was too dry and it was not possible to simulate a flood of the magnitude of Storofsen. This means that most of the precipitation falling as rain infiltrated the soil and some was most likely lost due to evapotranspiration, preventing the generation of a flood. Despite increasing the mean peak precipitation to 1558.3 and 382.3 mm/day for Lalm and Elverum, respectively, the resulting discharge did not exceed 100 m^3/s for either catchment. Lastly, for normal initial conditions (SPI close to 0), the discharge peaks did not reach the values from the literature until the mean

precipitation was set to 2478.4 and 2491.4 mm/day at Lalm and Elverum, respectively. Those precipitation values are considered extreme, and is nowhere near realistic values for inland, eastern Norway. These findings suggest that Storofsen could only have occurred during a period with a very wet soil, if rainfall was the only flood driving mechanism. Furthermore, it appears that Elverum is more sensitive to precipitation when it comes to flood events, as it required much less precipitation in order to reach the Storofsen flood size. This could be due to the larger catchment area at Elverum as compared to Lalm, which would accumulate a higher discharge since the precipitation would be spread over a larger area. In other words, it would result in more water coming in for the same amount of precipitation. Even though precipitation was the main driver of Storofsen, snow melt did also contribute considerably (Roald, 2013). This could be a subject for future research by performing a snow melt analysis of Storofsen.

CHAPTER 7

Conclusion

The configured and calibrated Shyft model has been used in order to simulate discharge for the three periods MWP, LIA and IT, by utilising the QDM bias corrected paleo simulations as model forcings. Additionally, a precipitation analysis of Storofsen has been performed. The main aim of this study was to investigate the seasonality and magnitude of floods within the three historical periods MWP, LIA and IT, and comparing the results to the Storofsen flood. Another aim was to identify the hydrometeorological conditions capable of causing Storofsen. Analyses of the Shyft model simulated discharge, yield the answers to the research questions:

i) Did flood seasonality and magnitude differ between MWP, LIA and IT?

The simulations show that the seasonality is consistent for all three periods, where the annual maximum floods occur in May/June at Lalm and in May at Elverum. There are slightly higher and more frequent floods during LIA, than compared to MWP and IT.

ii) Did a flood occur at the same time of the season (late July) as Storofsen during the three periods MWP, LIA and IT?

None of the simulated floods occurred in late July, confirming that the Storofsen flood was exceptional.

iii) Did a flood of a comparable magnitude to Storofsen happen within the three periods MWP, LIA and IT?

Multiple of the simulated floods exceeded the Storofsen flood with up to 100% within each period. However, these simulated peaks are deemed to be unrealistic.

iv) What were the hydrometeorological conditions that caused Storofsen in late July 1789?

Peak mean precipitation required to cause a simulated flood with the magnitude of Storofsen was found to be 612.4 and 93.7 mm/day for Lalm and Elverum, respectively.

The results show that the flood seasonality is consistent between all the three periods MWP, LIA and IT, and none of the periods included any large floods at the timing of Storofsen in late July. There were multiple floods exceeding the Storofsen flood level within each of the three periods, although the flood peaks are unrealistically high. Sudden, high spikes in simulated temperature were suggested to be the cause of these high flood peaks, by creating rapid and high snow melt. The precipitation analysis suggests that wet soil conditions were required, in order for rain to produce a flood event comparable to Storofsen.

7.1 Further research

There are some results in this study that should be investigated further. Mainly, the explanation behind the unrealistically high simulated discharge peaks during the three periods MWP, LIA and IT. It was suggested that high and sudden spikes in temperature, resulted in rapid snow melt, which caused the unreasonably high flood peaks for the simulations. Investigating the effect of these temperature spikes could be subject to further research. If the temperature is the cause of the high flood peaks, it would be interesting to see whether the sudden spikes stem from the NorESM1-F model or if they are imposed during the bias correction.

There were some ideas of research that were thought to be performed, but turned out to be too time consuming or beyond the scope of this thesis. There was meant to be performed a snow melt and land cover analysis of Storofsen. It was also meant to be performed a bias correction of precipitation with the GP distribution on the tails, which most likely would have made the Shyft model simulations more realistic. Another idea was to use the paleo simulations to create synoptic weather charts for MWP, LIA and IT. These charts could have been compared to weather charts for the days leading up to and during Storofsen from (Østmoe, 1985).

Bibliography

Ahsanullah, M., Kibria, B. and Shakil, M. (2014). 'Normal distribution'. In: *Normal and Student st Distributions and Their Applications*. Springer, pp. 7–50. doi: https://doi.org/10.2991/978-94-6239-061-4_2.

Ailliot, P., Thompson, C. and Thomson, P. (2011). 'Mixed methods for fitting the GEV distribution'. In: *Water Resources Research* vol. 47, no. 5. doi: https://doi.org/10.1029/2010WR009417.

Alderman, K., Turner, L. R. and Tong, S. (2012). 'Floods and human health: a systematic review'. In: *Environment international* vol. 47, pp. 37–47. doi: https://doi.org/10.1016/j.envint.2012.06.003.

Allen, R. G., Trezza, R. and Tasumi, M. (2006). 'Analytical integrated functions for daily solar radiation on slopes'. In: *Agricultural and Forest Meteorology* vol. 139, no. 1-2, pp. 55–73. doi: https://doi.org/10.1016/j.agrformet.2006.05.012.

Alnes, K., Berg, A. O., Clapp, C., Lannoo, E. and Pillay, K. (2018). 'Flomrisiko i Norge: Hvem betaler for framtidens våtere klima?' In: *CICERO Report*.

Ault, T., Deser, C., Newman, M. and Emile-Geay, J. (2013). 'Characterizing decadal to centennial variability in the equatorial Pacific during the last millennium'. In: *Geophysical Research Letters* vol. 40, no. 13, pp. 3450–3456. doi: https://doi.org/10.1002/grl.50647.

Bebber, W. J. van (1891). *Die Zugstrassen der barometrischen Minima nach den Bahnenkarten der Deutschen Seewarte für den Zeitraum 1875–1890*. Meteorologische Zeitschrift, pp. 361–366.

Beguería, S., Vicente-Serrano, S. M. and Beguería, M. S. (2017). 'Package 'spei''. In: *Calculation of the Standardised Precipitation- Evapotranspiration Index, CRAN [Package]*.

Benestad, R. (2013). 'Association between trends in daily rainfall percentiles and the global mean temperature'. In: *Journal of Geophysical Research: Atmospheres* vol. 118, no. 19, pp. 10–802. doi: https://doi.org/10.1002/jgrd.50814.

Bergström, S. (1976). *Development and application of a conceptual runoff model for Scandinavian catchments*.

Bethke, I., Outten, S., Otterå, O. H., Hawkins, E., Wagner, S., Sigl, M. and Thorne, P. (2017). 'Potential volcanic impacts on future climate variability'. In: *Nature Climate Change* vol. 7, no. 11, pp. 799–805. doi: https://doi.org/10.1038/nclimate3394.

Beyer, R., Krapp, M. and Manica, A. (2020). 'An empirical evaluation of bias correction methods for palaeoclimate simulations'. In: *Climate of the Past* vol. 16, no. 4, pp. 1493–1508. doi: https://doi.org/10.5194/cp-16-1493-2020.

Bhattarai, B. C., Silantyeva, O., Teweldebrhan, A. T., Helset, S., Skavhaug, O. and Burkhart, J. F. (2020). 'Impact of catchment discretization and imputed radiation on model response: a case study from central himalayan catchment'. In: *Water* vol. 12, no. 9, p. 2339. doi: https://doi.org/10.3390/w12092339.

Blöschl, G., Kiss, A., Viglione, A., Barriendos, M., Böhm, O., Brázdil, R., Coeur, D., Demarée, G., Llasat, M. C., Macdonald, N. et al. (2020). 'Current European flood-rich period exceptional compared with past 500 years'. In: *Nature* vol. 583, no. 7817, pp. 560–566. doi: https://doi.org/10.1038/s41586-020-2478-3.

Brázdil, R., Demarée, G. R., Deutsch, M., Garnier, E., Kiss, A., Luterbacher, J., Macdonald, N., Rohr, C., Dobrovolnỳ, P., Kolář, P. et al. (2010). 'European floods during the winter 1783/1784: scenarios of an extreme event during the 'Little Ice Age''. In: *Theoretical and Applied Climatology* vol. 100, pp. 163–189. doi: https://doi.org/10.1007/s00704-009-0170-5.

Burkhart, J. F., Matt, F. N., Helset, S., Sultan Abdella, Y., Skavhaug, O. and Silantyeva, O. (2021). 'Shyft v4. 8: a framework for uncertainty assessment and distributed hydrologic modeling for operational hydrology'. In: *Geoscientific Model Development* vol. 14, no. 2, pp. 821–842. doi: https://doi.org/10.5194/gmd-14-821-2021.

Cannon, A. J., Sobie, S. R. and Murdock, T. Q. (2015). 'Bias correction of GCM precipitation by quantile mapping: how well do methods preserve changes in quantiles and extremes?' In: *Journal of Climate* vol. 28, no. 17, pp. 6938–6959. doi: https://doi.org/10.1175/JCLI-D-14-00754.1.

Chahine, M. T. (1992). 'The hydrological cycle and its influence on climate'. In: *Nature* vol. 359, no. 6394, pp. 373–380. doi: https://doi.org/10.1038/359373a0.

Chai, T. and Draxler, R. R. (2014). 'Root mean square error (RMSE) or mean absolute error (MAE)'. In: *Geoscientific model development discussions* vol. 7, no. 1, pp. 1525–1534. doi: https://doi.org/10.5194/gmdd-7-1525-2014.

Connolly, R., Soon, W., Connolly, M., Baliunas, S., Berglund, J., Butler, C. J., Cionco, R. G., Elias, A. G., Fedorov, V. M., Harde, H. et al. (2021). 'How much has the Sun influenced Northern Hemisphere temperature trends? An ongoing debate'. In: *Research in Astronomy and Astrophysics* vol. 21, no. 6, p. 131. doi: https://doi.org/10.1088/1674-4527/21/6/131.

Desmet, P. (1997). 'Effects of interpolation errors on the analysis of DEMs'. In: *Earth surface processes and landforms: The Journal of the British Geomorphological Group* vol. 22, no. 6, pp. 563–580. doi: https://doi.org/10.1002/(SICI)1096-9837(199706)22:6<563::AID-ESP713>3.0.CO;2-3.

Dottori, F., Salamon, P., Bianchi, A., Alfieri, L., Hirpa, F. A. and Feyen, L. (2016). 'Development and evaluation of a framework for global flood hazard mapping'. In: *Advances in water resources* vol. 94, pp. 87–102. doi: https://doi.org/10.1016/j.advwatres.2016.05.002.

Douben, K.-J. (2006). 'Characteristics of river floods and flooding: a global overview, 1985–2003'. In: *Irrigation and Drainage: The journal of the International Commission on Irrigation and Drainage* vol. 55, no. S1, S9–S21. doi: https://doi.org/10.1002/ird.239.

Drageset, T.-A. (2000). 'Flomberegning for Otta og Gudbrandsdalslågen'. In: *Norges vassdragsog energidirektorat, Oslo*.

Egorova, T., Schmutz, W., Rozanov, E., Shapiro, A. I., Usoskin, I., Beer, J., Tagirov, R. V. and Peter, T. (2018). 'Revised historical solar irradiance forcing'. In: *Astronomy & Astrophysics* vol. 615, A85. doi: https://doi.org/10.1051/0004-6361/201731199.

Engeland, K., Wilson, D., Borsányi, P., Roald, L. and Holmqvist, E. (2018). 'Use of historical data in flood frequency analysis: a case study for four catchments in Norway'. In: *Hydrology Research* vol. 49, no. 2, pp. 466–486. doi: https://doi.org/10.2166/nh.2017.069.

Engeland, K., Aano, A., Steffensen, I., Støren, E. and Paasche, Ø. (2020). 'New flood frequency estimates for the largest river in Norway based on the combination of short and long time series'. In: *Hydrology and Earth System Sciences* vol. 24, no. 11, pp. 5595–5619. doi: https://doi.org/10.5194/hess-24-5595-2020.

Erlandsen, H. B., Tallaksen, L. M. and Kristiansen, J. (2019). 'Merits of novel high-resolution estimates and existing long-term estimates of humidity and incident radiation in a complex domain'. In: *Earth System Science Data* vol. 11, no. 2, pp. 797–821. doi: https://doi.org/10.5194/essd-11-797-2019.

Fang, G., Yang, J., Chen, Y. and Zammit, C. (2015). 'Comparing bias correction methods in downscaling meteorological variables for a hydrologic impact study in an arid area in China'. In: *Hydrology and Earth System Sciences* vol. 19, no. 6, pp. 2547–2559. doi: https://doi.org/10.5194/hess-19-2547-2015.

Finans Norge (2023). *Natur- og værskader*. Available at https://www.finansnorge.no/tema/statistikk-og-analyse/forsikring/natur--og-varskader/. Viewed: 26. April 2023.

Glover, B., Sælthun, N. and Lilleeng Walløe, K. (2018). 'Verdien av vassdragsreguleringer for reduksjon av flomskader'. In: *Multiconsult: Oslo, Norway*, p. 50.

Gottschalk, L., Jensen, J. L., Lundquist, D., Solantie, R. and Tollan, A. (1979). 'Hydrologic regions in the Nordic countries'. In: *Hydrology Research* vol. 10, no. 5, pp. 273–286. doi: https://doi.org/10.2166/nh.1979.0010.

Grove, J. M. (1972). 'The incidence of landslides, avalanches, and floods in western Norway during the Little Ice Age'. In: *Arctic and Alpine Research* vol. 4, no. 2, pp. 131–138.

Guo, C., Bentsen, M., Bethke, I., Ilicak, M., Tjiputra, J., Toniazzo, T., Schwinger, J. and Otterå, O. H. (2019). 'Description and evaluation of NorESM1-F: A fast version of the Norwegian Earth System Model (NorESM)'. In: *Geoscientific Model Development* vol. 12, no. 1, pp. 343–362. doi: https://doi.org/10.5194/gmd-12-343-2019.

Gupta, H. V., Kling, H., Yilmaz, K. K. and Martinez, G. F. (2009). 'Decomposition of the mean squared error and NSE performance criteria: Implications for improving hydrological modelling'. In: *Journal of hydrology* vol. 377, no. 1-2, pp. 80–91. doi: https://doi.org/10.1016/j.jhydrol.2009.08.003.

Haddeland, I. (2022). *HySN2018v2005ERA5 (Version 1) [Data set]*. Zenodo. (Accessed on: 19-09-2022). doi: https://doi.org/10.5281/zenodo.5947547.

Hanssen-Bauer, I., Drange, H., Førland, E., Roald, L. A., Børsheim, K., Hisdal, H., Lawrence, D., Nesje, A., Sandven, S., Sorteberg, A. et al. (2009). 'Klima

i Norge 2100'. In: *Bakgrunnsmateriale til NOU Klimatilpassing., Norsk klimasenter, Oslo, Norway*.

Hanssen-Bauer, I., Førland, E., Haddeland, I., Hisdal, H., Lawrence, D., Mayer, S., Nesje, A., Nilsen, J., Sandven, S., Sandø, A. et al. (2017). 'Climate in Norway 2100–a knowledge base for climate adaptation'. In: *NCCS report* vol. 1, p. 2017.

Hegdahl, T. J., Engeland, K., Müller, M. and Sillmann, J. (2020). 'An event-based approach to explore selected present and future atmospheric river–induced floods in western Norway'. In: *Journal of Hydrometeorology* vol. 21, no. 9, pp. 2003–2021. doi: https://doi.org/10.1175/JHM-D-19-0071.1.

Heo, J.-H., Ahn, H., Shin, J.-Y., Kjeldsen, T. R. and Jeong, C. (2019). 'Probability distributions for a quantile mapping technique for a bias correction of precipitation data: A case study to precipitation data under climate change'. In: *Water* vol. 11, no. 7, p. 1475. doi: https://doi.org/10.3390/w11071475.

Hersbach, H. et al. (2018). *ERA5 hourly data on single levels from 1959 to present*. Copernicus Climate Change Service (C3S) Climate Data Store (CDS). (Accessed on: 14-10-2022). doi: https://doi.org/10.24381/cds.adbb2d47.

Hock, R. (2003). 'Temperature index melt modelling in mountain areas'. In: *Journal of hydrology* vol. 282, no. 1-4, pp. 104–115. doi: https://doi.org/10.1016/S0022-1694(03)00257-9.

Hofstätter, M., Chimani, B., Lexer, A. and Blöschl, G. (2016). 'A new classification scheme of European cyclone tracks with relevance to precipitation'. In: *Water Resources Research* vol. 52, no. 9, pp. 7086–7104. doi: https://doi.org/10.1002/2016WR019146.

Huang, S., Eisner, S., Haddeland, I. and Mengistu, Z. T. (2022). 'Evaluation of two new-generation global soil databases for macro-scale hydrological modelling in Norway'. In: *Journal of Hydrology* vol. 610, p. 127895. doi: https://doi.org/10.1016/j.jhydrol.2022.127895.

Huo, R., Li, L., Engeland, K., Xu, C.-Y., Chen, H., Paasche, Ø. and Guo, S. (2022). 'Changing flood dynamics in Norway since the last millennium and to the end of the 21st century'. In: *Journal of Hydrology*, p. 128331. doi: https://doi.org/10.1016/j.jhydrol.2022.128331.

Jenkinson, A. F. (1955). 'The frequency distribution of the annual maximum (or minimum) values of meteorological elements'. In: *Quarterly Journal of the Royal Meteorological Society* vol. 81, no. 348, pp. 158–171. doi: https://doi.org/10.1002/qj.49708134804.

Jonkman, S. N. (2005). 'Global perspectives on loss of human life caused by floods'. In: *Natural hazards* vol. 34, no. 2, pp. 151–175. doi: https://doi.org/10.1007/s11069-004-8891-3.

Khan, S., Gabriel, H. and Rana, T. (2008). 'Standard precipitation index to track drought and assess impact of rainfall on watertables in irrigation areas'. In: *Irrigation and Drainage Systems* vol. 22, pp. 159–177. doi: https://doi.org/10.1007/s10795-008-9049-3.

King, D. E. (2009). 'Dlib-ml: A Machine Learning Toolkit'. In: *Journal of Machine Learning Research* vol. 10, pp. 1755–1758.

Kirchner, J. W. (2009). 'Catchments as simple dynamical systems: Catchment characterization, rainfall-runoff modeling, and doing hydrology backward'.

In: *Water Resources Research* vol. 45, no. 2. doi: https://doi.org/10.1029/2008WR006912.

Knoche, M., Fischer, C., Pohl, E., Krause, P. and Merz, R. (2014). 'Combined uncertainty of hydrological model complexity and satellite-based forcing data evaluated in two data-scarce semi-arid catchments in Ethiopia'. In: *Journal of hydrology* vol. 519, pp. 2049–2066. doi: https://doi.org/10.1016/j.jhydrol.2014.10.003.

Kolberg, S., Rue, H. and Gottschalk, L. (2006). 'A Bayesian spatial assimilation scheme for snow coverage observations in a gridded snow model'. In: *Hydrology and Earth System Sciences* vol. 10, no. 3, pp. 369–381. doi: https://doi.org/10.5194/hess-10-369-2006.

Lafon, T., Dadson, S., Buys, G. and Prudhomme, C. (2013). 'Bias correction of daily precipitation simulated by a regional climate model: a comparison of methods'. In: *International journal of climatology* vol. 33, no. 6, pp. 1367–1381. doi: https://doi.org/10.1002/joc.3518.

Larsen-Vonstett, Ø. (2020). 'Ekstremværrapporten fra If: Slik er Norge forberedt på mer ekstremvær'. In: *CICERO Report*. doi: .

Lawrence, D. (2020). 'Uncertainty introduced by flood frequency analysis in projections for changes in flood magnitudes under a future climate in Norway'. In: *Journal of Hydrology: Regional Studies* vol. 28, p. 100675. doi: https://doi.org/10.1016/j.ejrh.2020.100675.

Lawrence, D. and Hisdal, H. (2011). 'Hydrological projections for floods in Norway under a future climate'. In.

Lindau, R. and Simmer, C. (2013). 'On correcting precipitation as simulated by the regional climate model COSMO-CLM with daily rain gauge observations'. In: *Meteorology and Atmospheric Physics* vol. 119, pp. 31–42. doi: https://doi.org/10.1007/s00703-012-0215-7.

Lindström, G., Johansson, B., Persson, M., Gardelin, M. and Bergström, S. (1997). 'Development and test of the distributed HBV-96 hydrological model'. In: *Journal of hydrology* vol. 201, no. 1-4, pp. 272–288. doi: https://doi.org/10.1016/S0022-1694(97)00041-3.

Lins, H. F. and Slack, J. R. (1999). 'Streamflow trends in the United States'. In: *Geophysical research letters* vol. 26, no. 2, pp. 227–230. doi: https://doi.org/10.1029/1998GL900291.

Loster, T. (1999). 'Flood trends and global change'. In: *Proceedings IIASA Conf on Global Change and Catastrophe Management: Flood Risks in Europe*.

Mardal, M. A. (2018). *Storofsen*. Available at https://snl.no/Storofsen. Viewed: 31. August 2022.

Markonis, Y., Kossieris, P., Lykou, A. and Koutsoyiannis, D. (2012). 'Effects of Medieval Warm Period and Little Ice Age on the hydrology of Mediterranean region'. In: *EGU General Assembly Conference Abstracts*, p. 12181.

McKee, T. B., Doesken, N. J. and Kleist, J. (1995). 'Drought Monitoring with Multiple Time Scales, 9th Conference, Applied climatology'. In: *CONFERENCE ON APPLIED CLIMATOLOGY, Applied climatology, 9th Conference, Applied climatology*. The Society, pp. 233–236.

McKee, T. B., Doesken, N. J., Kleist, J. et al. (1993). 'The relationship of drought frequency and duration to time scales'. In: *Proceedings of the 8th Conference on Applied Climatology*. Vol. 17. 22. Boston, pp. 179–183.

Merz, R. and Blöschl, G. (2003). 'A process typology of regional floods'. In: *Water resources research* vol. 39, no. 12. doi: https://doi.org/10.1029/2002WR001952.

Muñoz Sabater, J. (2019). *ERA5-Land hourly data from 1981 to present [Data set]*. Copernicus Climate Change Service (C3S) Climate Data Store (CDS). (Accessed on: 19-09-2022). doi: https://doi.org/10.24381/cds.e2161bac.

— (2021). *ERA5-Land hourly data from 1950 to 1980 [Data set]*. Copernicus Climate Change Service (C3S) Climate Data Store (CDS). (Accessed on: 19-09-2022). doi: https://doi.org/10.24381/cds.e2161bac.

Nadim, F., Pedersen, S. A. S., Schmidt-Thomé, P., Sigmundsson, F. and Engdahl, M. (2008). 'Natural hazards in Nordic countries'. In: *Episodes Journal of International Geoscience* vol. 31, no. 1, pp. 176–184. doi: https://doi.org/10.18814/epiiugs/2008/v31i1/024.

Nash, J. E. and Sutcliffe, J. V. (1970). 'River flow forecasting through conceptual models part I—A discussion of principles'. In: *Journal of hydrology* vol. 10, no. 3, pp. 282–290. doi: https://doi.org/10.1016/0022-1694(70)90255-6.

NERSC (2022). *PARCIM: Proxy Assimilation for Reconstructing Climate and Improving Model*. Available at https://www.nersc.no/nb/project/parcim. Viewed: 3. May 2023.

NVE (n.d.[a]). *Elverum*. Sildre, NVE. (Accessed on: 28-9-2022). url: https://sildre.nve.no/station/2.604.0.

— (n.d.[b]). *Lalm*. Sildre, NVE. (Accessed on: 28-9-2022). url: https://sildre.nve.no/station/2.25.0.

Olsen, J. R., Stedinger, J. R., Matalas, N. C. and Stakhiv, E. Z. (1999). 'Climate variability and flood frequency estimation for the upper Mississippi and Lower Missouri rivers'. In: *JAWRA Journal of the American Water Resources Association* vol. 35, no. 6, pp. 1509–1523. doi: https://doi.org/10.1111/j.1752-1688.1999.tb04234.x.

Otnes, J. (1982). *Gamle flommerker langs Glåma*. Laget.

Pettersson, L. (2000). 'Flomberegning for Glommavassdraget Oppstrøms Vorma'. In: *Norges vassdragsog energidirektorat, Oslo*.

— (2014). 'Aktive vannføringsstasjoner i Norge'. In: *Norges vassdragsog energidirektorat, Oslo*.

Pierce, D. W., Cayan, D. R., Maurer, E. P., Abatzoglou, J. T. and Hegewisch, K. C. (2015). 'Improved bias correction techniques for hydrological simulations of climate change'. In: *Journal of Hydrometeorology* vol. 16, no. 6, pp. 2421–2442. doi: https://doi.org/10.1175/JHM-D-14-0236.1.

Pilgrim, D. H., Cordery, I. and Baron, B. C. (1982). 'Effects of catchment size on runoff relationships'. In: *Journal of Hydrology* vol. 58, no. 3-4, pp. 205–221. doi: https://doi.org/10.1016/0022-1694(82)90035-X.

Powell, M. J. (2009). 'The BOBYQA algorithm for bound constrained optimization without derivatives'. In: *Cambridge NA Report NA2009/06, University of Cambridge, Cambridge* vol. 26.

Priestley, C. H. B. and Taylor, R. J. (1972). 'On the assessment of surface heat flux and evaporation using large-scale parameters'. In: *Monthly weather review* vol. 100, no. 2, pp. 81–92. doi: https://doi.org/10.1175/1520-0493(1972)100<0081:OTAOSH>2.3.CO;2.

Ritter, A. and Munoz-Carpena, R. (2013). 'Performance evaluation of hydrological models: Statistical significance for reducing subjectivity in

goodness-of-fit assessments'. In: *Journal of Hydrology* vol. 480, pp. 33–45. doi: https://doi.org/10.1016/j.jhydrol.2012.12.004.

Roald, L. A. (2013). *Flom i Norge*. Tom & Tom.

Salas, J. D. and Obeysekera, J. (2014). 'Revisiting the concepts of return period and risk for nonstationary hydrologic extreme events'. In: *Journal of Hydrologic Engineering* vol. 19, no. 3, pp. 554–568. doi: https://doi.org/10.1061/(ASCE)HE.1943-5584.0000820.

Schaefli, B. and Gupta, H. V. (2007). 'Do Nash values have value?' In: *Hydrological Processes* vol. 21, no. ARTICLE, pp. 2075–2080. doi: https://doi.org/10.1002/hyp.6825.

Shepard, D. (1968). 'A two-dimensional interpolation function for irregularly-spaced data'. In: *Proceedings of the 1968 23rd ACM national conference*, pp. 517–524. doi: https://doi.org/10.1145/800186.810616.

Sigl, M., Winstrup, M., McConnell, J. R., Welten, K. C., Plunkett, G., Ludlow, F., Büntgen, U., Caffee, M., Chellman, N., Dahl-Jensen, D. et al. (2015). 'Timing and climate forcing of volcanic eruptions for the past 2,500 years'. In: *Nature* vol. 523, no. 7562, pp. 543–549. doi: https://doi.org/10.1038/nature14565.

Skaugen, T. and Randen, F. (2013). 'Modeling the spatial distribution of snow water equivalent, taking into account changes in snow-covered area'. In: *Annals of glaciology* vol. 54, no. 62, pp. 305–313. doi: https://doi.org/10.3189/2013AoG62A162.

Skaugen, T. and Weltzien, I. H. (2016). 'A model for the spatial distribution of snow water equivalent parameterized from the spatial variability of precipitation'. In: *The Cryosphere* vol. 10, no. 5, pp. 1947–1963. doi: https://doi.org/10.5194/tc-10-1947-2016.

Sommerfeldt, W. (1972). *Ofsen i 1789: og virkninger av den i Fron*. Fron historielag.

Sorteberg, A., Lawrence, D., Dyrrdal, A., Mayer, S. and Engeland, K. (2018). 'Climatic changes in short duration extreme precipitation and rapid onset flooding–implications for design values'. In: *Report* vol. 1, p. 2018.

Steinhilber, F., Beer, J. and Fröhlich, C. (2009). 'Total solar irradiance during the Holocene'. In: *Geophysical Research Letters* vol. 36, no. 19. doi: https://doi.org/10.1029/2009GL040142.

Taye, G., Poesen, J., Wesemael, B. V., Vanmaercke, M., Teka, D., Deckers, J., Goosse, T., Maetens, W., Nyssen, J., Hallet, V. et al. (2013). 'Effects of land use, slope gradient, and soil and water conservation structures on runoff and soil loss in semi-arid Northern Ethiopia'. In: *Physical Geography* vol. 34, no. 3, pp. 236–259. doi: https://doi.org/10.1080/02723646.2013.832098.

Team, U., Bontemps, S., Defourny, P., Van Bogaert, E., Team, E., Arino, O., Kalogirou, V. and Perez, J. R. (2011). 'GLOBCOVER 2009 Products Description and Validation Report'. In.

Teutschbein, C. and Seibert, J. (2012). 'Bias correction of regional climate model simulations for hydrological climate-change impact studies: Review and evaluation of different methods'. In: *Journal of hydrology* vol. 456, pp. 12–29. doi: https://doi.org/10.1016/j.jhydrol.2012.05.052.

The Norwegian Meteorological institute, MET Norway (2022). *Norwegian observational gridded climate datasets [Data set]*. Thredds.met. (Accessed on: 05-09-2022). url: https://thredds.met.no/thredds/catalog/senorge/seNorge_2018/Archive/catalog.html.

Thom, H. C. (1958). 'A note on the gamma distribution'. In: *Monthly weather review* vol. 86, no. 4, pp. 117–122. doi: https://doi.org/10.1175/1520-0493(1958)086<0117:ANOTGD>2.0.CO;2.

Thorsnæs, G. (2021). *Gauldalen*. Available at https://snl.no/Gauldalen. Viewed: 31. August 2022.

Tong, Y., Gao, X., Han, Z., Xu, Y., Xu, Y. and Giorgi, F. (2021). 'Bias correction of temperature and precipitation over China for RCM simulations using the QM and QDM methods'. In: *Climate Dynamics* vol. 57, no. 5, pp. 1425–1443. doi: https://doi.org/10.1007/s00382-020-05447-4.

Van Montfort, M. and Witter, J. (1986). 'The generalized Pareto distribution applied to rainfall depths'. In: *Hydrological Sciences Journal* vol. 31, no. 2, pp. 151–162. doi: https://doi.org/10.1080/02626668609491037.

Viglione, A., Hosking, J. R., Laio, F., Miller, A., Gaume, E., Payrastre, O., Salinas, J. L., N'guyen, C. C., Halbert, K. and Viglione, M. A. (2020). 'Package 'nsRFA''. In: *Non-supervised Regional Frequency Analysis. CRAN Repository*, pp. 1–7.

Vormoor, K., Lawrence, D., Schlichting, L., Wilson, D. and Wong, W. K. (2016). 'Evidence for changes in the magnitude and frequency of observed rainfall vs. snowmelt driven floods in Norway'. In: *Journal of Hydrology* vol. 538, pp. 33–48. doi: https://doi.org/10.1016/j.jhydrol.2016.03.066.

Walter, I. A., Allen, R. G., Elliott, R., Jensen, M., Itenfisu, D., Mecham, B., Howell, T., Snyder, R., Brown, P., Echings, S. et al. (2005). *ASCE Standardized Reference Evapotranspiration Equation*. American Society of Civil Engineers.

Winsemius, H. C., Aerts, J. C., Van Beek, L. P., Bierkens, M. F., Bouwman, A., Jongman, B., Kwadijk, J. C., Ligtvoet, W., Lucas, P. L., Van Vuuren, D. P. et al. (2016). 'Global drivers of future river flood risk'. In: *Nature Climate Change* vol. 6, no. 4, pp. 381–385. doi: https://doi.org/10.1038/nclimate2893.

Yang, W., Gardelin, M., Olsson, J. and Bosshard, T. (2015). 'Multi-variable bias correction: application of forest fire risk in present and future climate in Sweden'. In: *Natural Hazards and Earth System Sciences* vol. 15, no. 9, pp. 2037–2057. doi: https://doi.org/10.5194/nhess-15-2037-2015.

Yao, A. Y. (1974). 'A statistical model for the surface relative humidity'. In: *Journal of Applied Meteorology and Climatology* vol. 13, no. 1, pp. 17–21. doi: https://doi.org/10.1175/1520-0450(1974)013<0017:ASMFTS>2.0.CO;2.

Yilmaz, M. U. and Onoz, B. (2020). 'A comparative study of statistical methods for daily streamflow estimation at ungauged basins in Turkey'. In: *Water* vol. 12, no. 2, p. 459. doi: https://doi.org/10.3390/w12020459.

Østmoe, A. (1985). *Stor-ofsen 1789: værsystemet som førte til den største flomkatastrofen i Norge*. Oversiktsregisteret.

Appendices

APPENDIX A

Figures and Tables

A.1 Figures

Figure A.1 - Figure A.2 show the seasonal mean and standard deviation of the observed, paleo simulated and bias corrected paleo simulated model forcings. Time series of temperature and precipitation before and after bias correction is shown in Figure A.3 and Figure A.4, respectively. Figure A.5 - Figure A.9 show the decadal timeseries of discharge, temperature, precipitation, SWE and SCA, respectively. Plots of flood quantiles and the corresponding GEV distribution fit are shown in Figure A.10 and Figure A.11. Similar plots for precipitation quantiles are included in Figure A.12 and Figure A.13.

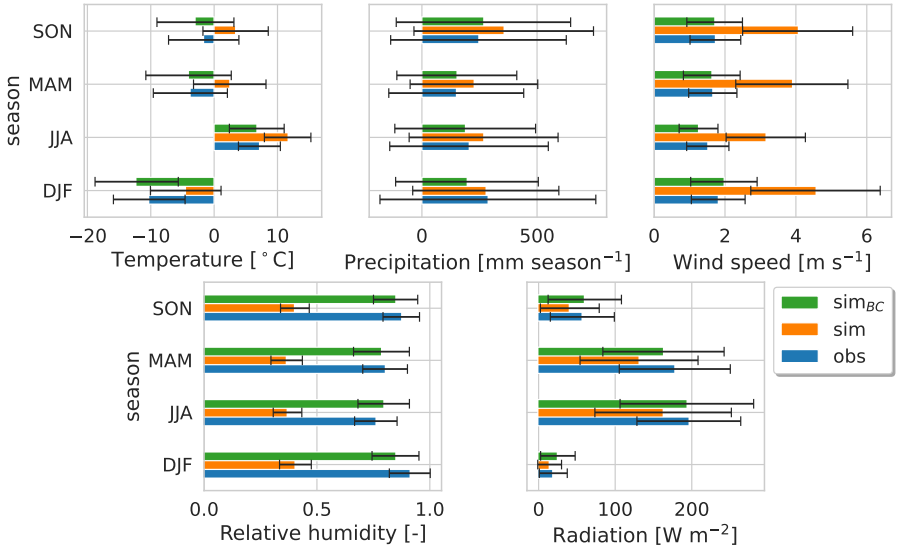

Figure A.1: Seasonal mean and standard deviation for Lalm with Solar 2. Bars represent means and error bars represent standard deviations. The notation *BC* denotes bias corrected. Observations are from 1960-2020 and paleo simulations from 851-1959.

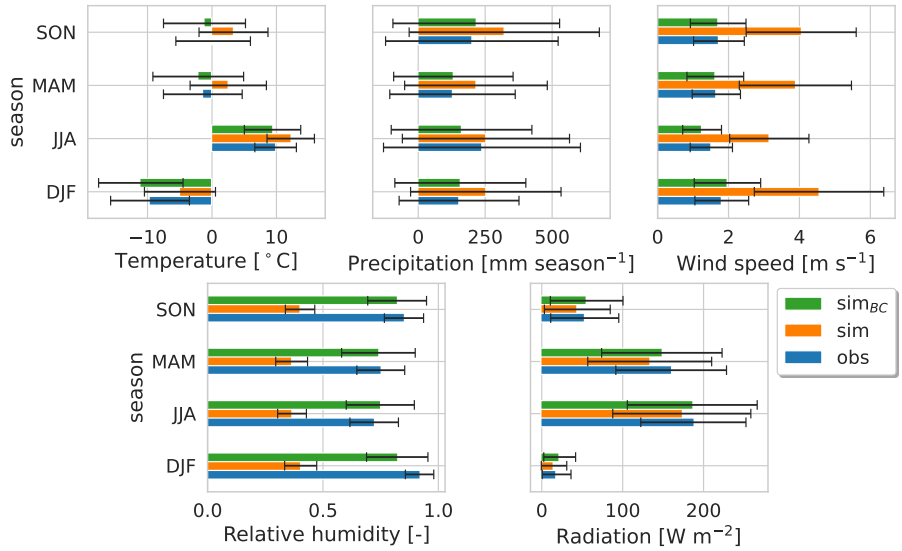

Figure A.2: Seasonal mean and standard deviation for Elverum with Solar 2. Bars represent means and error bars represent standard deviations. The notation *BC* denotes bias corrected. Observations are from 1960-2020 and paleo simulations from 851-1959.

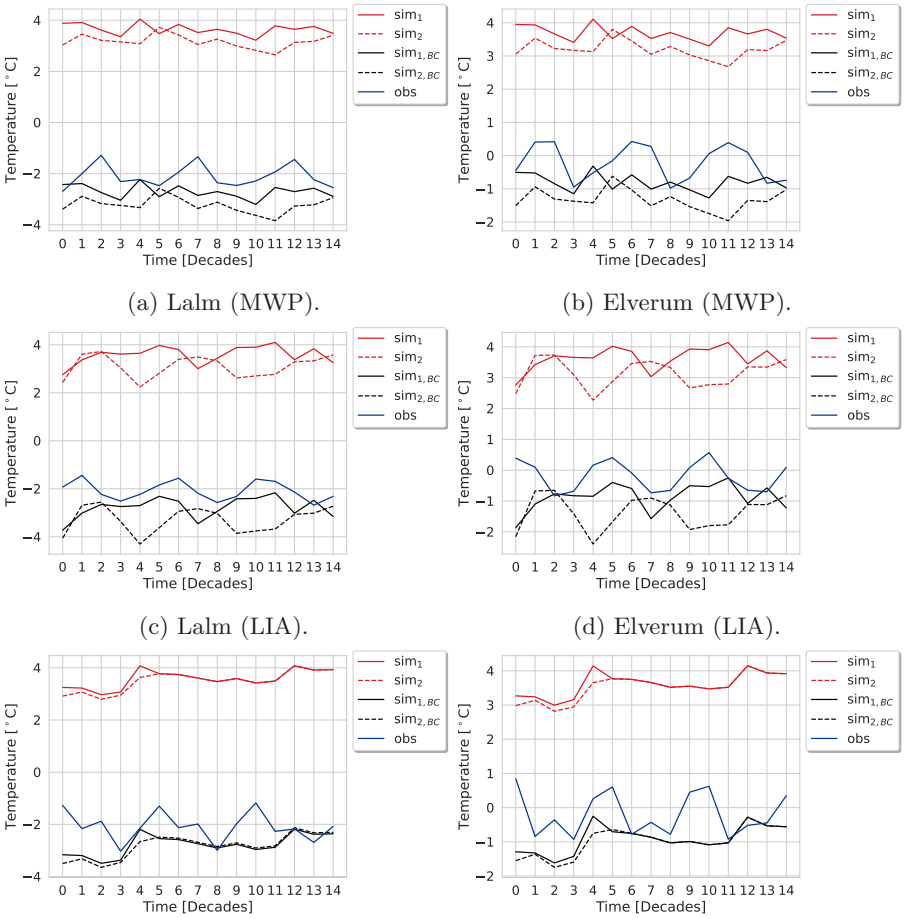

(a) Lalm (MWP).

(b) Elverum (MWP).

(c) Lalm (LIA).

(d) Elverum (LIA).

(e) Lalm (IT).

(f) Elverum (IT).

Figure A.3: Time series of temperature before and after bias correction, for (a)-(b) MWP, (c)-(d) LIA and (e)-(f) IT at Lalm and Elverum. Subscripts 1 and 2 denote Solar 1 and 2, respectively. BC denotes bias corrected.

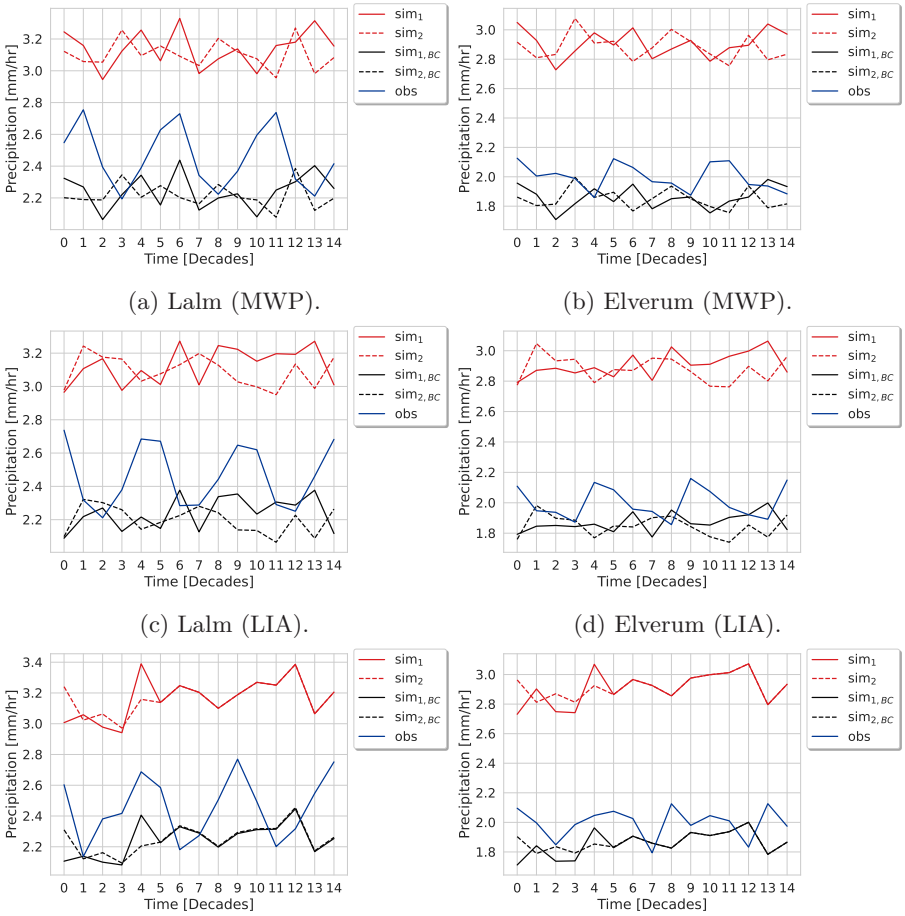

(a) Lalm (MWP). (b) Elverum (MWP).

(c) Lalm (LIA). (d) Elverum (LIA).

(e) Lalm (IT). (f) Elverum (IT).

Figure A.4: Time series of precipitation before and after bias correction, for (a)-(b) MWP, (c)-(d) LIA and (e)-(f) IT at Lalm and Elverum. Subscripts 1 and 2 denote Solar 1 and 2, respectively. BC denotes bias corrected.

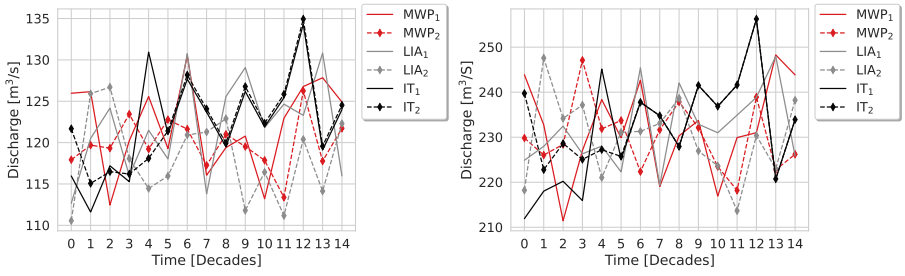

(a) Lalm. (b) Elverum.

Figure A.5: Decadal discharge timeseries at (a) Lalm and (b) Elverum.

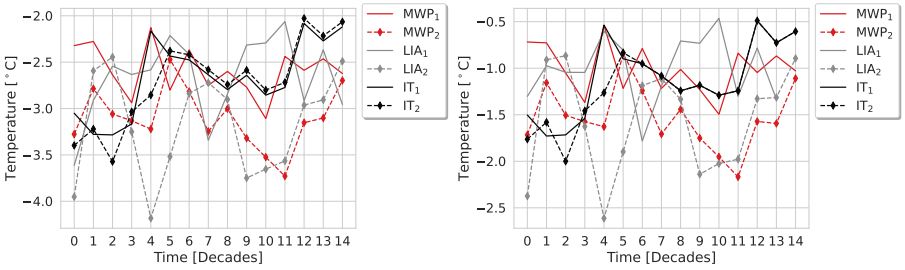

(a) Lalm. (b) Elverum.

Figure A.6: Decadal temperature timeseries at (a) Lalm and (b) Elverum.

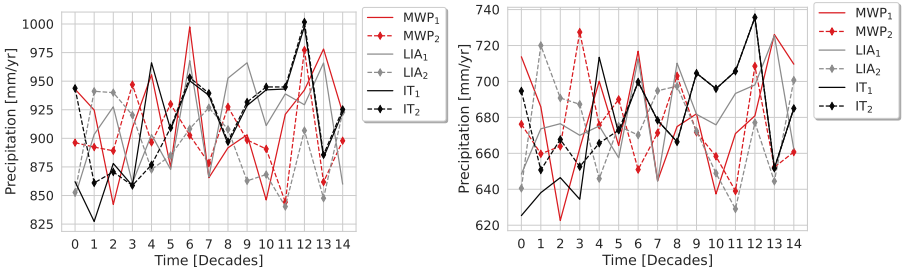

(a) Lalm. (b) Elverum.

Figure A.7: Decadal precipitation timeseries at (a) Lalm and (b) Elverum.

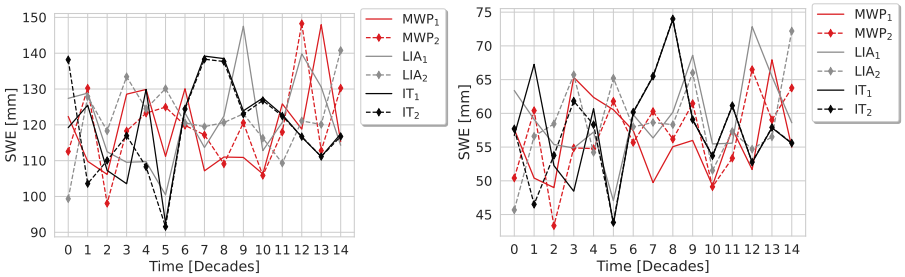

(a) Lalm. (b) Elverum.

Figure A.8: Decadal SWE timeseries at (a) Lalm and (b) Elverum.

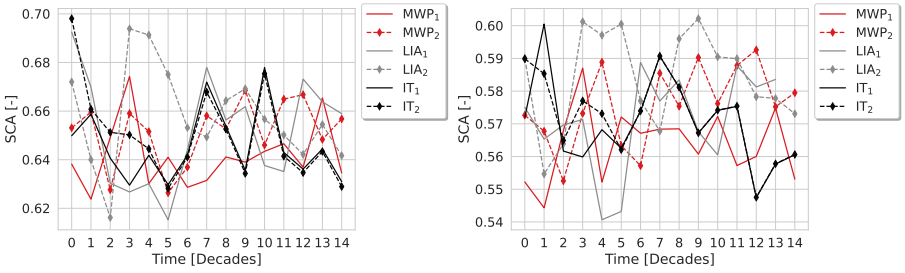

(a) Lalm. (b) Elverum.

Figure A.9: Decadal SCA timeseries at (a) Lalm and (b) Elverum.

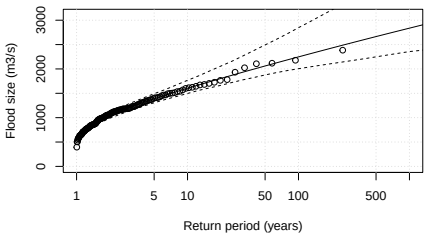

(a) MWP (Solar 1)

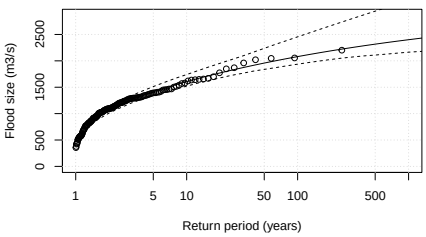

(b) MWP (Solar 2)

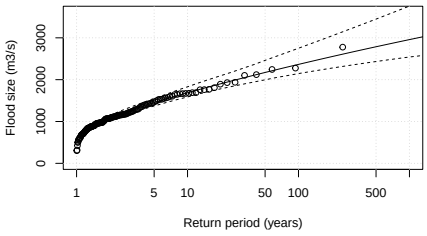

(c) LIA (Solar 1)

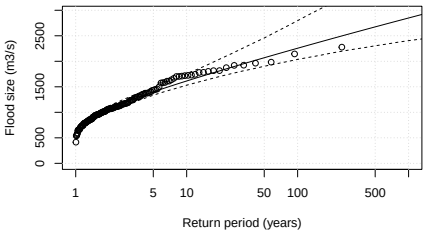

(d) LIA (Solar 2)

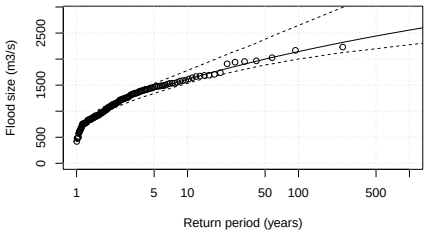

(e) IT (Solar 1)

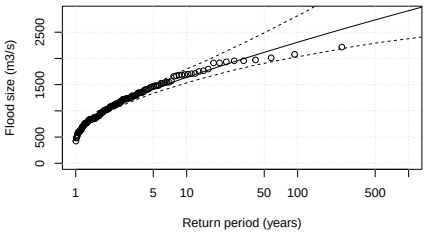

(f) IT (Solar 2)

Figure A.10: Flood quantile plots for (a)-(b) MWP, (c)-(d) LIA and (e)-(f) IT at Lalm.

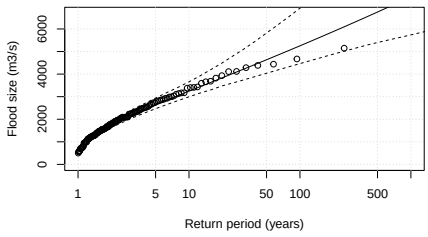

(a) MWP (Solar 1)

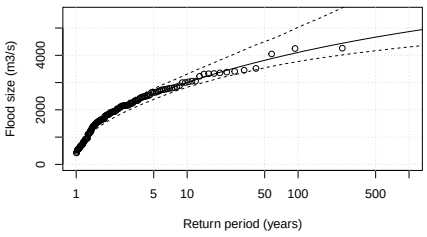

(b) MWP (Solar 2)

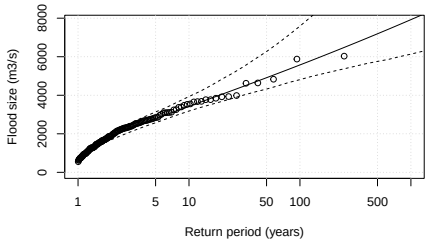

(c) LIA (Solar 1)

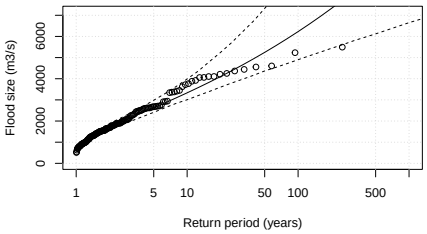

(d) LIA (Solar 2)

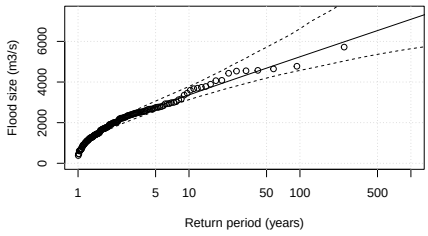

(e) IT (Solar 1)

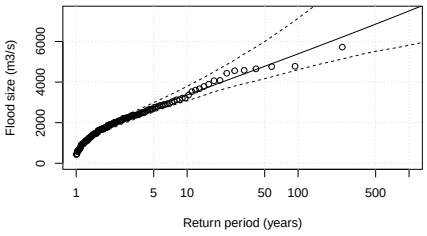

(f) IT (Solar 2)

Figure A.11: Flood quantile plots for (a)-(b) MWP, (c)-(d) LIA and (e)-(f) IT at Elverum.

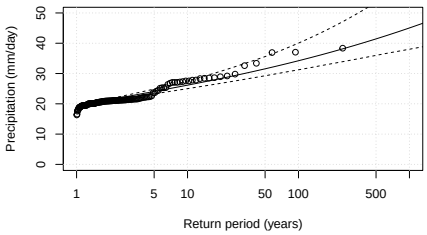

(a) MWP (Solar 1)

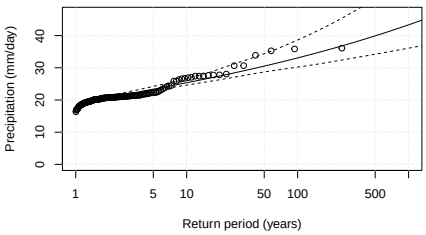

(b) MWP (Solar 2)

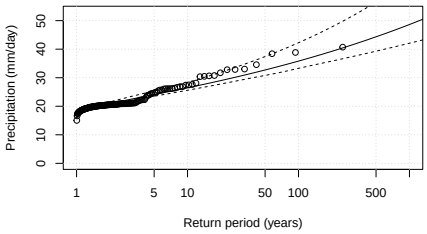

(c) LIA (Solar 1)

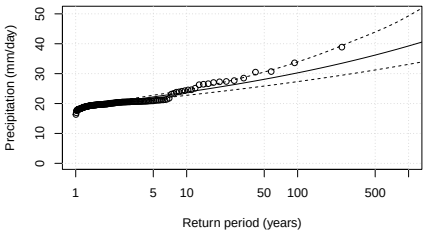

(d) LIA (Solar 2)

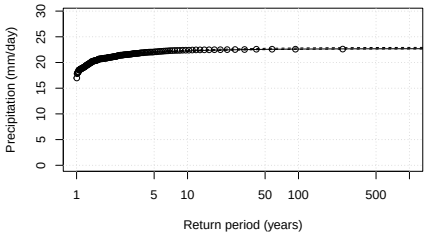

(e) IT (Solar 1)

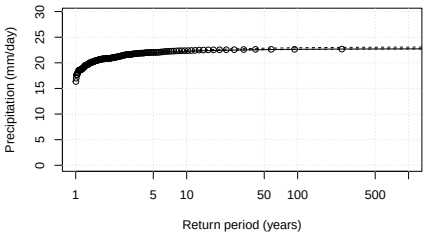

(f) IT (Solar 2)

Figure A.12: Precipitation quantile plots for (a)-(b) MWP, (c)-(d) LIA and (e)-(f) IT at Lalm.

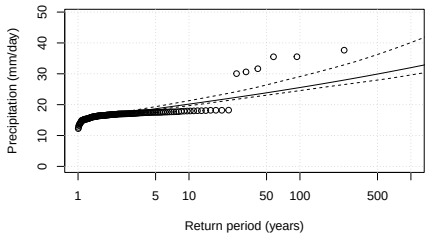

(a) MWP (Solar 1)

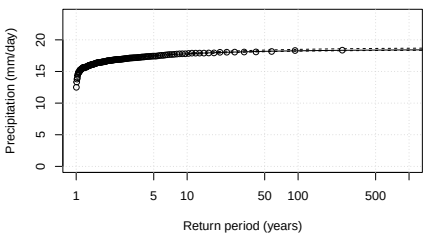

(b) MWP (Solar 2)

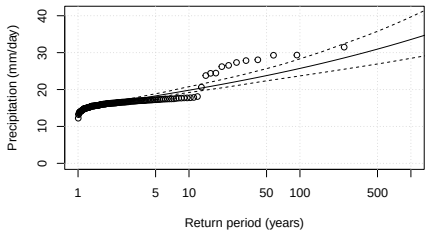

(c) LIA (Solar 1)

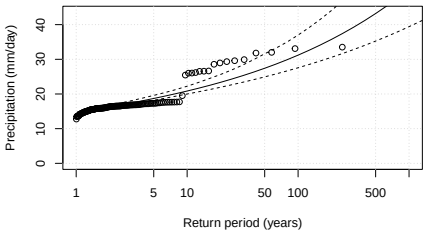

(d) LIA (Solar 2)

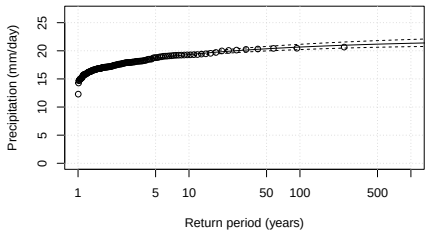

(e) IT (Solar 1)

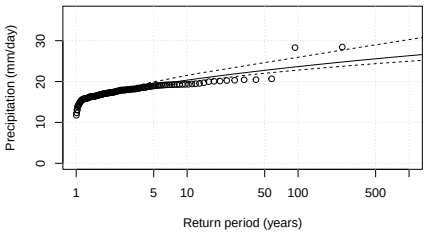

(f) IT (Solar 2)

Figure A.13: Precipitation quantile plots for (a)-(b) MWP, (c)-(d) LIA and (e)-(f) IT at Elverum.

A.2 Tables

The 95% confidence intervals for the simulated 100-year floods are included in Table A.1. Table A.2 - Table A.7 show the seasonal mean discharge, temperature and precipitation for Lalm and Elverum. Table A.8 shows the GlobCover characteristics (Team et al., 2011) that was used to create the Shyft model cell, that represented the model region.

Table A.1: 100-year flood 95% confidence intervals [m^3/s].Lalm and Elverum are denoted L and E. S1 and S2 refers to Solar 1 and 2, respectively.

	S	**MWP**	**LIA**	**IT**	**Obs**
L	1	[1954, 2355]	[2139, 2809]	[1988, 2482]	[939, 1745]
	2	[2024, 2639]	[2052, 2777]	[2033, 2788]	[939, 1745]
E	1	[4495, 6966]	[4728, 7990]	[4604, 6806]	[2365, 5184]
	2	[3781, 5010]	[5045, 8655]	[4567, 6828]	[2365, 5184]

Table A.2: Seasonal mean discharge at Lalm [m^3/s].

	MWP		LIA		IT		
Season	**SV 1**	**SV2**	**SV 1**	**SV 2**	**SV 1**	**SV 2**	**Obs**
DJF	22.4	23.7	23.9	23.1	24.3	26.0	21.5
MAM	111.6	107.9	108.8	98.4	105.4	102.3	58.8
JJA	226	227.7	231.8	230.6	233.6	234.6	260.0
SON	126.0	118.2	120.5	117.4	122.9	124.1	80.2

Table A.3: Seasonal mean discharge at Elverum [m^3/s].

	MWP		LIA		IT		
Season	**SV 1**	**SV2**	**SV 1**	**SV 2**	**SV 1**	**SV 2**	**Obs**
DJF	109.3	116.2	111.3	114.2	114.4	116.0	94.4
MAM	311.4	300.7	311.0	288.3	298.1	297.2	273.9
JJA	243.5	246.7	250.6	255.2	252.5	257.1	361.3
SON	260.2	255.1	252.3	257.5	256.3	260.6	240.5

Table A.4: Seasonal mean temperature at Lalm [°C].

	MWP		LIA		IT		
Season	**SV 1**	**SV2**	**SV 1**	**SV 2**	**SV 1**	**SV 2**	**Obs**
DJF	-11.4	-12.3	-11.6	-12.2	-11.7	-11.6	-8.9
MAM	-3.6	-4.0	-3.6	-4.2	-3.5	-3.6	-3.1
JJA	6.9	6.8	7.0	6.5	7.0	6.8	7.4
SON	-2.4	-3.0	-2.7	-3.1	-2.7	-2.7	-1.1

Table A.5: Seasonal mean temperature at Elverum [°C].

	MWP		LIA		IT		
Season	**SV 1**	**SV2**	**SV 1**	**SV 2**	**SV 1**	**SV 2**	**Obs**
DJF	-10.6	-11.5	-10.7	-11.4	-10.9	-10.9	-8.1
MAM	-2.0	-2.4	-2.0	-2.5	-1.9	-2.0	-0.3
JJA	9.3	9.2	9.4	9.0	9.4	9.2	10.6
SON	-1.0	-1.6	-1.2	-1.6	-1.3	-1.3	0.9

Table A.6: Seasonal mean precipitation at Lalm [mm/season].

	MWP		LIA		IT		
Season	**SV 1**	**SV2**	**SV 1**	**SV 2**	**SV 1**	**SV 2**	**Obs**
DJF	234.2	225.5	234.9	219.9	227.9	227.4	298.3
MAM	168.1	171.2	170.1	162.5	176.6	177.8	149.5
JJA	205.3	207.7	210.2	208.3	206.9	206.7	205.2
SON	308.1	299.1	297.6	301.5	302.4	305.6	226.2

Table A.7: Seasonal mean precipitation at Elverum [mm/season].

	MWP		LIA		IT		
Season	**SV 1**	**SV2**	**SV 1**	**SV 2**	**SV 1**	**SV 2**	**Obs**
DJF	163.5	158.5	165.9	156.1	159.5	159.5	150.7
MAM	133.0	132.5	132.8	129.1	133.9	136.3	132.7
JJA	163.6	166.1	166.4	165.5	163.4	163.6	257.3
SON	219.5	217.9	215.9	221.4	219.9	223.0	180.9

Table A.8: GlobCover properties.

Value	**GlobCover legend**	**LCCS Label**
11	Post-flooding or irrigated croplands (or aquatic)	Irrigated tree crops // Irrigated shrub crops // Irrigated herbaceous crops // Post-flooding cultivation of herbaceous crops
14	Rainfed croplands	Rainfed shrub crops // Rainfed tree crops // Rainfed herbaceous crops
20	Mosaic cropland (50-70%) / vegetation (20-50%)	Cultivated and managed terrestrial areas / Natural and semi-natural primarily terrestrial vegetation
30	Mosaic vegetation (50-70%) / cropland (20-50%)	Natural and semi-natural primarily terrestrial vegetation / Cultivated and managed

		terrestrial areas
40	Closed to open (>15%) broadleaved evergreen or semi-deciduous forest	Broadleaved evergreen closed to open trees // Semi-deciduous closed to open trees
50	Closed (>40%) broadleaved deciduous forest (>5m)	Broadleaved deciduous closed to open (100-40%) trees
60	Open (15-40%) broadleaved deciduous forest/ woodland (>5m)	Broadleaved deciduous (40-(20-10)%) woodland
70	Closed (>40%) needleleaved evergreen forest (>5m)	Needleleaved evergreen closed to open (100-40%) trees
90	Open (15-40%) needleleaved deciduous or evergreen forest (>5m)	Needleleaved evergreen (40-(20-10)%) woodland // Needleleaved deciduous (40-(20-10)%) woodland
100	Closed to open (>15%) mixed broadleaved and needleleaved forest (>5m)	Broadleaved closed to open trees / Needleleaved closed to open trees
110	Mosaic forest or shrubland (50-70%) / grassland (20-50%)	Closed to open trees / Closed to open shrubland (thicket) // Herbaceous closed to open vegetation
120	Mosaic grassland (50-70%) / forest or shrubland d (20-50%)	Closed to open shrubland (thicket) // Herbaceous closed to open vegetation / Closed to open trees
130	Closed to open (>15%) (broadleaved or needleleaved, evergreen or deciduous) shrubland (<5m)	Broadleaved closed to open shrubland (thicket)
140	Closed to open (>15%) herbaceous vegetation (grassland, savannas or lichens/mosses)	Herbaceous closed to very open vegetation // Closed to open lichens/mosses
150	Sparse (<15%) vegetation	Sparse trees // Herbaceous sparse vegetation // Sparse shrubs
160	Closed to open (>15%) broadleaved forest regularly flooded (semi-permanently or temporarily) - Fresh or brackish water	Closed to open (100-40%) broadleaved trees on temporarily flooded land, water quality: fresh water // Closed to open (100-40%) broadleaved trees on permanently flooded land, water quality: fresh water

170	Closed (>40%) broadleaved forest or shrubland permanently flooded - Saline or brackish water	Closed to open (100-40%) broadleaved trees on permanently flooded land (with daily variations), water quality: saline water // Closed to open (100-40%) broadleaved trees on permanently flooded land (with daily variations), water quality: brackish water // Closed to open (100-40%) semi-deciduous shrubland on permanently flooded land (with daily variations), water quality: saline water // Closed to open (100-40%) semi-deciduous shrubland on permanently flooded land (with daily variations), water quality: brackish water
180	Closed to open (>15%) grassland or woody vegetation on regularly flooded or waterlogged soil - Fresh, brackish or saline water	Closed to open shrubs // Closed to open herbaceous vegetation
190	Artificial surfaces and associated areas (Urban areas >50%)	Artificial surfaces and associated areas
200	Bare areas	Bare areas
210	Water bodies	Natural water bodies // Artificial Water bodies
220	Permanent snow and ice	Artificial perennial snow // Artificial perennial ice // Perennial snow // Perennial ice